Spring 1-1-2010

Measuring the Effect of Water Quality Parameters on the Release of Silver Nanoparticles from a Ceramic Surface Using a Quartz Crystal Microbalance

Michael Wayne Stewart
University of Colorado at Boulder, michael.w.stewart@colorado.e

Recommended Citation

Stewart, Michael Wayne, "Measuring the Effect of Water Quality Parameters on the Release of Silver Nanoparticles from a Ceramic Surface Using a Quartz Crystal Microbalance" (2010). *Civil Engineering Graduate Theses & Dissertations*. 30.
https://scholar.colorado.edu/cven_gradetds/30

Measuring the effect of water quality parameters on the release of silver nanoparticles from a ceramic surface using a quartz crystal microbalance

by

Michael Wayne Stewart
B.S., Colorado State University, 2003

A thesis submitted to the Faculty of the Graduate School of the
University of Colorado at Boulder in partial fulfillment
of the requirements for the degree of

Master of Science
Department of Civil, Environmental, and Architectural Engineering
2010

This thesis entitled:

Measuring the effect of water quality parameters on the release of silver nanoparticles from a ceramic surface using a quartz crystal microbalance

written by Michael W. Stewart

has been approved for the Department of
Civil, Environmental, and Architectural Engineering

____
Angela R. Bielefeldt

____
R. Scott Summers

____
Joseph N. Ryan

Date________________

The final copy of this thesis has been examined by the signatories, and we find that both the content and the form meet acceptable presentation standards of scholarly work in the above mentioned discipline.

Abstract

Stewart, Michael Wayne (M.S.; Environmental Engineering; Dept. of Civil, Environmental, and Architectural Engineering)

Measuring the effect of water quality parameters on the release of silver nanoparticles from a ceramic surface using a quartz crystal microbalance

Thesis directed by Angela R. Bielefeldt and R. Scott Summers

Ceramic water filters are used in many developing countries as a household water treatment technology, often produced locally using regionally-available materials, and constructed in various forms (i.e., as discs, candles, or pots) that all rely on similar mechanisms of filtration and inactivation. A common production technique involves application of an anti-microbial, colloidal silver coating to the porous ceramic filter. The silver coating has shown improvements in microbial log reduction values over uncoated ceramic filters both in the laboratory and in the field. However, a more complete understanding of the silver coating requires knowledge of specific characteristics of the colloidal silver solution, including particle size, composition, and charge, and to understand how these characteristics affect silver particle deposition, anti-microbial activity, and potential optimization of the silver coating. Additionally, as water passes through the ceramic filter, the silver coating will release from the ceramic surface, decreasing the effectiveness of the filter by reducing the presence of silver.

A colloidal silver solution was prepared according to procedures recommended for ceramic pot filter production. The solution was then characterized for particle size distribution, trace contaminants, and zeta potential. Silver nanoparticles were adsorbed onto a silica substrate and assessed with a quartz crystal microbalance to monitor silver release. Preliminary experiments showed a strong dependence of silver release on water quality, with adsorbed silver releasing from an unmodified quartz sensor into flowing 10% (v/v) influent solution of tryptic soy broth at approximately 50 times the rate of release of adsorbed silver caused by flowing Millipore ultrapure water alone. Experiments were conducted to determine the effects water quality, including pH, turbidity, ionic strength, and natural organic matter, on the release of silver nanoparticles from the silica substrate. The most significant release was caused by waters containing sodium hypochlorite, suggesting that cleaning of silver-containing ceramic filters should be performed with caution.

Dedication

To those fabricating, investigating, and promoting ceramic pot filters, but most importantly, to those using them.

Acknowledgments

This research was made possible by the Professional Research Experience Program (PREP) through the Materials Reliability Division at NIST-Boulder. I am particularly grateful to Stephanie Hooker, Elisabeth Mansfield, Nick Barbosa, and Whitney Patterson.

Previous ceramic pot filter research conducted at the University of Colorado at Boulder provided an excellent foundation for this investigation. Beyond that, Scott Summers and Angie Bielefeldt have my deepest appreciation for their insightful perspective, as well as their consistent and solid advice.

Finally, thanks to all those within the ceramic pot filter community - an inspiring group full of support, insight, and encouragement.

Table of Contents

List of Tables

List of Figures

Introduction

Leading global scientific institutions are in agreement over the need to conduct thorough research towards characterization and understanding of nanoparticles, most often defined as "any piece of produced material with at least one dimension between approximately 1 and 100 nanometers" (Auffan et al. 2009; Jordan 2010; USEPA 2007). The National Nanotechnology Institute (NNI) is a United States (US) government program established to provide a framework for collaboration among agencies with interest in nanoparticle research, with collective funding among those agencies totaling nearly US$2 billion for fiscal year 2010 (NSTC 2010). The NNI brings together 25 US government agencies, including: the Environmental Protection Agency (EPA), the Department of Energy (DOE), the National Institute of Health (NIH), the National Science Foundation (NSF), and the National Institute of Standards and Technology (NIST) (PCAST 2010). Other leading nations also have well funded programs to promote nanotechnology research. As of 2003, both Japan and Western Europe funded nanoparticle research at similar levels to the US, with continually increasing funding over the following years (Roco 2002; ENG 2005; Cientifica 2009).

Many of these government programs stem from a need for increased regulation over the expanding use of nanoparticles in commercial applications. In 2007, goods valued at US$147 billion incorporated nanomaterials (Lux Research 2007; Hospitality Trends 2010). An economic estimate prepared by the NSF in 2001 presented an expected increase in the use of nanoparticles to over US$1 trillion per year by 2015 (NSF 2001). There were many assumptions and categorizations used in that estimation that have been disputed, but the underlying principle is clear and certain: nanoparticles are being incorporated into ever increasing programs and products.

Certain industries have been incorporating nanoparticles into products for years. Common applications include such everyday articles as pigments and dyes, batteries, electronics, photographic film developing equipment, construction materials, sporting goods, cookware, and personal care products such as sunscreen and makeup (PEN 2009). This widespread use is rather frightening knowing the prevalent concerns of the scientific community regarding the substantial lack of knowledge of risks, exposure, and fate of nanoparticles (Aitken et al. 2004).

In particular, silver nanoparticles have found an increasing number of uses in recent decades, necessitating an improved understanding of the lifecycle of that silver. According to the Project on Emerging Nanotechnologies, silver nanoparticles are employed in over 250 commercial products, making silver the most prevalent commercial nanoparticle (PEN 2009). That survey likely underestimates the current use of silver in commercial products, due to the increasing role that nanoparticles play in commercial innovation, as well as to products overlooked by the internet-based method of data collection. Even with nanoparticle silver incorporated into only one single commercial product, there exists a strong need to understand the behavior of that silver for immediate and long term environmental and human health considerations.

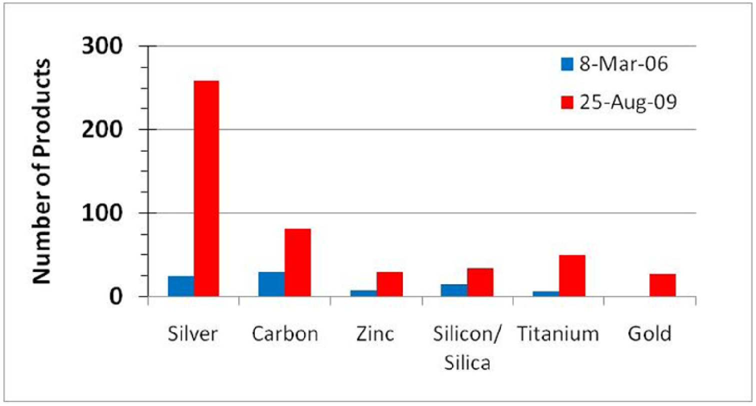

Figure 1: Number of commercial products containing common nanomaterials, according to the Project on Emerging Nanotechnologies

One application of silver nanoparticles is found in a somewhat unexpected role: ceramic drinking water filters produced and used in developing regions. While there are many examples of ceramic water filtration in both developed (e.g., ceramic membranes) and developing regions (e.g., ceramic candle filters) that employ silver for its known anti-microbial properties (Silvestry-Rodriguez et al. 2007), the basis of this research is specifically the ceramic pot filter (CPF). Due to the similarities of these applications, the results of this research may be applicable to a broader range of technologies, but the intention of this research was to focus on ceramic pot filters.

In the ceramic pot filter application, an aqueous solution of nanoparticle, or colloidal, silver is applied to the entire surface area of the filter. There is a general lack of understanding about that additional silver, from its deposition characteristics to its removal behavior, including factors that may impact both deposition and removal.

Studies that have monitored the release of silver have traditionally focused on the microbial efficacy of the overall filter rather than the behavior of the silver itself (Oyanedel-Craver and Smith 2008; Kohler 2009; Lantagne 2001). This approach is valuable in that the end goal of these filters is to produce safe drinking water for the end user by reducing microbial contamination. However, unique insight may be gained by a deeper look into the behavior of the silver itself to allow for improvements in the coating process, better prediction of the lifetime of the coating, and recommendations for filter handling procedures once the coating has been applied.

The investigation presented here employed a highly sensitive mass detection technique to gain insight into the effects of varied pH, turbidity, ionic strength, natural organic matter, and sodium hypochlorite content on the release of silver from a ceramic surface. The results of this study may be most useful for filter handling recommendations, as it was found that influent waters containing even very low concentrations of sodium hypochlorite caused a rapid and substantial removal of the silver coating.

Following this section, the reader will find a Background section which provides basic insight into ceramic pot filters, then an introduction to fundamental theories in support of the experiments performed, as well as a brief description of the analytic techniques employed in this research. A Methods section provides details of the materials, devices, and procedures used during experimentation. The Results and Discussion section presents the data obtained from those experiments. Finally, a Conclusions section provides a contextual overview of the results presented here. Detailed methods and results beyond those presented in the main text are included as Appendices.

Background

While the research presented in this thesis has broad applicability to silver used in many commercial applications, as well as provides basic insight into its groundwater transport characteristics, the true basis for these experiments is that of the silver coating applied to ceramic pot filters (CPF) used in developing regions. A brief explanation of the CPF fabrication procedures is provided below, followed by a short introduction to the theories describing colloid, or nanoparticle, behaviors.

Ceramic Pot Filter Overview

The ceramic pot filter is a household, or point-of-use, water treatment alternative that can provide sufficient drinking water for a family that may not otherwise have access to a safe source of drinking water (Sobsey et al. 2008). Currently, there are over 30 operational factories in 18 different countries with a total production capacity of nearly 80,000 filters per year (Raynor 2009; Clasen 2009; CMWG 2010). Once the ceramic filter is fabricated, it is used in conjunction with a receptacle and spigot as shown in Figure 2 below. The user pours available water into the top, open volume of the ceramic filter. Over a few hours, the water passes through the ceramic element, collecting in the receptacle below. The spigot then provides hygienic access to the filtered drinking water.

Figure 2: Schematic (left) and Image (right) of a ceramic pot filter system, as promoted by Potters for Peace

Pot filters are produced at each factory using almost entirely locally-sourced materials. Local clay is mixed with an organic material (e.g., sawdust) such that when fired at high temperatures, the final ceramic pot contains a network of open pores created by burning off the organic material. According to Potters for Peace, a USA-based non-governmental organization

(NGO) that promotes and facilitates the production of ceramic pot filters, the pores within the ceramic are targeted to a size of 0.6 to 2 micrometers (0.6-2.0 µm) in diameter (PFP undated). A pore structure at that size will remove bacteria (and other relatively large contaminants) through size exclusion, given the characteristic dimension of many bacteria being on the order of 1-2 µm.

After firing, each filter is inspected with quality control tests that, at a minimum, include flow rate testing. If the flow rate is too slow (generally less than 1.5 L/hr), the filter will be rejected for insufficient production capacity. If the flow rate is too fast (generally greater than 3 L/hr), the filter will be rejected for not containing a pore structure of sufficiently small diameter to effectively filter out microbial contaminants (Raynor 2009; Klarman 2009).

Silver as Applied to Ceramic Pot Filters

Each filter that passes the quality control tests will then have a coating of silver applied. Potters for Peace promotes application of around 45 milligrams (mg) of silver per filter, either by brushing a colloidal solution onto the filter or by dipping the entire filter into the silver solution (Nardo 2005). Other production models exist where silver nitrate is applied to the filter instead of nanoparticle silver (Hagan et al. 2009). Another embodiment introduces the silver as a dry powder into the dry mixture of clay and organic material (Klarman 2009). This research focuses on the application method suggested by Potters for Peace.

In many cases, the colloidal silver is brushed onto the filter using a paintbrush to coat the entire usable surface area of the ceramic pot filter. A colloid is any particle ranging from 1 nm to 10 µm in size, suspended in a liquid, but for the purposes of this paper, any colloidal suspension discussed will be limited to a suspension of nanoparticles of 1-100 nm (Gustafsson and Gschwend 1997). Historically, the silver solution recommended by Potters for Peace was sourced as a 3.2 percent colloidal silver solution produced by Microdyn®. Because that product is no longer available, a common product now used in its place is produced by Laboratorios Argenol of Spain. The product can be received as a powder, and then each factory generally mixes a 3.2 percent stock solution of colloidal silver. For each filter, the solution to be applied is prepared by mixing two milliliters (2 mL) of this stock 3.2 percent solution with 250 mL of filtered water, creating a solution of 0.018 percent by weight silver, assuming a silver solids content of 70 percent of the product supplied by Laboratorios Argenol (Lantagne 2001; Nardo 2005; silver data in Appendix C.1: Silver Collargol Data). By applying the entire 252 mL solution evenly to each filter, it is known that each filter receives 45 mg of silver.

Whether the silver is brushed on, or the filter is dipped into a colloidal silver solution (or any other similar method is used in conjunction with a colloidal silver solution), the mechanism of adsorbing onto the ceramic surface should be similar. The silver applied will either adsorb onto the ceramic walls of the filter, or settle into the open pore spaces within the matrix. Some of the deposited silver will be relatively well attached to the ceramic filter, while much of the silver will be very loosely associated and can be readily washed away. For that reason, it is recommended to flush each ceramic pot filter with at least 3 full cycles of water before the collected water is considered safe to drink (Nardo 2005). The concentrations of total silver (ionic and/or nanoparticles) in treated water ranged from around 50 parts per billion (ppb) during the initial flushing phase, decreasing to around less than 1 ppb after repeated use (Lantagne 2001; Bielefeldt et al. 2009)

To date, silver has not been shown to be highly toxic to humans. Silver ions have no known human toxicity, especially at long-term exposure to low concentrations, with the biggest risk being that of a condition called argyria, when the skin turns permanently blue (Brandt et al. 2010). Silver nanoparticles have a calculated toxicity of 10 grams of total intake over a lifetime, which led to the World Health Organization (WHO) maximum level of silver in water of 0.1 mg/L, or 100 ppb (WHO 2004). More recent studies have shown silver nanoparticle toxicity to cell cultures and aquatic life at environmentally relevant concentrations (Hussain et al. 2005; Navarro et al. 2008; Sung et al. 2008; Archer 2008). Based on these studies, silver is actually quite toxic to aquatic life – comparable to mercury in that regard – but the effects of delivery as a nanoparticle are poorly understood (Luoma 2008). Further silver nanoparticle toxicity research is a necessity as the use of these engineered materials becomes more widespread.

When used on these ceramic pot filters, silver has the potential to substantially reduce the microbial concentration of drinking water. As mentioned above, it also has the potential to cause harm, in that it is released from the ceramic filter and will be ingested by the end-user. This double effect is quite similar to concerns surrounding other commercial applications of silver nanoparticles (Ju-Nam and Lead 2008; Nowack and Bucheli 2007; Stone 2009). In all cases, it is important to fully understand the processes involved in order to better control the effects, both positive and negative.

Ceramic Pot Filter Ceramic Characterization

There have been a few efforts to characterize the ceramic structure of ceramic pot filters. A glimpse into the data previously collected is provided here, along with a few additional images and insight included in the Results and Discussion section. What is most striking about the ceramic characterization data is the wide range of results obtained. Much of that variability can be attributed to geographic differences (given the use of locally-sourced clays), but there are many other factors inherent in the production process that can influence the ceramic matrix. Some of the production variables include: dry clay type, composition, particle size, and condition; organic material type, composition, particle size, and condition; mix ratio of clay-to-organic material; forming and drying processes during fabrication; and especially the temperature profile during firing.

The extreme variability during production is best governed through the use of knowledgeable advisors to establish the fabrication procedures, along with a well-designed, consistently implemented quality control program. Even with those controls in place, it is quite difficult to provide a set of characterization parameters that will capture the state of every ceramic pot filter being produced. Even with this awareness, a deeper look into the ceramic microstructure is important for an understanding of the defining characteristics of the ceramic substrate with which the silver nanoparticle coating will interact.

Scanning Electron Microscopy

Scanning electron microscopy (SEM) is a means to capture images with resolution readily achievable down to 10 nm and less (Russell et al. 2004). The images are an excellent way to visualize features of the ceramic microstructure of ceramic pot filters. Furthermore, through the use of different electron detectors, unique insight can be gained into either the surface topography or the relative composition of the specimen (Russell et al. 2004).

SEM images of ceramic pot filters produced by a Potters for Peace sponsored factory were made widely available in 2001 (Lantagne 2001). In that work, it was found that many of the open features of the ceramic pot filter are much larger in size than the 1 µm target pore size; in fact, cracks and voids with dimensions up to 200 µm were found. Other studies have confirmed these larger features exist in almost all ceramic pot filter specimens (van Halem 2006; Klarman 2009).

While these features are much larger than the pore size targeted for size exclusion of bacteria, it does not mean that the filters are any less effective than proven previously. It simply means (1) that these larger features must neck down at some point to a channel on the order of 1 µm wide (thereby still allowing for size exclusion), (2) that these larger features are closed pores and have no exit for any bacteria, (3) that the bacterial efficacy of ceramic pot filters is governed by other mechanisms besides size exclusion, or (4) some combination of effects related to those listed.

Energy Dispersive X-ray Spectroscopy

Another technique employed in previous ceramic characterization studies was that of energy dispersive X-ray spectroscopy (EDS or EDX). This method is commonly combined with the SEM as a means to detect the elemental composition of the specimen being studied. Consistent with expected composition given the starting materials, ceramic filters were found to be comprised of an alumino-silicate matrix (Lantagne 2001). This (intentionally) highly-porous alumino-silicate matrix is formed during the vitrification of the constituent materials during the firing process, with a 6-10 hour hold at peak temperatures near 900 degrees Celsius (UNDP c2004).

Due to volume interference effects that are beyond the scope of this paper, EDS is not a useful technique to determine the location or distribution of deposited silver nanoparticles.

Porosimetry

The porosity characteristics of each ceramic pot filter are greatly affected by the type and size of the organic material incorporated into the filter body. Studies have been conducted using Archimedes principle to determine the percentage of open porosity by comparing the mass of the filter dry, saturated, and submerged (van Halem 2006; Klarman 2009). Filters from Nicaragua, Ghana, and Cambodia were tested, with determined porosities between 30 and 40 percent (van Halem 2006). Interestingly, a filter produced in Nicaragua tested without a colloidal silver solution yielded 35 percent porosity.

These values agree with those reported for cored sections of pot filters from Nicaragua, which had 40 percent porosity on average (Kohler 2009). Kohler found that cores taken from the bottom of the filter had a significantly higher porosity ($p=0.029$) than cores taken from the side walls.

Table 1: Summary of Porosimetry and Density data from ceramic pot filters

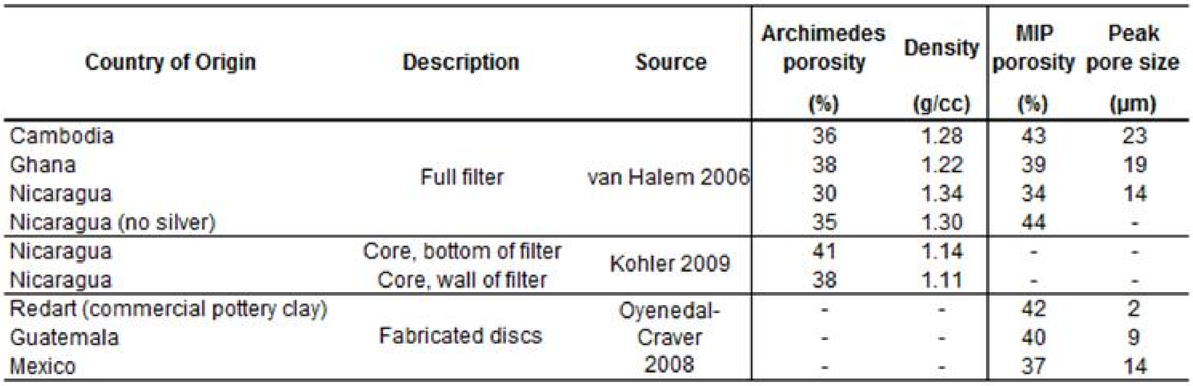

Country of Origin	Description	Source	Archimedes porosity (%)	Density (g/cc)	MIP porosity (%)	Peak pore size (µm)
Cambodia	Full filter	van Halem 2006	36	1.28	43	23
Ghana			38	1.22	39	19
Nicaragua			30	1.34	34	14
Nicaragua (no silver)			35	1.30	44	-
Nicaragua	Core, bottom of filter	Kohler 2009	41	1.14	-	-
Nicaragua	Core, wall of filter		38	1.11	-	-
Redart (commercial pottery clay)	Fabricated discs	Oyenedal-Craver 2008	-	-	42	2
Guatemala			-	-	40	9
Mexico			-	-	37	14

Similar results were obtained by Mercury Intrusion Porosimetry (MIP). Using this technique, filter porosities were found to be 34 to 44 percent (van Halem 2006; Oyenedal-Craver 2008). MIP provides more specific data of the porosity size distributions. The peaks of the distribution curves were at pore diameters of 14, 19, and 23 µm for the Nicaraguan, Ghanian, and Cambodian filters, respectively (van Halem 2006). A summary table of these results is included here as Table 1.

As with the open features seen during SEM analysis, it is apparent that many of the pores within ceramic pot filters are much larger than the targeted diameter of 1 µm. This suggests that additional importance may be placed on the role of the silver coating applied to each filter.

Particle Size Penetration

Microsphere particles, kaolin particles, and naturally occurring surface water particles have been used to detect the size exclusion capabilities of ceramic pot filters. It was found that particles greater than 8 µm diameter were still passed through the walls of the filter, but at a substantial reduction from influent concentrations (Bielefeldt et al. 2010). That microsphere study definitively showed that the porous filter walls were much more effective at removing larger particles than smaller diameter features. Again, this can be interpreted as adding emphasis to the importance of the silver coating for the microbial efficacy of ceramic pot filters.

Quartz Crystal Microbalance (QCM) Introduction

Piezoelectric Effect

The quartz crystal microbalance (QCM) is one technique used to study surface interactions. QCM devices are commonly employed in processes where high mass sensitivity is required, such as during pharmaceutical production. The fundamental piezoelectric behavior, integral to QCM measurements, was described as early as the 1880's, most notably by Jacques and Pierre Curie (Ward and Buttry 1990; Mould 2007). In that seminal work, it was found that mechanical stress applied to crystals (e.g., quartz) created a proportional electrical potential. The Curies and others also experimented with the reverse effect, where an electrical potential applied across a crystal creates a mechanical strain within the structure of the crystal (Buttry and Ward 1992; O'Sullivan and Guilbault 1999).

The piezoelectric effect can be harnessed within an oscillating circuit, in which an alternating current is applied across a crystal, in turn creating a vibration within the crystal as the quartz mechanically strains in alternating directions in response to the applied current. Oscillating circuits are very precise and reliable oscillators by careful preparation of the crystal itself and the electronic controls. In

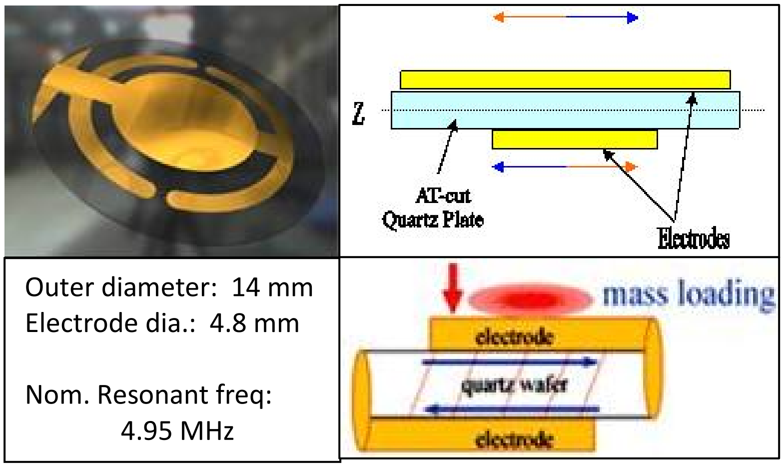

Outer diameter: 14 mm
Electrode dia.: 4.8 mm

Nom. Resonant freq:
4.95 MHz

Figure 3: Image and dimensions of common QCM sensor geometry (left) and schematic showing direction of shear mode oscillation without (upper right) and with (lower right) additional mass deposited.

most QCM measurements, quartz material that is cut along the “AT” material axis is selected as the sensor material due to its excellent temperature stability around room temperature and its sensitive vibration modes (Rodahl 1995a).

Figure 3 shows a common sensor geometry, in which the thickness of the quartz sensor determines the fundamental resonant frequency (Lu 1975). An electrode is deposited onto each flat surface of the disc-shaped sensor. An alternating current is applied to those opposing electrodes, which induces an alternating electric field through the thickness of the quartz sensor. That changing electric field causes piezoelectric strain within the quartz sensor. Data recorded by the QCM is the resonant frequency of each sensor, or, in other words, the frequency at which each sensor has the lowest impedance to that oscillating strain field.

In the case of the AT-cut quartz, the piezoelectric oscillations produced are shear-mode strains captured within the overlapping surface area of the electrodes (Ward and Buttry 1990).

Multiple Resonant Frequencies, or Harmonics

Physical resonance behavior is a phenomenon found in many everyday applications, from the quartz movement in watches to musical instruments. Just as guitar or violin strings have multiple harmonics that create multiple audible pitches (related to octaves, in the musical case), a quartz device has multiple harmonics of its fundamental resonant frequency. Due to the reflection characteristics of the acoustic wave within the quartz sensor, only the odd multiples of the fundamental resonant frequency are detectable (O’Sullivan and Guilbault 1999).

The primary difference between the multiple harmonics is the penetration depth into the sample residing on the surface of the sensor. The penetration depth is proportional to the decay length of the frequency in the medium of interest, where higher frequencies, with shorter wavelengths, tend to decay much more rapidly than lower frequencies (Rechendorff et al. 2007).

Equation 1: Decay length for each harmonic frequency (Rechendorff et al. 2007)

$$\partial_N = \left(\frac{\eta}{\pi \cdot f_N \cdot \rho} \right)^{1/2}$$

δ_N is the decay length,
N represents the harmonic,
ρ is the density of the medium.

Given known visco-elastic properties of the sample material, a theoretical penetration depth for each harmonic can be calculated. Equation 1 is used in the decay length calculation (Rechendorff et al. 2007). This equation contains terms specific to the properties of the oscillator (i.e., quartz) as well as the fluid medium surrounding the oscillator. For example in water at room temperature, the decay lengths for each odd harmonic from one through thirteen are shown in Table 2 below. Decay length values for the same sensor in air are also given for perspective of the resonance damping caused by the higher density-viscosity product. More details regarding the magnitude of expected frequency and dissipation shifts are found below, in the QCM Measurement and Analysis section.

Table 2: Theoretical decay lengths of each harmonic frequency of interest for both Air and Water at 22° C

Harmonic	**Air δ_N (nm)**	**Water δ_N (nm)**
1	10300	248
3	5900	143
5	4600	111
7	3900	94
9	3400	83

Another major difference between the multiple harmonics is the radial amplitude distribution of the different frequencies. Basically, a higher frequency will produce responses from a more focused area than a lower frequency. The radial distribution can be a substantial factor in measurements requiring the highest mass sensitivity, but the effect can be lessened by considering harmonics at lower frequencies. For instance, considering the effects of sample placement on the electrode surface, models have shown a few percent difference in frequency shifts when the sample was perfectly centered versus tangentially located to the outer edge of the electrode (Lu et al. 2004). This effect is most noticeable at the higher frequencies (the model by Lu was run at a nominal frequency of 35 MHz), but the deviation from ideal frequency shift is even less at lower frequencies (Lu et al. 2004).

QCM Measurement and Analysis

Frequency Response in Relation to Mass in a Vacuum

Sauerbrey adopted piezoelectric resonance behavior of quartz crystals into a measurement technique with his work in 1959. In that, Sauerbrey shows that the change in resonance frequency is directly proportional to the quantity of mass added to the sensor's surface, provided that the mass is a thin, uniform film that is rigidly attached to the quartz crystal. Those assumptions are based on the derivation of the Sauerbrey equation (Equation 2), in which additional mass on the surface of the sensor is treated as an extension of the sensor itself. Certainly, the additional mass must be well attached to the surface for the sensor to detect any changes. Also, the mass must behave similarly to the resonant properties of the quartz sensor itself, or else the equation will not accurately describe the mass added.

As can be seen by Equation 2(a), Sauerbrey derived a direct, linear proportion between a change in frequency and the deposited mass causing that shift (shown more clearly by reduction to Equation 2(b). Note the terms in the equation have little to do with any characteristics of the specimen, but rather the constant of proportionality is dependent on the sensor's resonant frequency and physical properties (namely, shear modulus and density). It is also important to note that the Sauerbrey correlation is often used to arrive at an areal mass due to the inclusion of surface area in the equation. This is much less of a concern for films with good uniformity, but can cause issues in interpretation for more discrete, particle-like mass additions.

The Sauerbrey correlation is a useful description of deposited mass when the criteria mentioned above are met; another criterion bounding its application is that the shift in frequency caused by the deposited mass should be less than two percent of the baseline resonant frequency of the sensor (SRS 2005). Exceeding that mass deposition limit was addressed by the Z-match method, which has been shown to be a reliable mass correlation up to 40 to 50 percent frequency shift from baseline (Lu and Lewis 1972).

Equation 2: Change in frequency related to change in mass for each harmonic frequency (Sauerbrey 1959)

$$\Delta f_N = \frac{-2 \cdot \Delta m \cdot f_{N,0}^2}{A\sqrt{\rho_q \mu_q}} = -\frac{2 \cdot f_{N,0}^2}{A\sqrt{\rho_q \mu_q}} \cdot \Delta m \qquad \text{(a)}$$

$$\Delta f_N = -c_N \cdot \Delta m \qquad \text{(b)}$$

Δf_N is the frequency shift,
N represents the overtone (or harmonic),
ρ_q is the density of the quartz,
μ_q is the shear modulus of the quartz,
A is the active area of the electrodes,
c_N is a constant for each sensor,
Δm is the associated change in mass.

As an example of QCM detection limits according to these models, consider a sensor with a 5 MHz resonant frequency. Under well-controlled conditions, a one Hz shift is reliably detectable by QCM measurement. According to the Sauerbrey equation, that one Hz shift would be caused by 6 ng/cm^2 of mass deposited on the surface. Assuming a common crystal geometry where the working electrode has an area of 0.24 cm^2, the minimum detectable mass is on the order of 1-2 ng. An upper limit for the Sauerbrey correlation may be found by assuming a frequency shift of two percent of the nominal resonant value. At that 100 kHz frequency shift, the Sauerbrey equation yields a deposited mass of 600 µg/ cm^2 corresponding to a deposited mass on the order of 150 µg.

Frequency Response within Fluid Environments

Much of the foundation work towards QCM measurements was hypothesized and/or conducted assuming the sensor was in a vacuum, thereby eliminating any potential effects from an ambient fluid, whether air or water. Kanazawa and Gordon published an equation to describe this damping in 1985 which incorporated similar crystal properties as the Sauerbrey equation, but additionally considered the density and viscosity of the surrounding fluid. The density and viscosity of the surrounding fluid will act to dampen the resonant frequency of the quartz sensor, just as an additional mass does. This more thorough description of expected QCM behavior substantially increased the potential applications of the QCM instrument.

Equation 3: Frequency shift due to liquid loading (Kanazawa and Gordon 1985)

$$\Delta f_N = -f_{N,0}^{3/2} \cdot \left(\frac{\rho_L \eta_L}{\pi \cdot \rho_q \mu_q} \right)^{1/2}$$

Δf_N is the frequency shift,
N represents the overtone (or harmonic),
$f_{N,0}$ is the unloaded resonant frequency,
ρ_q is the density of the quartz,
μ_q is the shear modulus of the quartz,
ρ_L is the density of the liquid,
η_L is the viscosity of the liquid.

As in the equation derived by Sauerbrey, the theoretical frequency shift is dependent on the resonant frequency of the unloaded sensor, as well as physical properties of the sensor itself. The shift due to a liquid is also dependent on the density and viscosity of the liquid in contact with the sensor.

Frequency response of a deposited mass on the surface of a QCM sensor operating in a liquid may be treated as two superposed and separate effects, that due to the deposited mass and that due to the liquid damping (Kanazawa and Gordon 1985). That is to say, given a certain decrease in resonant frequency caused by a deposited mass and given a certain decrease in resonant frequency caused by submersion in a viscous liquid, when that sensor with deposited mass is submerged in that liquid, the total expected frequency shift is theoretically the sum of the two components (i.e., mass and liquid).

Of course, in application there are deviations from theoretical frequency shifts due to neglected effects. One major effect can be attributed to the surface roughness associated with both the surface of the sensor and the surface of the deposited mass. Liquid-based surface roughness effects on QCM measurements have been modeled and validated through experimentation, finding that when surface roughness was at 3 nm rms, there was no detectable difference in the frequency response relative to an ideal, flat surface. However, when surface roughness was 33 nm rms, the effects on frequency shift were almost 10 percent of the theoretical shift for the first harmonic, and nearly 20 percent for the seventh harmonic (Rechendorff et al. 2007). At each harmonic, the measured data showed a larger shift than the theoretical frequency shift due to a coupling effect between the cratered surface and the surrounding liquid.

The principal of superposition of frequency shifts will hold most accurately when the additional mass is deposited in such a way as to prevent, or minimize, its release. In the case of the experiments presented here, there is an expectation of silver release from the surface. Because of that, the flow experiments were analyzed carefully to determine the effects of varied water quality on the rate of release. The theoretical descriptions provided in this Background section served as a basis for analysis.

Electrical Resistance Response to a Fluid

The electrical resistance of the circuit may be recorded as an independent verification of the resonant frequency when the measurement is being conducted on a fluid (Martin et al. 1991). The resistance is sensitive to changes in the density and/or viscosity of the material being measured, and is much less sensitive to mass deposited on the sensor surface, provided that the mass approaches the Sauerbrey assumptions (thin, uniform, rigid, and well attached film). For that reason, this parameter is a useful measurement for liquid measurement, but is relatively meaningless when analyzing a rigid film, as the electrical resistance will not behave substantially different than it would for the sensor alone.

Equation 4: Resistance shift due to liquid loading (Martin et al. 1991)

$$\Delta R_N = \left(\frac{N \cdot \omega_s \cdot L_u}{\pi} \right) \cdot \left(\frac{2 \cdot \omega_s \cdot \rho_L \cdot \eta_L}{\rho_q \cdot \mu_q} \right)^{1/2}$$

ΔR_N is the resistance shift,
N represents the overtone (or harmonic),
ω_s is the angular frequency at resonance,
L_u is the inductance for the unloaded sensor,
ρ_q is the density of the quartz,
μ_q is the shear modulus of the quartz,
ρ_L is the density of the liquid,
η_L is the viscosity of the liquid.

The QCM machines employed for these experiments were not capable of returning a value for the inductance of the sensor. Impedance or network analyzers can provide that measurement. Values presented within this document for expected resistance shifts were calculated using published values for the inductance of the sensors of around 40 mH (SRS 2005).

Frequency and Resistance Shift Values for Water

Theoretical frequency and resistance shifts can be calculated for water flowing across the surface of a sensor (Kanazawa and Gordon 1985; Martin et al. 1991). Using density and viscosity values for water at room temperature (see table in Appendix B: Theoretical QCM Response to Water), the expected frequency shift of the first harmonic is 710 Hz and the expected resistance shift is 360 Ohms.

Scaled Frequency Response of QCM in Water

All results are presented in a scaled frequency format, unless otherwise stated. Data is recorded in absolute frequencies, and then scaled by normalizing by each harmonic. For instance, in Table 3, the third harmonic shows an absolute frequency decrease of 1191 Hz from baseline. The scaled frequency shift is found by dividing 1191 Hz by 3, since this is the third harmonic. The result is a third harmonic scaled frequency decrease of 397 Hz, as shown in Table 3.

Table 3: Theoretical frequency and dissipation shifts for a 4.95 MHz sensor in water at 22° C, relative to vacuum.

Harmonic N	**Absolute Δf_N (Hz)**	**Scaled Δf_N (Hz)**	**ΔD_N (10^6 x arb. units)**
1	-687	-687	278
3	-1191	-397	160
5	-1537	-307	124
7	-1819	-260	105
9	-2062	-229	93

Table 4: Theoretical frequency and dissipation shifts for a 4.95 MHz sensor in air at 22° C, relative to vacuum.

Harmonic	**Absolute Δf_N (Hz)**	**Scaled Δf_N (Hz)**	**ΔD_N (10^6 x arb. units)**
1	-34	-34	14
3	-59	-20	8
5	-77	-15	6
7	-91	-13	5
9	-103	-11	5

Dissipation of the Amplitude of Oscillation

Another independent parameter that can provide information about the viscosity and elasticity of any material being analyzed is dissipation. Dissipation is a term that describes the energy loss versus energy storage of the sensor and any material in contact with the sensor (Rodahl 1995a). The quantity is determined through similar electronic controls as are necessary for the detection of resonant frequency. Once the sensor is being driven at its resonant frequency, the alternating current driving the piezoelectric oscillation is stopped while the amplitude of oscillation continues to be monitored (Hook 1997).

For a rigid material, with extremely low elasticity, such as quartz, the dissipation will be a very low quantity as the oscillations will not be substantially damped. A more elastic material, or highly viscous material, will have the effect to dampen the residual oscillations of the sensor through energy dissipation, yielding a much higher dissipation factor. Schematic representations of these effects are included as Figure 4, with tabulated theoretical values included in Table 3.

Equation 5: Dissipation shift due to liquid loading (Rechendorff et al. 2007)

$$\Delta D_N = 2\frac{f_N^{1/2}}{N}\left(\frac{\rho_L \cdot \eta_L}{\pi \cdot \rho_q \cdot \mu_q}\right)^{1/2}$$

ΔD_N is the dissipation shift,
N represents the harmonic,
f_N is the unloaded resonant frequency,
ρ_q is the density of the quartz,
μ_q is the shear modulus of the quartz,
ρ_L is the density of the liquid,
η_L is the viscosity of the liquid.

Modeling Frequency and Dissipation Responses

There are a number of analytical approaches that have been developed to model frequency and dissipation responses of the QCM. Most fundamental of these is the Sauerbrey correlation mentioned above. Some approaches, such as the Z-match method (Lu and Lewis 1972) were direct improvements over the Sauerbrey correlation, while other approaches handle more complexities of frequency response. One of these models is the Voigt model, which is based on an elasto-mechanical model of the sensor and any material in contact with the surface (Voinova et al. 1999). The Voigt model captures visco-elastic responses with much more accuracy than the Sauerbrey equation or any alternative approach that does not allow the viscosity of the contact material to be considered. A schematic of the Voigt physico-mechanical model is included as Figure 5 (Jaiswal 2010). As explained by Jaiswal, the frequency and dissipation shifts are dependent on the density, viscosity, elasticity, and thickness of the film, on top of the analogous sensor properties inherent in these calculations.

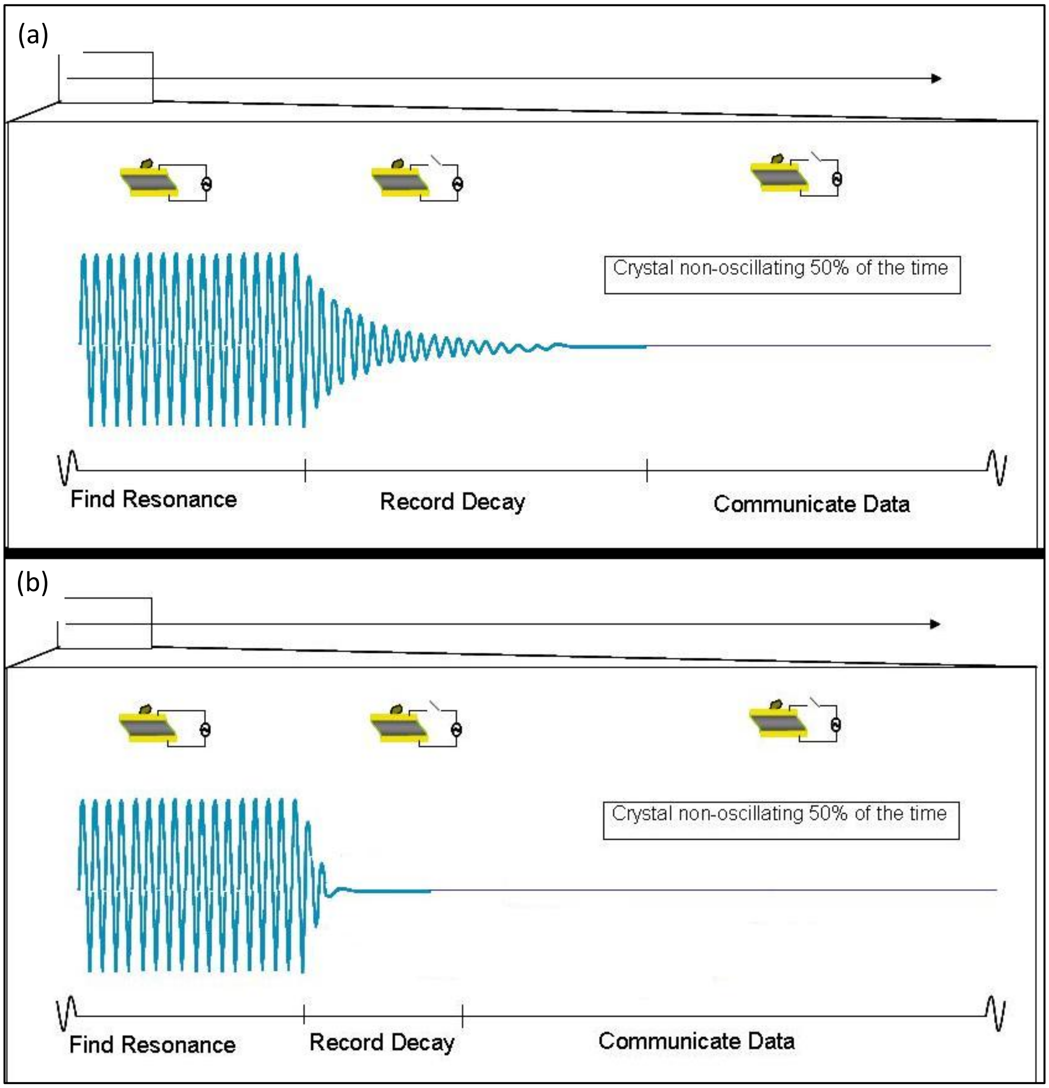

Figure 4: Frequency output schematic during QCM measurement of frequency and dissipation shift. Image above (a) shows lower dissipation associated with rigid mass in contrast to the higher dissipation of a visco-elastic mass (b). (Adapted from Q-sense product literature)

Keeping in mind that the dissipation factor is a measure of the visco-elastic properties of the material being analyzed, the dissipation factor can be used to determine the appropriateness of the Voigt model for the data collected. The Voigt model should only be employed when the shift in dissipation (increased by a factor of 10^6) is at least 5 to 10 percent of the frequency shift in Hz (Jaiswal

2010). At dissipation shifts below that threshold, the viscosity that must be input into the Voigt model approaches infinity in order to represent the stiff, inelastic material, disrupting the modeling equations.

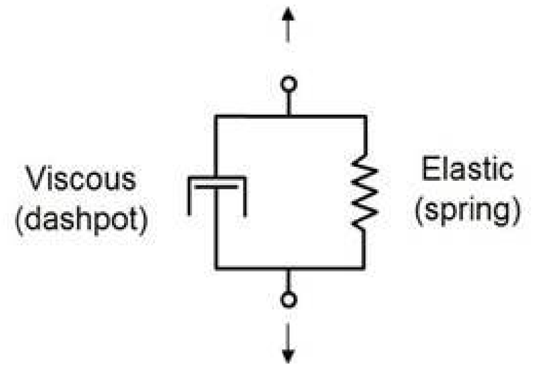

Figure 5: Physico-elastic Voigt model schematic.

While the Voigt model attributes any departure from the ideal Sauerbrey response to visco-elastic behavior, some research points to a hydrodynamic effect as a cause (Rojas et al. 2008). In the case of a heterogeneous ferritin film submersed in a fluid, Rojas et al. were able to show that the ratio of bandwidth shift (related to dissipation) to frequency shift correlates with theoretical frequency dependence for hydrodynamic-induced responses under certain conditions. Specifically, by incorporating an atomic force microscope (AFM) with QCM, It was shown that an unpurified ferritin film, containing relatively large agglomerations of ferritin (~4 times the size of single particles), responds to the oscillations of the QCM in a significantly different manner than the response of the purified ferritin film (Rojas et al. 2008).

Advantages of QCM Measurements

The advantage of QCM measurements is that of monitoring mass, viscosity, and density properties of a sample *at the surface* of the QCM sensor. This provides insight that may be otherwise lost by simply analyzing bulk properties of the specimen. Furthermore, the exceptional mass sensitivity of the QCM device is a welcomed (required, perhaps) feature when investigating surface interactions of nanoparticles in an aqueous environment.

The experiments presented here were designed to represent conditions of the colloidal silver applied to ceramic water filters, but a broader understanding of the expected behavior of nanoparticles on a submerged surface is important to better assess the data collected.

Nanoparticle-Surface Interactions

The release of nanoparticles from a surface is related to solution-based colloidal theory, but traditional colloid theories often fail to describe all of the effects between the nanoparticle, the surface, and the bulk fluid.

Solution Property Effects

Modeling of colloids in solution is often left to the DLVO (Derjaguin, Landau, Verwey, and Overbeek) theory. The DLVO theory combines two forces associated with particles in solution: (1) van der Waals attraction and (2) electrostatic repulsion from the double layer of counterions surrounding each particle (Benjamin 2002).

The van der Waals force is due to the attraction or repulsion of dipoles, whether permanent or induced. This force also generally incorporates a dispersion force attributed to London that describes the interaction between non-polar molecules (Cosgrove 2010).

The double layer force is a description of the attraction of ions to the surface of a charged particle (Cosgrove 2010). As the surface of the particle may be charged either at its standard state, or by the loss of surface groups, it tends to attract counterions from solution until the surface charge is effectively balanced. As the counterions build up around the surface of the particle, there is a region defined by the volume containing those counterions. That region is termed the electrical double layer. The electrical double layer has a characteristic dimension based on the type of electrolyte in solution, the concentration of ions in solution, the valence state of the ion, the pH and natural organic matter content of the solution, as well as electrical considerations of both the particle and fluid (el Badawy et al. 2010; Benjamin 2002; Diegoli et al. 2008; Ju-Nam and Lead 2008; Quevedo and Tufenkji 2009).

Zeta-potential is related to the electrical potential between the charge of the bulk fluid and the charge of the electrical double layer surrounding the particle (Benjamin 2002). In general, any particle with an absolute value of charge greater than 25-30 mV is considered to be a stably dispersed colloid in suspension (Cosgrove 2010).

The zeta-potential of any particle is affected by the pH of the bulk fluid. Given that pH is a measure of the available protons or hydroxide species, the effect on the zeta potential is similar to the electrical attractions mentioned in the double layer discussion above. Then, by attracting those counterions from solution, the electrical charge surrounding the particle will change, causing a shift in the zeta-potential (Benjamin 2002).

A term related to the zeta-potential of a particle is the isoelectric point (IEP). This number is the pH at which the zeta-potential of that particle measures zero. It is based on the interaction of the free protons or hydroxides species with the charged particle. While the IEP is controlled by factors related to the composition of the solution, it is also important to know the characteristics of the nanoparticle, including a physico-chemical description of its surface. Silver nanoparticle isoelectric points have been reported across a wide range of pH values, depending strongly on any capping agent, or surfactant, in place around the silver nanoparticle (el Badawy et al. 2010).

Ionic strength and type of electrolyte are yet other parameters that have an effect on the zeta potential of dispersed particles. Every ion has a certain electrical charge that can interact with a particle in suspension. The concentration and type of ion in solution play a major role in zeta-potential. Divalent ions will often interact more strongly with a charged particle in suspension, thereby having a larger effect on the zeta-potential of the colloid. It has been shown that silver nanoparticles in suspension maintained stability in the presence of sodium (monovalent) ion, while the zeta potential was dropped to a point of instability when calcium (divalent) ion was present (el Badawy et al. 2010).

The composition of the solution is important for the effects it may have on a suspended particle. As discussed, it can affect the stability of the colloid. The solution composition can also have direct effects on chemical speciation, potentially dissolving a colloid or precipitating out from the ionic form. One of the most important considerations for silver nanoparticles is that of chloride. The solubility of silver chloride is quite low, saturating pH-neutral water at silver (and chloride) concentrations of approximately 0.013 mM, resulting from a solubility product of 1.8×10^{-10} (Benjamin 2002). Instead of dissolving into solution, the silver and chloride tend to bind together to form a precipitate. This effect has been shown in a number of studies (el Badawy et al. 2010; Brauner et al. 2003). For that reason, the inclusion of chloride has been avoided when not considered as a parameter of interest.

Colloidal Property Effects

The effects of solution chemistry are compounded by the nature of the particle itself, and whether a capping agent or stabilizing compound surrounds the particle. Numerous studies have shown the dramatic effect that the physico-chemical properties of the nanoparticle itself can have on the stability and agglomeration behavior of nanoparticles in suspension (el Badawy et al. 2010; Geranio et al. 2009). While trends can be noted from these various studies, it is extremely important to relate any of these concepts back to the particular nanoparticle under investigation with a thorough characterization of the physico-chemical state of that specific nanoparticle.

Surface Property Effects

An initial consideration should be that of the attachment mechanism of the nanoparticle to the surface of interest. Studies have shown the effects of surface properties on nanoparticle attachment, often times in association with fouling of membranes. Interestingly, surface roughness can play a dominant role in deposition behavior, even more so than the physical and chemical state of the surface, however numerical models show the importance of zeta potential (Vrijenhoek et al. 2001; Hoek et al. 2003).

Electrostatic interactions between the surface and the colloid still play a major role in both deposition and release characteristics of a nanoparticle. The electrical state of the surface is controlled to a certain extent by the solution composition (Ryan and Gschwend 1994). This effectively places a double emphasis on the solution composition in that it not only controls the behavior of particles in suspension, but it also controls the affinity of the particle interaction with the submerged surface. To complicate the matter even further, DLVO theory breaks down at particle separation distances less than around 4 nm, so does not successfully portray particle-surface interactions (Ryan and Gschwend 1994).

In the case of the ceramic water filters, that mechanism is not well-understood, deserving further investigation in the future. Recall that the substrate is an alumino-silicate matrix and that the silver nanoparticles are applied as an aqueous colloidal solution. The silver will be adsorbed onto the walls of the ceramic filter, or perhaps captured into the smallest of pores within the ceramic matrix, suggested by porosimetry data (van Halem 2006). It is suspected that the surface charge of the deposited silver will tend towards positive as silver cations may be generated at the surface of each particle, or agglomeration of particles (Morones et al. 2005). It is likely that the surface charge of the alumino-silicate matrix is slightly negative, as that is a common state for materials comprised of the same constituents, as well as a likely result of natural organic matter (NOM) that may have been associated with the filter walls during quality control flow rate testing. Without fully understanding the relationship between the alumino-silicate matrix and the silver nanoparticles, an approximation through the use of a representative inorganic substrate, silica, will be employed for the experiments presented here.

Silica surfaces have been used in studies to represent a sand grain, such as may be encountered in groundwater transport (Quevedo and Tufenkji 2009). The isoelectric point for crystalline silica is on the order of 1.5 to 3, whereas amorphous alumino-silicates (representative of ceramic pot filter composition) often show an isoelectric point of 4-5 (Jara et al. 2005). Silica is the best commercially available representative surface for the alumino-silicate matrix of ceramic water filters.

QCM Detection of Nanoparticle-Surface Interactions

Quartz crystal microbalance measurement techniques are well suited to monitor and record interactions of nanoparticles with surfaces. This experimental approach stems directly from the initial measurement research pioneered by Sauerbrey, Kanazawa, Gordon, Martin, and others. Over the previous decades, there have been advancements to broaden the applications in which the QCM may find use. Specifically, initial measurement research was strictly based on the measurement being conducted in a vacuum environment, which to this day is still quite applicable to certain QCM uses (e.g., monitoring thickness during film deposition processes). Advancements in understanding the theories behind the QCM measurement platform have led to its use in a surrounding fluid medium, including air, water, and more viscous compounds such as resins and oils. These opportunities are being expanded as further research is conducted towards nanoparticle behavior under controlled conditions.

Quantum dots are one example of a manufactured nanoparticle that have been analyzed under various conditions using the QCM. Quantum dots have found uses in a variety of commercial applications, but are most known for their encased metal structure, where the coating can be specifically designed to be compatible with a target; specifically, this has been useful for biological deployment of the metal core of the quantum dot (Quevedo and Tufenkji 2009). The functional coating applied to a quantum dot will define its surface properties and size, and the size of the contained core will often influence the electrical and optical properties of the quantum dot. For that reason, each quantum dot needs to be specifically characterized, but in general, this class of material is manufactured to a size of between 2 and 1000 nm, depending on coatings applied.

It has been shown that ionic strength is a major factor in the deposition rate of quantum dots flowing in the solution of interest, depositing onto a silica-coated QCM sensor (Quevedo and Tufenkji 2009). Quantum dots comprised of carboxyl-terminated cadmium-telluride at a manufacturer specified diameter of 10 nm (hydrodynamic diameters determined from dynamic light scattering to be 50 to 200 nm) were studied. The deposition rates of those quantum dots onto a silica-coated sensor were different when the ionic strength was due to either a monovalent ion (potassium) or a divalent ion (calcium), with the divalent ion causing a significantly faster rate of deposition. The rate of release from the silica surface was also determined, with similar results to deposition rates, in that the monovalent salt had much higher propensity to remove the quantum dots from the surface while the rate of release due to calcium was much slower (Quevedo and Tufenkji 2009). This suggests that the divalent ion had a stronger effect of forcing the quantum dots onto the silica surface than the monovalent ion. This agrees with what would be predicted by the suspension behavior of that quantum dot according to DLVO theory.

The QCM platform has also been used to detect *Cryptosporidium parvum (C. parvum)* in water samples containing natural interferents, such as dissolved organic matter (DOM), other microbes, microbial secretions, and other broadly categorized natural colloidal particles (Poitras et al. 2009). *C. parvum* is a protozoan oocyst approximately 2-3 µm in diameter when viable, with a negative surface charge at relevant pH values and an isoelectric point at around 2.5 (Drozd and Schwartzbrod 1996; Poitras et al. 2009). In the work by Poitras et al., the dissipation was determined to be a better data source as a biosensor than the frequency shifts. Recall that the dissipation is directly related to the density-viscosity product of the material deposited on the surface. Microbes have a detectable viscosity that will affect the dissipation readings greater than the frequency. The authors were able to reliably detect *C. parvum* in some cases, but given interferents that mimic the viscosity effects, the QCM detection method was difficult to decipher. Of note in that same study, *Escherichia coli* (*E. coli*) flowing across the surface of the QCM sensor was not sufficient to cause detectable shifts in either frequency or dissipation (Poitras et al. 2009).

Research Objectives

The goal of this research was to determine and understand the effects of water quality on the release of silver nanoparticles from an inorganic substrate, using a highly sensitive acoustic resonance detection system to monitor the release under various influent water conditions. The results of this investigation will be useful for the community of fabricators and end-users of ceramic water filters in that these data will aid in determining the useful lifetime of the anti-bacterial silver coating applied to ceramic water filters. Furthermore, these data can be useful to assess the appropriateness of this technology given available water quality.

The research objectives were:

1. Develop an experimental approach based on a quartz crystal microbalance (QCM) to monitor, in real-time, the rate of release of silver nanoparticles from a ceramic substrate.

2. Measure the impact that water quality parameters, specifically pH, turbidity, ionic strength and natural organic matter (NOM), have on the rate of release of silver nanoparticles from a ceramic substrate.

3. Measure the effect that water containing sodium hypochlorite has on the rate of release of silver nanoparticles from a ceramic substrate.

The results presented in this document include data relevant to these objectives. More detailed discussion of the implications of the data may be found in the Results and Discussion section of this document, with additional and more detailed results included as Appendices.

Methods

Silver Solution Preparation

Unless otherwise stated, all silver used in these experiments was the commercially available product Collargol Colloidal Silver French IX Edition, produced by Laboratorios Argenol of Spain (product info in Appendix C.1: Silver Collargol Data).

The majority of the experiments were performed using a silver solution representative of the colloidal silver solution used during production of ceramic pot filters, which for the purposes of this report will be called the "application solution". In this laboratory investigation, the water for the solution was purified in order to minimize additional water quality variables for each experimental run. However, the water used during actual fabrication of ceramic pot filters will generally be filtered (not purified) water, and will likely contain many other constituents from sources of contamination as well as natural organic matter. The effects of these constituents on the colloidal silver solution were not studied in this work.

The 3.2 percent stock solution, similar to the stock solution traditionally used as a starting point by production facilities worldwide following the Potters for Peace recommendations, was prepared by carefully mixing 250 mL of Millipore ultrapure water with 8 g of Collargol silver powder. Details are included as Appendix C.2: Colloidal Silver Solution Mixing Procedures.

Potters for Peace recommendations were followed to then create the "application solution" dilution. For the application solution, 2 mL of the 3.2 percent stock solution was mixed with 250 mL of Millipore ultrapure water, yielding a colloidal silver solution of 0.018 percent by weight, since only 70 percent of the Collargol silver powder is silver. Details of this mixture procedure are included in Appendix C.2: Colloidal Silver Solution Mixing Procedures.

Some of the analytic measurements presented herein were performed on a colloidal silver solution of 5 mg/L (nominal); these runs are specifically noted in the Results section for each particular measurement. The 5 mg/L was prepared by adding 79 µL of the stock 3.2 percent solution to 500 mL of ultrapure water. Note that this solution was nominally 5 mg/L; actual silver concentration was 3.5 mg/L for this solution.

Ceramic Characterization

Scanning Electron Microscopy (SEM)

New SEM images of two different filters were captured recently. One of the filters was fabricated in Managua, Nicaragua, used for 2-3 years by a household in Nicaragua, and then used by the University of Colorado, Boulder for testing over the course of 3-4 more years. The other filter was unused, fabricated in Lima, Peru, and donated by Mercantil Interamericana, SAC for further research.

A LEO Model 1525 scanning electron microscope was used to capture micrographs of the ceramic microstructure of pot filters. Images were recorded using a secondary electron detector, an in-lens electron detector, and a backscatter electron detector to view physical and compositional information.

Silver Characterization

Inductively Coupled Plasma with Mass Spectroscopy (ICP-MS)

ICP-MS was employed to determine the composition of the application solution. The application solution was mixed as described above, then diluted with ultrapure water in order to contain appropriate concentrations of silver for the ICP-MS device (generally less than 500 ppb). The scan was run across a range of elements in order to determine trace contaminants, as well as actual silver content. This analytical technique is not capable of resolving hydrogen, carbon, nitrogen, oxygen, fluoride, or any of the noble gases. This has some effect in this study as the Collargol colloidal silver solution contains a substantial quantity of casein ($C_{47}H_{48}N_3O_7S_2Na$).

High Speed Centrifugation

The nominal 5 mg/L silver solution was centrifuged at 42,000 rpm (288,000 g's) in order to separate the silver particles, allowing for a direct measure of silver ions in solution. Appendix C.3: High Speed Centrifugation shows more detail of calculations and theory related to the centrifugation required to remove particles from suspension.

Two 10 mL specimens of the nominal 5 mg/L silver solution were centrifuged, one for 1 hour and one for 2 hours. The supernatant was carefully removed by pipette in order to avoid transfer of the pelletized nanoparticles and stored in a separate centrifuge tube for analysis. ICP-MS was used to determine silver content of the supernatant, as well as an uncentrifuged control sample. Analysis was conducted at the Laboratory for Environmental and Geological Studies (LEGS) at the University of Colorado. Silver detection limit for this ICP-MS analysis was 11 ppb.

The measured silver concentration of the centrifuged sample relates to the ionic fraction of the silver solution. The colloidal fraction was calculated as the difference between the total silver content and the ionic silver content.

Transmission Electron Microscopy (TEM)

A 10 µL drop of the application solution was applied to a standard 300 mesh copper TEM grid for imaging. A JEOL 2000FX transmission electron microscope with LaB_6 filament was used to image the silver nanoparticles at 200 kV using a 1k by 1k CCD camera, in accordance with best practice electron microscopy techniques.

Particle Size Distribution (PSD)

The particle size distribution (PSD) was determined by use of a Zetasizer Nano device (Malvern Instruments) by means of dynamic light scattering (DLS). The nominal 5 mg/L silver solution was prepared as described above, with the stock 3.2 percent solution added to pH adjusted Millipore ultrapure water. The water was adjusted using a similar technique as employed for the sample water preparation: pH adjustment was achieved through addition of 1 M nitric acid or 1 M sodium hydroxide.

Measurements were taken at a range of relevant pH values, from 3 to 10. Measurements were repeated five times at each pH value of interest. Data was recorded using the Malvern Zetasizer software package.

Zeta Potential

Zeta potential was recorded in conjunction with PSD data using the Malvern Instruments Zetasizer Nano. The exact same samples were used for this data collection. Measurements were taken across the same range of pH values, from 3-10, and again repeated five times at each pH value of interest.

QCM Measurements

Most QCM measurements were obtained using commercially available QSX-303 quartz sensors, from Q-sense (product details included in Appendix C.4: QSX-303 Sensor Specifications). These sensors are AT-cut quartz sensors 14 mm diameter and 0.3 mm thick. The fundamental resonance frequency is 4.95 MHz (± .05 MHz) with an electrode surface area of 0.24 cm^2. The gold electrode has a thickness on the order of 100 nm. The QSX-303 quartz sensors were selected because of the silicon dioxide, or silica, coating that is sputtered onto the working surface of the sensor, on top of the gold electrode. The thickness of that silica coating is 50 nm.

As discussed in the Background section of this document, each individual sensor has its own fundamental frequency. Deviations from that nominal value are caused by slight changes in the cut or thickness of the sensor, as well as slight changes in the placement location of the sensor within the holder. By following the procedures outlined here, and acquiring baseline data for each individual sensor, subsequent measurements on each sensor will be repeatable and comparable among that sensor's specific data set.

Initial QCM Experiments

Some initial experiments were conducted using a slightly different experimental setup, but with comparable procedures. Those experiments are noted when presented. In those cases, the sensor surface was unmodified, so the active area was the gold electrode itself. The sensors were of a slightly different geometry (25.4 mm diameter with 0.4 cm^2 active area), but had a similar nominal fundamental resonant frequency of 5 MHz.

Sensor Handling

All handling of the sensors, from initial receipt through all cleaning processes and experiments, was conducted with latex gloves. The primary means of holding or transferring each sensor was through the use of a square tip, flat bladed tweezer. The sensors were always clasped near the edge, away from the electrodes. These handling efforts were to minimize contamination of the sensor, and to reduce the chance of scratching the sensitive electrodes and coatings, in order to minimize sources of error in the resonant frequency data collection.

Sensor Cleaning

Each sensor was cleaned within 24 hours prior to the baseline measurement, and again within 24 hours prior to silver deposition. The cleaning procedure, as recommended by the manufacturer, involved a number of steps to remove contaminants from the surface of the sensor (see Appendix C.5: QCM Sensor Cleaning Procedures for more detail). Initially, each sensor was subjected to the BioForce Nanosciences ProCleaner UV/ozone device for 12-15 minutes. Next, a 30-60 minute soak in a 2 percent solution of Sodium Dodecyl Sulfate (SDS) continued to break chemical bonds of contaminants to the surface. Each sensor was then rinsed with ultrapure water three times per side and dried with dry nitrogen. After a final 12-15 minute cycle in the UV/ozone cleaner, the sensor was considered ready for use.

General QCM Procedures

All data from these experiments, aside from the preliminary experiments briefly mentioned, was recorded using a Q-sense E4 QCM device with frequency and dissipation monitoring of seven harmonics: the first, or fundamental, resonant frequency, along with the 3rd, 5th, 7th, 9th, 11th, and 13th harmonics. The E4 device has four sensor holders that can be monitored simultaneously, which has a number of advantages including overall throughput and replications of the same experimental conditions. That simultaneous replication is especially helpful to ensure identical influent conditions during flow testing. All manufacturers recommended procedures were followed during set-up and experimentation.

QCM Device

Initial QCM experiments, as presented in the Preliminary Results section, were conducted on a Stanford Research Systems QCM200 device. This digital controller drives each sensor at its resonant frequency, recording not only the frequency, but also the electrical resistance. This device is only capable of monitoring the first, or fundamental, resonant frequency.

The majority of the results presented were collected on a Q-sense E4 QCM device. The sensor holders for the E4 are shown in Figure 6. Some of the features of these holders include precise temperature control, repeatable sensor placement, repeatable clamping force, and an incorporated flow cell that readily allows for flow experiments. All experiments were run at 22.0 ± 0.1 °C, unless otherwise noted. The Peltier system within the sensor holder did an excellent job of maintaining that temperature during both dry and flow measurements. Every sensor from Q-sense has one flattened side where the flat surface is parallel to the piezoelectric axis of the AT-cut quartz. The gold electrodes are deposited in relation to that notch to ensure that each sensor is oriented correctly when in the holder.

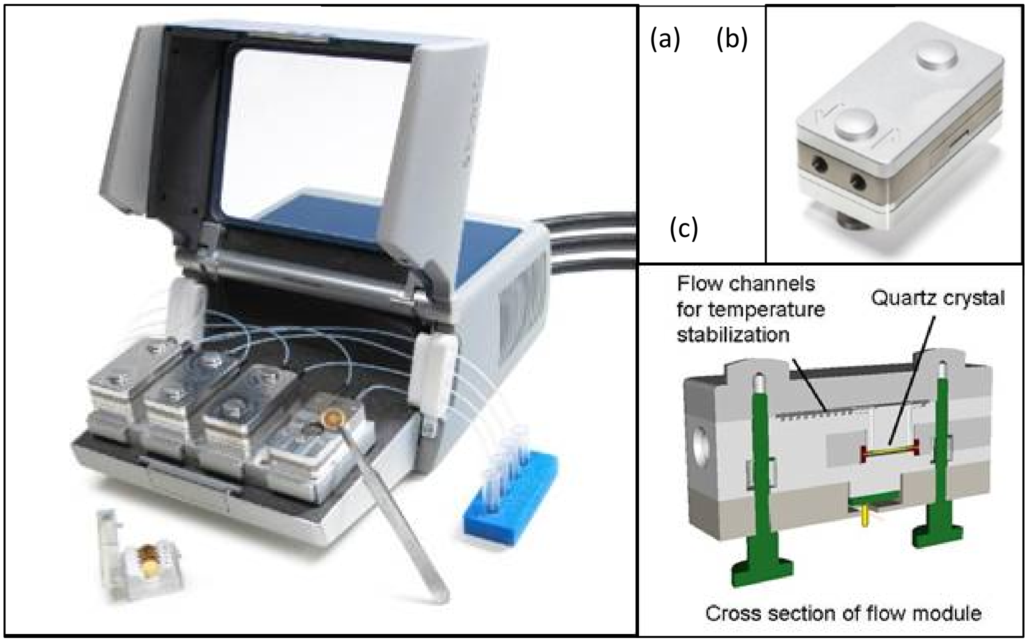

Figure 6: Q-sense E4 QCM device shown (a) along with an individual sensor holder (b) and a cross-sectional schematic (c) of the holder with incorporated flow paths. (Q-sense product literature)

The top of the E4 sensor holder is billet aluminum with two threaded screws to secure it in place. As the screws are tightened, the flat mating surfaces of the metal top will buffer the height adjustment, providing a similar clamping pressure to the quartz sensor itself. Actual contact is made to the sensor through a Viton o-ring on each surface of the sensor. These o-rings keep the fluid in place over the sensor during flow experiments. An inlet tube leads from the bulk influent fluid to the inlet of the sensor holder. The fluid than snakes through a path associated with the Peltier thermal system so that not only is the sensor held at a constant 22.0 degrees Celsius, but the fluid entering the chamber will also be steady at that temperature. There is an outlet from the sensor holder which then leads to a waste container.

Data Collection and Initial Assessment

Data was collected through the Q-sense software package, which recorded 7 harmonic frequencies (odd harmonics from first through thirteenth), along with the dissipation of each of those 7 harmonics, for each of the 4 sensors being run simultaneously. A data set, including the frequency and dissipation values for all 7 harmonics, was taken from each sensor approximately every 5 seconds. Time and temperature data was stamped alongside each data set collected. The data was exported into Excel for statistical analysis.

Initially, when all four sensors were loaded into the Q-sense E4, the device found each resonant frequency and associated dissipation. The device scanned a range of 495 kHz, centered on the nominal resonant frequency for each harmonic of interest, with a step of 2.5 kHz between each successive data point. When driving the quartz sensor at each of those steps, the amplitude of the piezoelectric oscillation was monitored. The frequency causing the maximum amplitude of oscillation was the resonant frequency for that sensor, in line with resonant theory.

During this initial resonant frequency search, if the device was unable to find any particular harmonic’s maximum oscillation, or if there were multiple peaks within the scanning range, the data from that harmonic was determined to be unsuitable for further analysis; in some cases the data was still collected but not used for analysis, in other cases the data from that harmonic was not collected during the experiment. When the QCM device was unable to locate the resonant frequency, the rejection criteria was trivial. At other times, the Q-sense E4 would return a value for the resonant frequency and dissipation, but there were multiple peaks within the scanning range. Whenever at least one of the secondary peaks exceeded 50 percent of the amplitude of the primary peak (associated with the frequency value returned by the E4), the data from that harmonic was deemed unsuitable for further analysis.

The first harmonic was not used during analysis as it can be skewed by its relatively deep penetration into the specimen, often much longer of a distance than the thickness of an attached film.

This is common practice in the literature and a manufacturer recommendation (Quevedo and Tufenkji 2009; Poitras et al. 2009).

Based on the criteria explained above, the data presented in this paper will not include the 11th or 13th harmonic. In very few cases did that data pass the initial assessment. There was insufficient data from these higher harmonics to group for trends.

Data presented here will focus on the odd harmonics from 3 through 9 (i.e., 3rd, 5th, 7th, and 9th).

Experimental Flow Overview

A flow chart is shown as Figure 7 which outlines the procedures followed for each sensor throughout the set of experiments presented here. More detail of each step may be found below.

Baseline Dry Measurement

Each sensor was placed into the Q-sense E4 specimen holder following the orientation guidelines. Initial resonant frequencies were determined for each sensor, each harmonic, which were used to determine the validity of the data collected, as explained above.

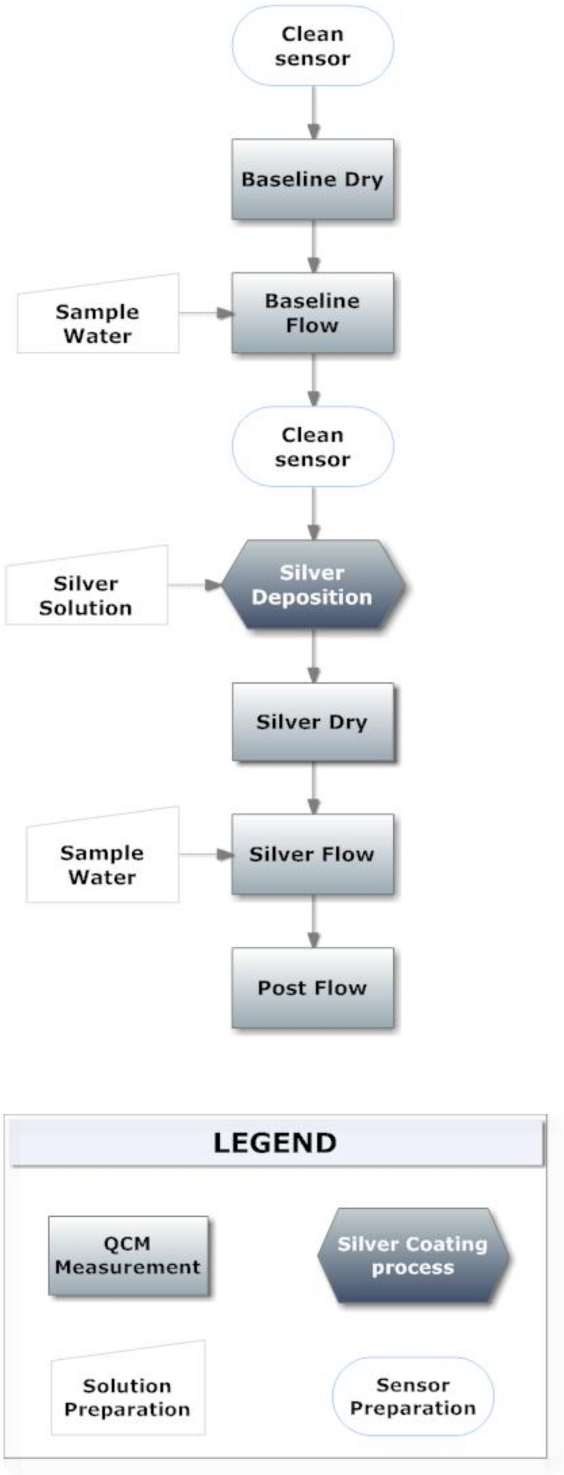

Figure 7: Flow chart of experimental procedures for all QCM measurements

Data collection was carried out for a minimum of 10 minutes, seeking a stable baseline measurement. During that time, if any of the sensor's frequency readings drifted by more than 2 Hz, the measurement was started over. This was done in accordance with the manufacturer's recommendation and supported by literature (Cho et al. 2010). It is presumed that substantial frequency drift is a measure of changing residual effects from clamping forces or from temperature equilibration, unless another effect might explain the change, which is an unlikely case for these baseline measurements. The stable baseline measurement was sought to ensure that the reading most accurately captures the fundamental resonance frequencies of each individual sensor.

Further data analysis was conducted by using the initial resonant frequencies captured during the initial sweep. This is appropriate due to the stable measurement criteria explained above. Also, this approach will provide a better comparison to QCM measurements taken with an impedance analyzer, or other circuit scanning electronics, in that those measurements are instantaneous, so do not have a comparable time scale as the E4 QCM.

Baseline Flow Measurement

For each experimental condition, a baseline flow measurement was recorded to capture each sensor's response to that fluid being in contact with the sensor surface. The four sensors were located in the sensor holder following the orientation guidelines mentioned above. Tubing was arranged to run the four sensors in parallel, using the exact same influent source for the four sensors involved in that experiment.

The baseline flow measurement was conducted using the same influent waters that were used during the correlated experimental flow (details to follow). In all flow runs, the flow rate was controlled by an Ismatec IPC-N4 peristaltic pump at a constant 100 µL/min through each sensor's holder.

Initially, the resonant frequency of each sensor was captured when dry. Within a minute or two, flow of the influent water began. During this measurement, the shift in frequency and dissipation from the dry baseline can be detected in real time.

Given the geometry of the flow path immediately above the sensor, there is a range of linear velocities across the active area of each sensor. That range may be bounded by the inlet velocity as governed by the flow channels embedded in the sensor holder (maximum linear velocity) and the velocity at the widest section of the sensor (minimum linear velocity). According to Q-sense product literature, the flow channel within the sensor holder is 1 mm by 0.6 mm and the diameter of the volume contained within the o-rings is 11 mm. At the volumetric flow rate of 100 µL/min, those dimensions provide a linear velocity range of 0.23 to 0.28 cm/sec. Using a characteristic dimension of 11 mm, the flow is definitely laminar, with a Reynold's number of around 0.25.

The extremely complex geometry of the porous structure of ceramic pot filters prohibits a direct calculation of the linear velocity of water passing through the filter. A rough approximation may be found using the reported values for residence time, tortuosity, and wall thickness, which are approximately 40 min, 5-10, and 1.5 cm, respectively (van Halem 2006). Given those parameters, a linear velocity of around 0.003 to 0.006 cm/sec is expected for water passing through the walls of the filter. Using a characteristic dimension of 15 µm, based on the mean pore diameters published by van Halem, the Reynold's number for this flow regime is around 5×10^{-4}.

Based on those flow rate comparisons, the QCM experiments are greatly accelerated compared to the flow rates actually seen in ceramic filters. This is a benefit to receive a greater amount of information in shorter time, but could substantially lower the microbial efficacy relative to the full filters, given a much shorter contact time between the silver nanoparticles and the microbes. For chemical and physical effects, however, the accelerated testing is quite useful.

Looking at the linear velocities calculated above, the QCM measurements are being conducted at a rate about 40 to 75 times faster than the flows through actual filters. Volumetrically, the difference is even greater. For instance, a rough model of the pore structure as a pipe with a diameter of 15 µm yields a volumetric flow rate of 1.7×10^{-3} µL/min, meaning that the QCM flow rate is nearly 80,000 times that of the actual filter. That extreme difference in flow rates may actually be a benefit when monitoring changes at the surface that involve chemical interactions and dispersions within the bulk fluid. In that case, the fluid will have sufficient ability to absorb the particle of interest without approaching saturation. Also, since the linear velocity is comparable, physical removal of the adsorbed nanoparticles should be similar in both cases.

In a few cases, flow to a certain sensor was interrupted due to tubing or pump failures. Every effort was made to bring the flow on-line for each sensor during the baseline flow run, but in some cases, data was collected from only three sensors. The number of sensors included in the data analysis is noted where presented within this document.

Once flow was initially detected across each sensor, the frequency and dissipation for each sensor was monitored for at least 10 minutes to ensure stability. Frequency drifts of more than 2 Hz during that 10 minute interval were not seen during baseline flow measurements, so no data sets were eliminated or repeated due to frequency drift.

Silver Deposition

After the sensor was cleaned according to the procedures detailed above, colloidal silver was then deposited onto the silica surface of the sensor. Each sensor had 5 µL of the application solution (prepared as described above by adding colloidal silver to Millipore ultrapure water) drop cast onto the center of the electrode area, equating to an expected deposited mass (including both casein and silver) of 1.27 µg.

As presented in the Results section, and corroborated by the manufacturer's specifications, measured silver concentrations of the application solution were a portion of the mass added to the silver solutions. Per mixing guidelines, the Collargol (silver and casein) concentration of the application solution should be 250 mg/L. Two different application solutions were tested by ICP-MS, returning silver concentrations of 178 and 190 ppm, a shortfall of around 30 percent. This matches exactly with the range of silver content given by Laboratorios Argenol of 70-75 percent by mass. Therefore, the deposited mass on each sensor is approximately 0.87 µg. Discussion from here on will presume that the silver deposited onto each sensor was 870 ng.

Drop casting the application solution onto the sensor was deemed to be the most feasible manner in which to deposit the silver that was, most importantly, representative of the adsorption mechanism of the colloidal silver when applied to ceramic pot filters. Each sensor then had an areal mass of deposited silver of 3600 ng/cm^2, or 3.6 µg/cm^2.

For comparison, a ceramic pot filter has a surface area on the order of 1500 cm^2 to which 45 mg of colloidal silver is applied; that equates to an areal silver concentration of around 30 µg/cm^2, neglecting wall thickness, porosity, or other dimensional effects. To obtain a comparable areal mass of deposited silver on the QCM sensors, around 7 µg of silver would have been required.

Attempting to account for the ceramic pore structure of the ceramic filter changes the silver mass loading dramatically. A simple model of a homogeneous pore structure, with each pore at a representative diameter of 15 µm, shows that 3×10^8 pores would be required to provide 35 percent porosity to a filter with overall surface area of 1500 cm^2. Including the surface area of those pores into the total surface area of the three-dimensional filter (thickness estimated at 1.5 cm) then increases the surface area to 210 m^2, over 3 orders of magnitude greater than the surface area solely considering the bulk surface. Applying 45 mg to 210 m^2 yields an average areal mass loading of 21 ng of silver per square centimeter. Given a sensor working area of 0.24 cm^2, that equates to a deposition of 5 ng of silver onto a QCM sensor to be comparable to the full filter mass loading.

That amount of silver would have been extremely difficult to reliably adsorb, and would have pushed the resolution limits of the QCM device itself. By applying the 5 µL drop of the application solution, these potential issues were mitigated by providing sufficient mass to detect initially, as well as to detect changes in that mass.

Each sensor was placed onto the cleaned surface of a hot plate, maintained between 65 and 75 degrees Celsius as recorded by an affixed thermocouple. The sensors were allowed to equilibrate to around 70 degrees Celsius by resting on the hot plate for 30-60 minutes before drop casting the silver solution.

A 5 µL mechanical pipette (uncalibrated; expected accuracy within 10 percent) was used to drop cast the application solution onto the silica surface of the sensor. After drawing the application solution into the pipette tip, it was imperative to wipe down the external surface of the tip with a clean laboratory wipe so as not to drop more solution than expected onto the sensor. When cleaning the outside of the pipette tip, the wipe itself was not placed near the outlet of the pipette tip, for if it was, some of the application solution may have been absorbed into the wipe through capillary action. In that case, the contents of the pipette tip were safely discarded and the pipette was refilled with 5 µL of application solution to proceed.

The outlet of the pipette tip was carefully held centered 1-3 mm above the surface of the sensor. A fraction of the application solution was released into a droplet. When the majority of the water had been driven from that droplet, another small fraction of the application solution was released onto the same location as the original droplet. When the majority of the water had been driven from that droplet, this procedure was repeated one or two more times until all of the 5 µL of application solution had been cast onto the sensor. Each sensor remained on the hot plate at 65 to 75 degrees Celsius for 30-60 minutes in order to drive off any residual water.

All sensors were stored in their original protective cases. Silver measurements were taken with the QCM within 24 hours of this deposition process.

A secondary deposition technique was used for some of the Preliminary results presented in this document. Sputtering is a technique that physically deposits particles of the target material (in this case, silver) onto the specimen by bombarding the target with an ion beam (Madou 1997). Sputter coating is often used for specimen preparation in electron microscopy, as well as other thin-film deposition processes. A solid silver target of 4N purity (> 99.99 percent silver content) was used for all sputtered films. A Gatan Model 682 Precision Etching and Coating System (PECS) with incorporated thickness monitor (Model 681.20000) was used to coat the gold electrode surface area of the QCM sensors. The outer perimeter of quartz itself (outside the area of the electrode) was masked to minimize any electrical effects of adding a conducting layer of silver to the surface. Measurements were taken with calipers to ensure that the entire surface area of the working electrode was covered by the silver film.

Silver Dry Measurement

The procedure for the Silver dry measurement was identical to that followed for the Baseline measurement, with an exception for an increased tolerance for frequency drift. The measurement was re-initiated if drift exceeded 4 Hz in 10 minutes; however in most cases the resonant frequencies were stable within 2 Hz over 10 minutes.

Similarly, data analysis was conducted using the initial resonant frequencies, as described for the Baseline dry methods above.

Silver Flow Measurement

Once the specified influent water was prepared, the silver flow experiment was conducted to detect rate of release of silver nanoparticles from the silica surface of the QCM sensors.

The procedures for the silver flow experiment were identical to that of the baseline flow runs, with a constant 22.0 degree Celsius temperature and steady 100 µL/min flow rate. The data collection was similarly started with the sensors in E4 QCM holders at ambient conditions, with flow beginning one to two minutes after commencing data collection.

The shift in frequency and dissipation were evident in real-time as the leading edge of the flow filled the volume above the sensor surface. Data was recorded during this initial onset of flow, and continued to record for 30 minutes to 3 hours after the flow was first detected on the sensor.

At the end of the flow run, data collection was stopped before the inlet tubing was removed from the influent water (while the pump continued to operate). Once flow through the tubing had ceased, the sensors were removed from the holders and placed vertically in their original storage containers. At this time, a set of dummy sensors were placed into the E4 sensor holders in order to clean the tubing and flow cells without risk of damaging the electronics. The cleaning process involved flowing the following fluids in sequence for at least 5 minutes each: bleach, ultrapure water, SDS, ultrapure water, and then ethanol.

The sensors involved in the silver flow experiment were stored at room temperature for 24 to 72 hours before proceeding with post flow measurements.

Post Flow Measurement

Final QCM measurements were taken of each sensor once dry, in order to compare the final shifts of frequency and dissipation relative to baseline dry measurements, both taken under ambient conditions.

The procedures for the post flow measurements were similar to those of both the baseline and silver dry measurements. Again in this case, the tolerance for frequency drift was loosened to less than 4 Hz in 10 minutes, allowing for the greater instabilities seen in the measurements after the sensors were exposed to the flow experiment.

Similarly, data analysis was conducted using the initial resonant frequencies, as described for the Baseline dry methods above.

At this time, each sensor was imaged using optical microscopy in order to gain visual perspective on the quantity and form of any silver left on the surface of the sensor. Images were captured using a Signatone 1160 series probe station at 5x magnification and are included as Appendix D.5: Optical Micrographs of Post Flow Condition.

Sample Water Preparation

Table 5 below shows the sample waters used during these experiments. More details of their preparation and characterization follow. The baseline condition, Millipore ultrapure water, is the first line of Table 5. The ionic strength and chloride content of each sample water is provided, with more discussion to follow in the Results and Discussion section.

Table 5: Sample water summary table

Sample water	**pH** (pH units)	**Ionic Strength** (mM)	**Cl^- concentration** (mM)
Millipore ultrapure	5.8	8.8 E-04	0
51 NTU, Kaolin particles	5.6	8.8 E-04	0
HNO_3 at pH=4.8	4.8	5.0 E-03	0
NaOH at pH=9.3	9.3	0.015	0
$NaNO_3$	5.4	150	0
$Ca(NO_3)_2$	5.7	150	0
NaOCl at 8.8 mg/L	8.5	0.12	0.12
NaOCl at 525 mg/L	8.5	7.0	7.0
1% PBS	7.1	1.6	1.4
10% TSB at 1.2 g/L TOC	7.0	129	8.6
NOM at 15 mg/L TOC	7.1	0.9	-

Baseline Water

The baseline condition to which all results were compared was that of Millipore ultrapure type 1 water obtained from a Direct-Q/UV 3™ system. Boulder county tap water was fed into the Direct-Q system, where it was treated sequentially by reverse osmosis, a dual wavelength (185 and 254 nm) UV-lamp, and then a mixed-bed ion exchange resin along with an Organex stage for final removal of trace ionic and organic contaminants. The effluent water from the Millipore system had a specific conductivity of 18.2 MΩ-cm, pH between 5.5 and 6.0, and less than 5 ppb of total organic carbon (TOC).

In all cases, the pH of the charge water was tested using a model IQ140 pH meter that was calibrated using a two-point calibration at pH values of 4.1 and 7.0 or at pH values of 7.0 and 9.0, depending on the sample water, immediately before use. The QCM flow experiment, whether a baseline flow or silver flow run, was begun within 1 hour of recording the pH data.

pH Adjusted Water

A range of pH values was selected to bound the anticipated pH values of water being poured through a ceramic pot filter by the end-user. The baseline ultrapure water was run at a pH of 5.8, which is within the range of interest. Other data points were taken at pH values of around 5, 7, and 9, with the charge water prepared according to the following procedures.

pH = 5 water

Nitric acid (HNO_3, Fisher Scientific) was added to the ultrapure water in order to reduce the pH. A previously prepared 1 M solution of nitric acid was added using a mechanical pipette for controllable additions at small volumes (less than 0.1 mL each addition). The charge water reached a measured pH of 4.8.

Since this water was not buffered against pH changes in order to minimize the variables of each charge water, the pH 4.8 sample waters for the baseline and experimental measurements were prepared at different times.

pH = 7 water

Sodium hydroxide (NaOH, Fisher Scientific) was added to the ultrapure water in order to raise the pH. The procedure followed was similar to that described above for the pH = 5 water. The charge water reached a measured pH of 6.8.

pH = 9 water

Sodium hydroxide (NaOH, Fisher Scientific) was added to the ultrapure water in order to raise the pH. The procedure followed was similar to that described above for the pH = 7 water, with a substantial increase in the quantity of NaOH added to solution. The charge water reached a measured pH of 9.3.

Turbid Water

Kaolin powder (Fisher Scientific) was added to the baseline ultrapure water in order to increase the turbidity to a nominal value of 50 nepholometric turbidity units (NTU). Turbidity measurements were taken on a Hach Ratio/XR Turbidimeter, using a calibration curve obtained less than 30 days prior to these measurements from control specimens prepared by diluting a 4000 NTU StablCal® Formazin turbidity standard.

Kaolin powder was added in increments with turbidity measurements taken in clean glass vials after each addition. Charge waters were prepared to 51.5 NTU.

Ionic Strength Controlled Water

In order to determine the effects of ionic strength on the rate of release, yet remain at relevant ionic strengths to natural waters, sample waters were prepared to an ionic strength of 150 mM. Nitric salts were used for their low propensity for chemical interaction with silver.

Monovalent ion

Sodium nitrate ($NaNO_3$, Fisher Scientific) was selected as a representative monovalent ion. A mass of 12.75 g of sodium nitrate was added to one liter of Millipore water. The mixture was then placed onto a stir plate for 15-20 minutes. The pH of this sample water was 5.4, measured both at the time of the baseline flow and the silver flow experiments.

Divalent ion

Calcium nitrate ($Ca(NO_3)_2$, Fisher Scientific) was selected as a representative divalent ion. Sample water preparation for this water was similar to that described above for the monovalent ion. To one liter of Millipore water, 23.62 g of calcium nitrate was added. The pH of this sample water was 5.7, again measured both during baseline flow and silver flow experiments.

Natural Organic Matter (NOM) in Water

Natural lake waters were collected from Big Elk Meadow Lake, Colorado on June 22, 2010. After collection, the water was filtered in order to concentrate the NOM. Total organic carbon (TOC) was measured to be 15.7 mg/L. Ionic strength was determined to be 0.93 mM based on the specific conductivity of 58 µS. Alkalinity was found to be 28-30 mg/L. The water was refrigerated until immediately before experimentation. The pH was measured to be 7.1 before both baseline and silver flow experiments.

Sodium Hypochlorite in Water

Two concentrations of sodium hypochlorite were prepared as sample waters: one to represent a disinfecting cleaning solution of 1 percent dilution (by volume) of typical household bleach and the other to represent bleach-treated drinking water. In both cases, standard household bleach at 5.25 percent sodium hypochlorite (NaOCl) was used.

The 1 percent dilution solution has a calculated ionic strength of 7.1 mM and a measured pH of 8.5. The calculated concentration of sodium hypochlorite was 535 mg/L for this solution.

The water prepared to represent bleach-treated drinking water was based on the United States Environmental Protection Agency (USEPA) and World Health Organization (WHO) recommendations for treating drinking water with bleach containing sodium hypochlorite (USEPA 2006; WHO 2003). In both of those sources, the recommended treatment is 165 µL (~3 drops) of bleach per liter of water. The resulting solution has a calculated ionic strength of 0.12 mM, a measured pH of 8.5 and a sodium hypochlorite concentration of 8.8 mg/L.

Preliminary results presented here also show data that was obtained using a dilution of household bleach that was not prepared according to any set procedures, but rather was mixed roughly at a 20 percent dilution (by volume). Expected sodium hypochlorite concentration for this cleaning solution is around 10.5 g/L.

Results and Discussion

Provided in this section are the results obtained during this investigation, along with a discussion of the implications. Initially, characterization data of the colloidal silver used during ceramic pot filter production is shown. Results from a few preliminary QCM experiments are shown next, to provide context for the direction of this investigation. Finally, results from the experimental matrix defined above are presented and discussed.

Ceramic Characterization

The SEM images below are labeled to identify which filter the specimen was taken from, as well as to identify the location within the filter. Shown in Figure 8 is a cross-sectional schematic of the ceramic pot filter, with a zoomed view of a side wall of the filer. As shown, any specimen taken from the surface of the filter that would generally be in contact with the water contained within the filter volume is referred to as an "inner wall" specimen. "Outer wall" specimens originate from the convex surface from which the filtered water will exit to the reservoir. And "mid-wall" specimens were taken from a point at approximately half of the wall thickness.

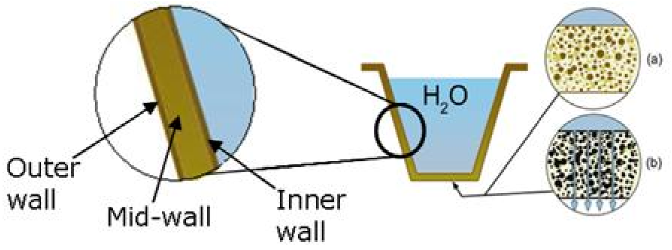

Figure 8: Cross-section schematic of a ceramic pot filter (McAllister 2005)

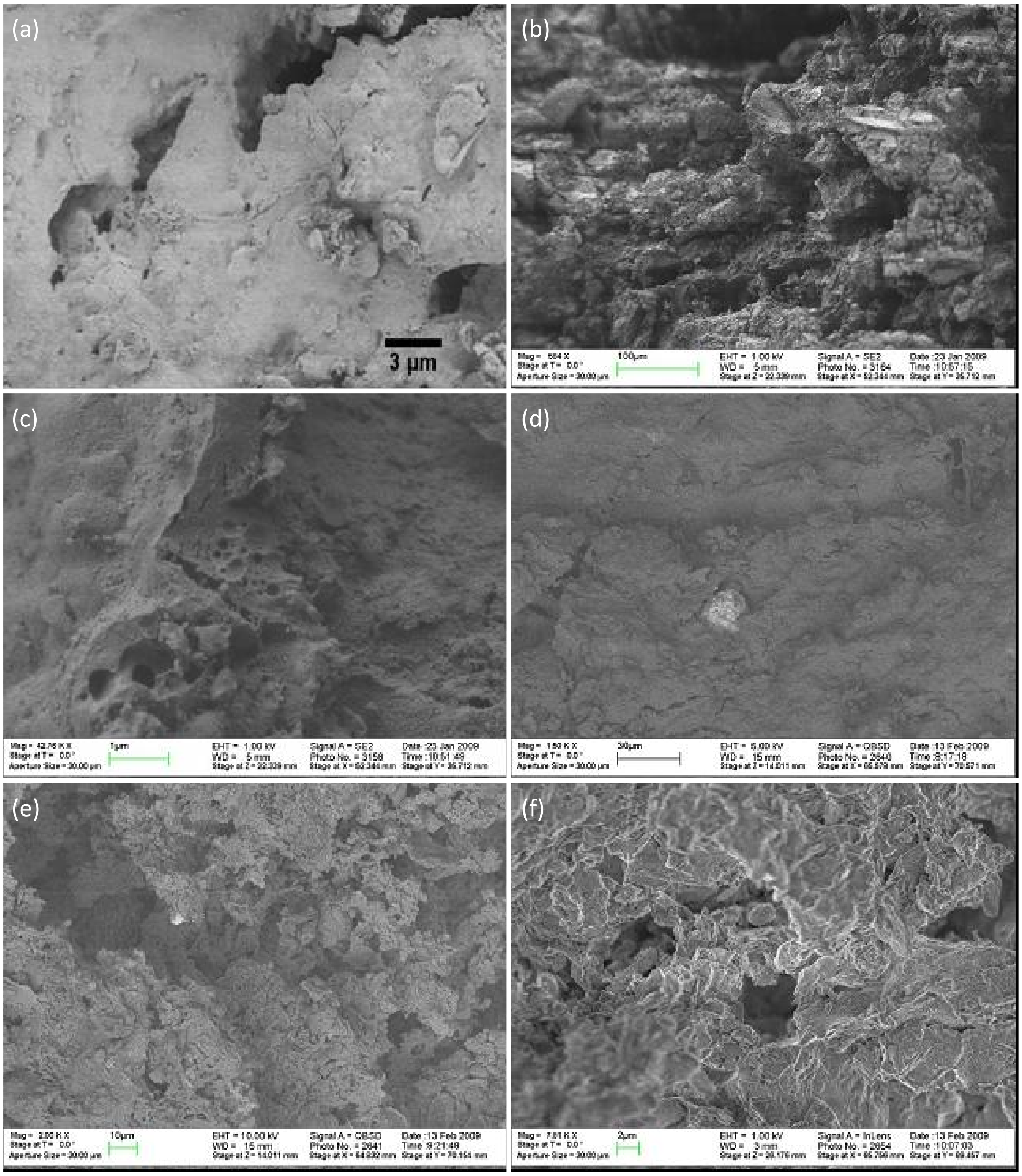

Figure 9: SEM images of inner wall of used Nicaraguan filter by Secondary Electron Detector (a); mid-wall of used Nicaraguan filter by Secondary Electron Detector (b, c); outer wall of used Nicaraguan filter by Backscatter Electron Detector (d, e); mid-wall of new Peruvian filter by In-Lens Detector (f). Scale bars shown represent: (a) 3 µm, (b) 100 µm, (c) 1 µm, (d) 30 µm, (e) 10 µm and (f) 2 µm.

It is apparent from these micrographs that years of use has a dramatic effect on the surface topology. Note the washed out appearance of the filter produced in Nicaragua, in contrast to the more distinctive features of the newly fabricated filter from Peru. The images taken with the backscatter detector (Figure 9: d, e, and f) show the layered morphology of the ceramic matrix, along with some random inclusions of contaminant elements that were likely mixed in with the starting materials.

See Appendix A: SEM Images for a more thorough compilation of SEM images taken from these same specimens.

Silver Characterization

Manufacturer Specifications

The colloidal silver product used throughout this study was produced by Laboratorios Argenol of Spain under the name Collargol, a powdered form of silver nanoparticles. The silver nanoparticles were provided mixed with casein ($C_{47}H_{48}N_3O_7S_2Na$), a dairy milk-derived protein, to aid in their suspension. According to the manufacturer specifications, the mixture contains 70-75 percent silver by weight, leaving approximately 30 percent casein content by weight. Actual manufacturer specifications and manufacturer provided TEM analysis of their product are included in Appendix C.1: Silver Collargol Data.

Transmission Electron Microscopy (TEM)

Micrographs of the silver nanoparticle were captured using a TEM. Figure 10 shows representative images taken during TEM analysis. As can be seen, the silver nanoparticles are quite spherical, with diameters on the order of 10 to 30 nm. This imaging was used as an initial approach to verify approximate particle size and was not sufficiently thorough to report details of particle size distribution.

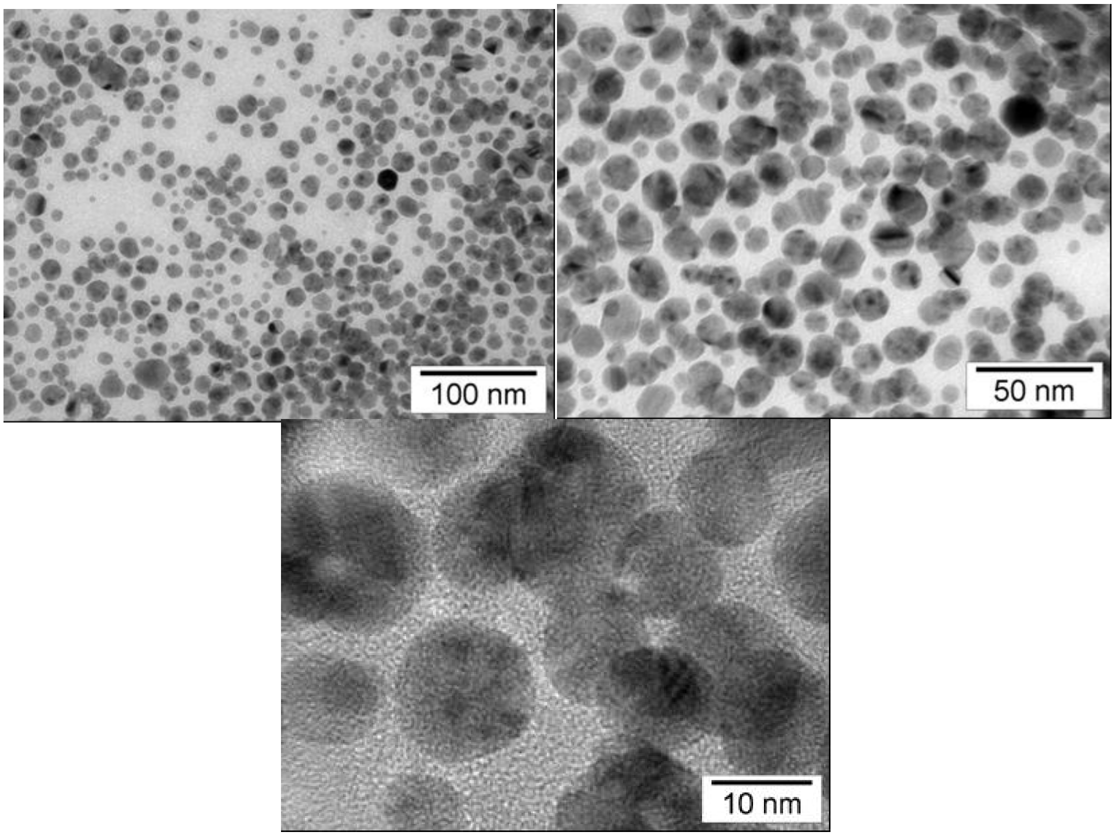

Figure 10: TEM images of Collargol colloidal silver at various magnifications

Particle Size Distribution

Particle size distribution (PSD) was determined by dynamic light scattering analysis conducted on the 5 mg/L aqueous solution of silver nanoparticles in ultrapure water. Particle size distributions, as shown in Figure 11, were calculated by two methods: intensity and number. Each measurement was repeated 5 times, with 95 percent confidence interval shown as the error bars. In most cases across the relevant pH values, the data point marker is larger than the error bars, but the zoomed in plot (inset, Figure 11) shows this region in greater detail.

The intensity distribution is greatly affected by larger particle sizes, as a one order of magnitude increase of hydrodynamic diameter effects a million-fold increase in the intensity peak. The number distribution accounts for that substantial affect on the light intensity, resulting in a peak that is proportionally sized to the count of particles at any given diameter. For that reason, the intensity distribution shows an average hydrodynamic diameter larger than that of the number distribution across the range of pH values studied.

The most obvious feature of these data is that below a pH of around 4, the hydrodynamic diameter of the silver nanoparticles increases to particle sizes greater than 1 µm. The agglomeration taking place in that lower pH range would cause instability of the colloidal solution, precipitating out silver particles. After the PSD analysis, silver precipitate was present in the vial containing the pH = 3.5 solution, confirming the behavior expected based on the PSD results.

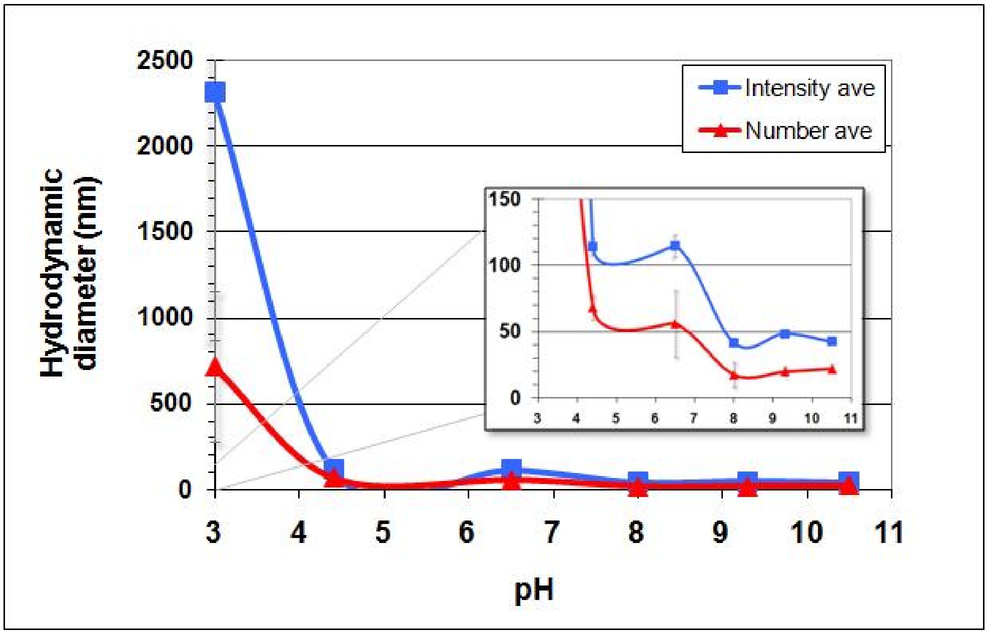

Figure 11: Particle size distribution of Collargol colloidal silver solution in Millipore ultrapure water. Inset plot is the same data zoomed in to a smaller range of hydrodynamic diameters. pH adjustment accomplished with HNO_3 or NaOH.

Another important feature is the excellent correlation of these PSD data to the TEM images provided above. Across a pH range representative of water used in the field for silver solution preparation, the number distribution PSD data suggests a mean particle diameter of 20 to 55 nm.

Zeta Potential

Zeta potential measurements were also conducted across a range of pH values, from 3 to 9.5. The results from this analysis are provided as Figure 12. These measurements demonstrate that the isoelectric point is approximately 3.5 for these silver nanoparticles.

Across the range of pH values of interest (for production setting silver solution preparation), the colloidal particles are well stabilized at zeta potential values of around -45 millivolts (mV). When the pH drops below 4, the particles rapidly become unstable as zeta potential values approach zero, or pass through the isoelectric point to low positive values.

These zeta potential results match closely with the analytical and visual data obtained from the particle size distribution measurements. The agglomeration into large particles at low pH values detected during PSD analysis is accelerated as the near-zero zeta potential values suggest a minimal repulsive force between the like particles.

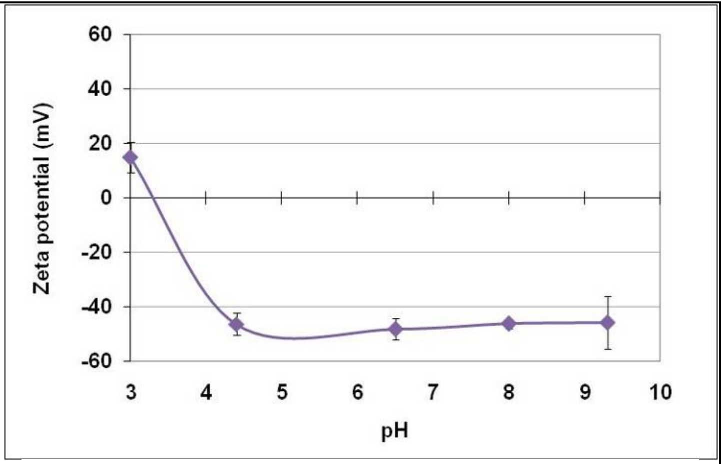

Figure 12: Zeta potential of Collargol colloidal silver solution in Millipore ultrapure water. pH adjustments accomplished with HNO_3 or NaOH

Compositional Analysis

Inductively coupled plasma with mass spectroscopy (ICP-MS) was employed to determine the elemental composition of the colloidal silver solution. As mixed, the application solution is expected to contain 250 ppm of Collargol powder, with around 25-30 present as casein, as well as residuals from manufacturing processes. When conducted on two different samples mixed in accordance with the application solution procedures, ICP-MS showed silver concentrations of 178 and 190 ppm, as expected.

Silver was found to comprise approximately 93 percent by mass of the application solution metals content. As shown in Table 6, the remaining 7 percent was made up mostly of sodium and iron. The relatively high sodium content is expected given the use of casein for suspension.

Given that ICP-MS analysis returned a metals content of which 93 percent was silver, the application solution has very few trace contaminants detectable.

Previous ICP-MS analysis was conducted on a 3.2 percent stock solution obtained from a Nicaragua factory. In that case, the silver content was determined to be 19.5 mg/L instead of the anticipated 32 mg/L (Wright and Bielefeldt 2005). This deficiency of nearly 40% could have also likely

Table 6: Elemental composition of the Collargol colloidal silver solution as determined by ICP-MS

Element	(ppb)	(% of total)
Ag	**178753**	**92.61%**
Na	10782	5.59%
Fe	2303	1.19%
B	1045	0.54%
P	85.63	0.04%
Br	35.69	0.02%
Au	6.37	0.00%
Zn	5.66	0.00%
Mo	2.15	0.00%
Be	1.91	0.00%
Sn	0.83	0.00%
Li	0.76	0.00%
Pb	0.60	0.00%
V	0.27	0.00%
Sb	0.19	0.00%
Co	0.18	0.00%
∑	193023	100.00%

been due to the use of a stabilizing compound (such as casein). But since the Microdyn product likely present in that sample is no longer in production, little more information is available.

Nanoparticle versus Ionic Silver

The physico-chemical state of the colloidal silver found in suspension was determined in order to understand whether the silver is being deposited onto the ceramic surface as a nanoparticle, or if the attachment may be taking place as ionic silver. The solution used for analysis was mixed at a nominal target concentration of 5 mg/L silver. Given the ICP-MS results presented above, as well as the manufacturer specifications, that concentration was approximately 3.5 mg/L silver.

After 1 hour of centrifugation at 288,000 g's, the supernatant was pulled from the sample and then analyzed for silver content using ICP-MS. Since the pellet was left out of the analysis, these results represent the ionic fraction of the silver content. This sample had an ionic silver concentration of 0.35 ppm, which is approximately 10 percent of the total silver.

After 2 hours of centrifugation, the sample had an ionic silver concentration of 0.33 ppm. Since the difference in ionic silver concentration was very slight between those two samples, longer centrifugation times to further fractionate the sample were deemed unnecessary.

These data show that when mixed into ultrapure water, the colloidal silver solution is comprised mainly of nanoparticles, with around 10 percent of the silver content being ionic.

Table 7: Total silver content of the application solution and ionic silver content of the centrifuged samples

Specimen	Description	Silver content (ppm)
Application Solution	Mixed per ceramic pot filter production specifications. Expected content is 175 to 190 ppm.	179 190
Centrifuged samples	1 hour centrifugation at 288,000 g's. Initial silver solution was 3.5 mg/L.	0.35
	2 hour centrifugation at 288,000 g's. Initial silver solution was 3.5 mg/L.	0.33

Preliminary QCM Data

The data presented in this sub-section was collected using the Stanford Research System (SRS) QCM 200. All sensors used for this preliminary data were the standard quartz sensor with gold electrode (that is, these sensors were not coated with silica). These results show good correlation with dry measurements recorded by the Q-sense E4 machine. Flow experiments conducted with the SRS device were useful in forming the direction of the investigation presented in this thesis.

Baseline Flow

Agreement was decent between the theoretical and recorded frequency and resistance shifts. The SRS machine only records the first harmonic, and the electrical resistance associated with that fundamental resonant frequency.

Millipore ultrapure water, flowing across the surface of the sensor at a rate of 0.2 mL/min, resulted in an average frequency shift of -774 Hz (+/- 56 Hz, $\alpha = 0.05$, n = 27) and an average electrical resistance of 337 Ohms (+/- 37 Ohms, $\alpha = 0.05$, n - 24). This is in relatively good agreement with the theoretical values of –697 Hz and 368 Ohms, calculated at 22° C. The resistance measurement seems to provide a more accurate response to the viscosity of the water on the surface of the sensor.

Silver Deposition

QCM 200 measurements taken after silver deposition differed from the expected value of -126 Hz, calculated at a deposited silver quantity of 890 ng. If the entire mass of 1.27 µg of Collargol powder were detectable, the frequency shift would be -180 Hz. The average measured frequency shift was -280 Hz (+/- 136 Hz, $\alpha = 0.05$, $n = 3$), with the data set shown in Figure 13.

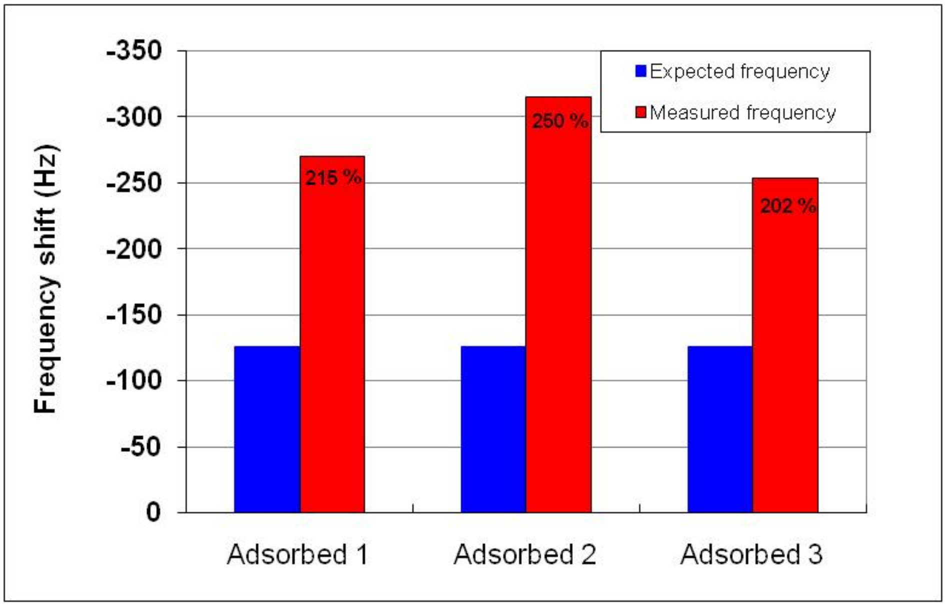

Figure 13: Preliminary measurements of frequency shift due to deposited silver

It is not altogether surprising that the measured values do not correlate perfectly with the expected value. The expected frequency shift was determined from the Collargol concentration of the application solution and the volume of solution drop cast onto the surface of the crystal by mechanical pipette. The Sauerbrey equation (Equation 2) provided the expected frequency shift based on the "known" amount of silver deposited. Sources for error in this approach are many, including pipette procedures, pipette calibration, silver location, and silver distribution once deposited. Related to that, one of the primary concerns is that the Sauerbrey conditions – of a rigid, thin, uniform, and well-attached film – may not be met by the simple drop casting procedures.

For that reason, a handful of sensors were coated using a sputtering technique, which deposits a thin film of silver in a much more controlled fashion, better adhering to the requirements of the Sauerbrey equation (Madou 1997). A range of different film thicknesses were applied, from 4 to 400 nanometers, according to the thickness monitor associated with the Gatan PECS sputter machine. Thickness measurements were confirmed by profilometry. Using the area of the sensor electrode and the measured film thickness, combined with the bulk density of silver, an expected mass of detectable silver was calculated for each sensor.

Interestingly, the sputtered mass detected by QCM was consistently short of the expected values, in contrast to the results seen for the adsorbed silver. Shown in Figure 14 is a plot of the data, normalized to the expected values so that the QCM measurements are shown as a percent

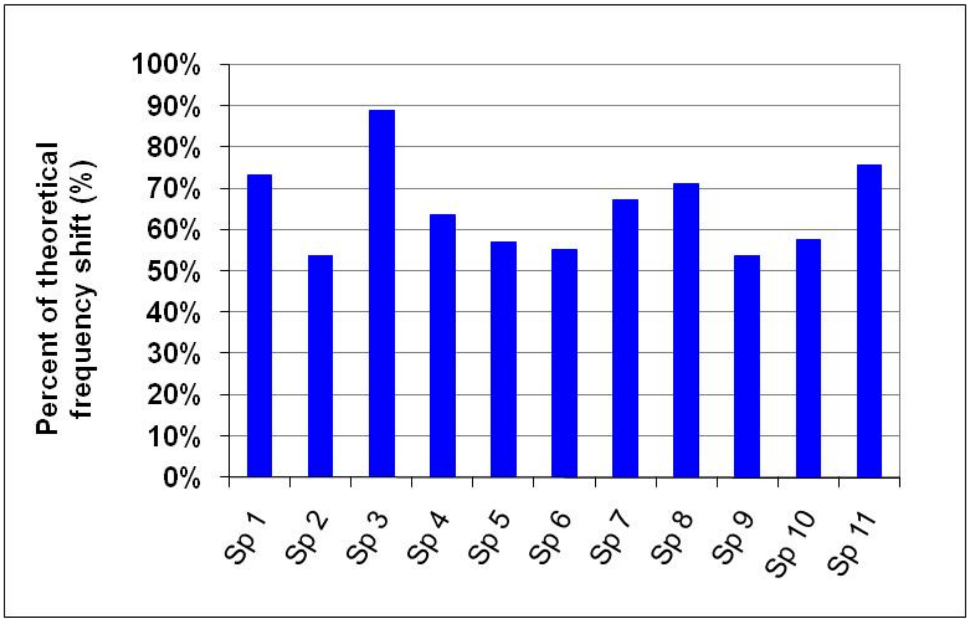

Figure 14: Frequency shifts of QCM sensors with sputter-coated silver, shown as a percentage of theoretical shift

of the expected value. With silver sputtered at a range of different thicknesses, the QCM detects around 65 percent (+/- 25 %, α = 0.05, n = 11) of the expected mass.

This difference is not well understood and is a good candidate for future research.

The electrical resistance measurements are not reported for the case of the silver deposition measurements. The deposited silver, whether adsorbed or sputtered, has no appreciable visco-elastic behavior to cause change from the baseline resistance measurements.

Silver Flow

The SRS QCM 200 device was used to flow ultrapure water across the surface of silver coated sensors in order to monitor the rate of release of that silver. While the results were not thoroughly analyzed for significance, there were noticeable changes in the frequency over time, suggesting a release of silver from the surface.

A schematic of the expected frequency response during all QCM experiments is included as Figure 15. The initial shift in frequency for the Silver Flow experiment is shown as the sum of the frequency shifts due to the flow of water and due to the mass of the

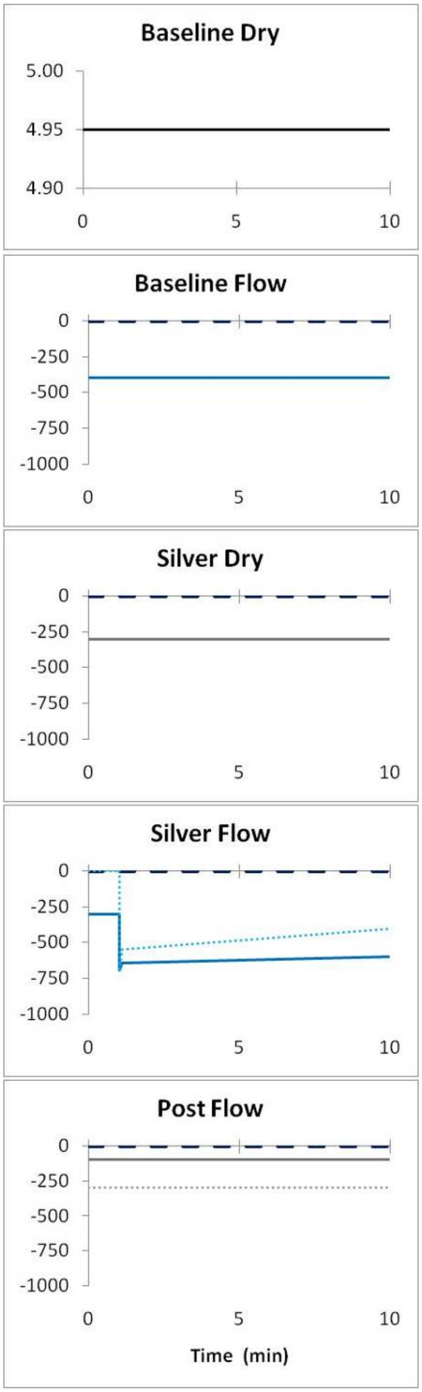

Figure 15: Schematic of frequency response expected for each QCM experiment

Table 8: Equivalent effluent silver concentrations according to the Sauerbrey correlation

Quantity Ag deposited	Deposition technique	Flow conditions	Change in frequency (first harmonic)	Change in time	Calculated equivalent concentrations
1.8 µg	Adsorption	Millipore ultrapure water	75 Hz	100 min	20-60 ppb
12 µg			35 Hz	45 min	20-60 ppb
2 µg	Sputter	Millipore ultrapure water	2-3 Hz	120 min	< 2 ppb
20 µg			2-3 Hz	100 min	0-2 ppb
80 µg			19 Hz	75 min	8-10 ppb
1.8 µg	Adsorption	10^8 CFU/mL in broth	125 Hz	4 min	>1000 ppb

silver deposited, in accordance with the superposition principle (Martin et al. 1991). It is assumed that the frequency shift found at the end of the Silver Flow experiment (relative to Baseline Flow) will match the Post Flow frequency shift (relative to Baseline Dry). The plot showing the Silver Flow has lines representing two outcomes; the solid blue line is that of a small initial flushing, followed by a slow release of silver, while the dashed blue line would be characteristic of a substantial release of silver during initial flushing, followed by a higher release of silver. The solid line case shown in the Silver Flow plot matches the solid line of the Post Flow plot; likewise for the dashed lines.

The equivalent mass concentrations shown in Table 8 are intended as an estimate of the silver concentration of the effluent water. These equivalent concentrations were calculated assuming that the Sauerbrey conditions were met, correlating the change in frequency in direct proportion to a change in mass. These concentration estimates were not verified by analysis of the effluent stream (until future experiments were conducted with sodium hypochlorite, as discussed in the relevant sub-section below).

The experimental set up for the SRS QCM 200 studies was not nearly as controlled as that for the Q-sense system. Efforts were made to use a constant sensor clamping force for each run, as well as to equilibrate the sensor and all water and other materials to room temperature. In most cases, the sample water was ultrapure water directly from the Millipore system, so the sample water preparation step was considered to be repeatable. However, the QCM 200 system is only designed to record information from one sensor at any given time, eliminating the data set that the Q-sense system produces by running four sensors in parallel using the exact same influent water.

A preliminary experiment was also conducted where the influent water was comprised of ten percent (v/v) tryptic soy broth (TSB) (ionic strength of 21 mM; 300 mg/L of total chlorine; total organic carbon of around 1.2 g/L) in Millipure ultrapure water. Subsequently, a very high concentration of *E. coli* DH5-α indicator bacteria was spiked into the influent TSB solution (concentration estimated at 10^9 CFU/mL according to later enumeration of the stock solution under similar conditions). This influent condition had a remarkable effect on the rate of release of silver from the gold electrode of the sensor. Shown in Figure 16 is data from that experiment, where the sharply increasing slope at approximately 85 minutes into the experiment is an indication of the rapid release of silver caused by the TSB solution. An additional increase in the slope is seen around 140 minutes into the experiment, when the influent water was spiked with *E. coli*. Note that the magnitudes of the shifts of each sensor vary, as each sensor had a different mass of silver deposited. Sensor A was a control experiment, and had no silver on the surface to remove; the data shown for Sensor A is baseline data for these flow conditions.

The near-complete removal of silver was confirmed by visual inspection of the sensor surface at the completion of this experiment using the optical microscopy technique introduced earlier, which showed that no silver remained on the gold electrode. Further verification was provided by a post flow analysis, where the frequency readings had practically returned to their baseline values.

Immediately after that experimental run, it was unclear what component of the TSB and *E. coli* mixture was most responsible for the release of silver nanoparticles. One possible explanation is that the *E. coli* interacted with the silver nanoparticles, which could be a benefit to inactivate or inhibit bacteria in contact with the silver coating, but could be a disadvantage in that bacterially-contaminated waters could then potentially render the silver coating useless in a short time after exhausting the available silver nanoparticles.

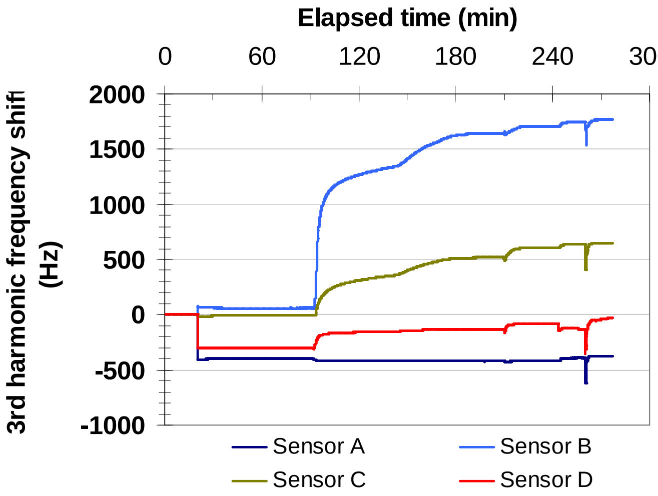

Figure 16: Example frequency plot of silver-coated QCM sensor exposed to influent waters containing 10% (v/v) TSB and ~ 10^9 CFU/mL *E. coli* (DH5-α)

Another preliminary run was conducted to determine the effects of the *E. coli* alone, without the 10 percent TSB solution. In this case, the *E. coli* was centrifuged and rinsed with phosphate buffered saline (PBS) three times before resuspending 1 mL of PBS (containing *E. coli*) into 99 mL of ultrapure water. The ionic strength of this sample water was on the order of 2 mM, with total chlorine concentration of around 50 mg/L. *E. coli* concentration was 9 x 10^4 CFU/mL after the washing. This condition had a much less noticeable effect on the rate of release of silver. Results from this experiment are shown in Figure 17. Again in this case, the flow was begun with a microbe-free solution, with the PBS and *E. coli* added to the influent at around 345 minutes into the experiment.

The initial rise in frequency once flow began was between 20 and 75 Hz within the first few minutes of water flowing across the sensor. That initial rise at 160 minutes is the release of silver due to

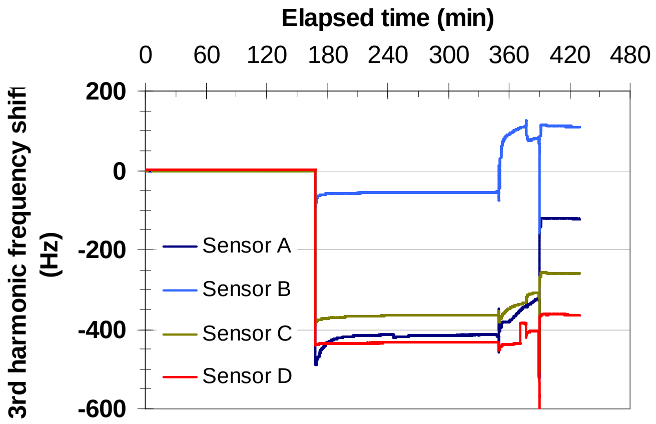

Figure 17: Example frequency response of silver-coated QCM sensor exposed to 1% PBS solution containing environmentally relevant concentration of *E. coli* (DH5-α)

a 1% PBS solution alone. Compared to the change of 100 to 1200 Hz in less than 10 minutes seen when the 10 percent TSB solution was run, the 1 percent PBS had a very minimal effect on the release rate of silver. However, similar to the effect noticed for the 10% TSB run, spiking the influent PBS solution with *E. coli* caused another jump in the frequency, seen at 345 minutes into the 1% PBS experiment. In this experiment, Sensor D is the control sensor, acting as a baseline for this experiment. Cleaning processes were begun at 375 minutes, causing some of the inconsistencies in the tail of the data shown in Figure 17.

The results of those preliminary runs provided insight into possible controlling factors on the release of silver from the unmodified quartz sensors. Evidently, the constituents of the water played a

Table 9: Rate of change of fundamental resonant frequency, arranged by influent water description

Experimental description (n = 4 for each experiment)	**Initial Region (minimum frequency to end-point)**				**Linear Region (end-point of Initial Region to final data point)**			
	Baseline slope	95% conf. int.	**Silver flow slope**	95% conf. int.	**Baseline slope**	95% conf. int.	**Silver flow slope**	95% conf. int.
	(Hz/min)		(Hz/min)		(Hz/min)		(Hz/min)	
10% TSB	-7.9	± 49.4	112.7	± 245.8	0.1	± 0.9	6.3	± 11.4
10% TSB + *E. coli* *	-	-	7.6	± 13.9	-	-	0.6	± 1.3
10.5 g/L NaOCl rinse *	-	-	6.0	± 6.8	-	-	0.2	± 0.3
1% PBS	-0.4	± 1.0	-	-	0.0	± 0.8	0.2	± 0.3
1% PBS + *E. coli* *	-	-	-0.3	± 0.9	-	-	0.0	± 0.0
10.5 g/L NaOCl rinse *	-	-	10.8	± 31.7	-	-	1.8	± 3.1

* - Analysis conducted in sequence; each rate of change was taken relative to the previous step.

larger role in the release of silver than the microbial concentration. This information led to the experimental outline to be performed on the Q-sense E4 QCM machine, which focused on water quality parameters in order to determine the effects of those individual parameters on the rate of release of silver. This is not to say that the microbial concentration does not have some impact on the rate of release, nor is it to say that the indicator *E. coli* bacteria is representative of all microorganisms that would be encountered during field use, but rather these experiments serve as a step towards understanding the importance of specific constituents within the influent water.

QCM Experiments

Experiments were conducted to measure the effects of pH, turbidity, ionic strength, natural organic matter (NOM), and sodium hypochlorite on the rate of release of silver from a silica coated QCM sensor. The variables tested within this experimental matrix are shown in Table 10.

Table 10: Summary table of sample waters used in QCM experiments

Parameter	Value	Description	n
Baseline	-	Millipore™ ultrapure water pH = 5.8	6
pH	4.8	pH adjusted with HNO_3	4
	9.3	pH adjusted with NaOH	3
turbidity	51.5 NTU	Kaolin powder added	4
ionic strength	150 mM	Monovalent ion, $NaNO_3$	4
	150 mM	Divalent ion, $Ca(NO_3)_2$	4
NaOCl	525 mg/L	Representative cleaning solution	4
	8.8 mg/L	Treated per drinking water quidelines	4
NOM	15 mg/L TOC	Pulled from Big Elk Meadow Lake, Colorado	4

Baseline Flow

As discussed in the Background section, theoretical values may be calculated for the frequency and dissipation shifts caused by a fluid with known density and viscosity (Table 3). As seen with the preliminary QCM data, there was good correlation between theoretical values and measured values.

Note that the preliminary data, recorded using the SRS 200 device, only measured the first fundamental frequency. The results obtained with the Q-sense E4 system demonstrate even better correlations for the higher harmonic frequencies, namely the third through ninth harmonics.

The bar graph included as Figure 18 is a representation of the measured frequency of each harmonic of interest (see Appendix D.2: Frequency and Dissipation Shifts for Baseline Flow for tabulated data). The left-most set of bars, labeled "All", includes data from every sample water, every sensor, with a total number of 39 data points included. The other sets of data are labeled according to the condition of the influent water. The error bars for this plot, and all other figures presented (unless otherwise specified), represent the 95 percent confidence interval as determined using Student's t-test with α equal to 0.05.

The mean for all of the sensors correlates extremely well with the theoretical shift in frequency, especially the measured value for the third harmonic. A trend exists in which the first harmonic is shifted slightly more negatively than theory predicts, causing its normalized value (as plotted) to exceed

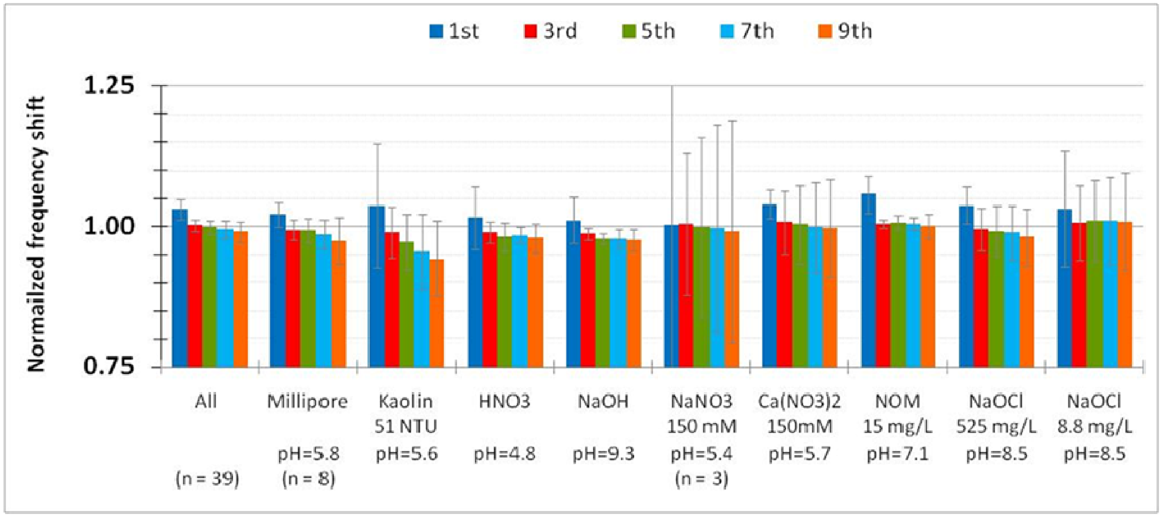

Figure 18: Frequency shifts during baseline flow measurements, normalized to theoretical value for each harmonic

one, with the third and higher harmonics shifting less than theoretical predictions (having normalized values less than one). In fact, each successively higher frequency shows a slightly larger departure from the predicted value, causing the normalized values to step down from the first to the third to the fifth harmonics, and so on. That same trend is present in all of the data sets for the individual sample waters.

Clearly some data sets have a wide variance in the measured frequency shifts. In particular, the baseline flow data from experimental runs with varied turbidity, ionic strength, and sodium hypochlorite show a much larger range for their 95 percent confidence intervals. In some cases, these larger error bars are due to the lower number of sensors that provided useful data; each of those data sets were analyzed with two to three sensors instead of four, which has a noticeable impact on the t-distribution. In some cases, the influent water itself may be interacting with the silica surface of the sensor, causing a fluctuation in the frequency reading. If that is the case, the intention of the baseline reading is to account for that type of fluctuation when running the flow experiment across the deposited silver.

Similarly, the dissipation shifts for each of those harmonics under baseline flow conditions are shown as Figure 19. The most obvious feature of these data is the major discrepancy between the

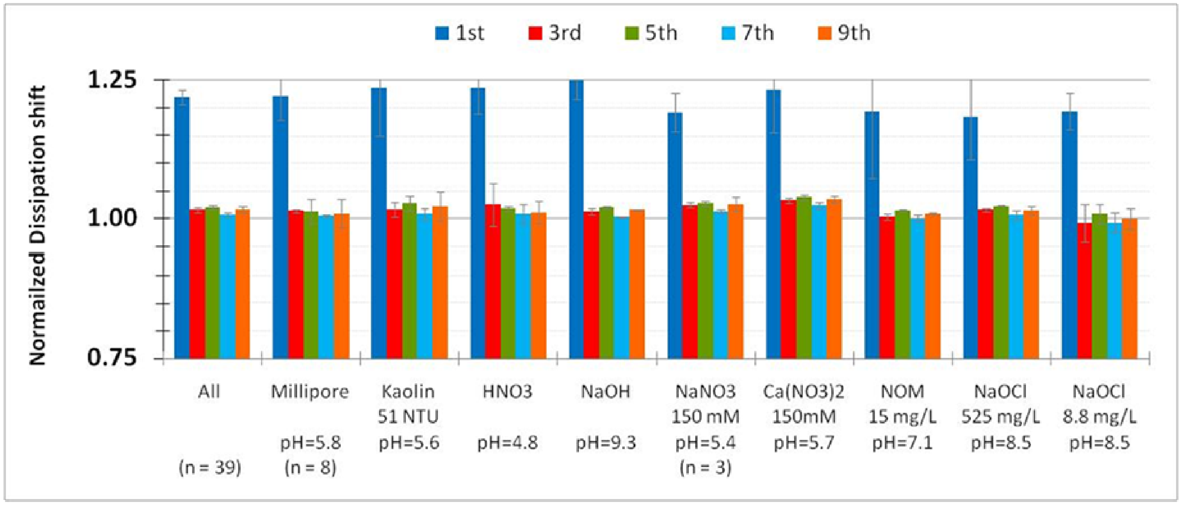

Figure 19: Dissipation shifts during baseline flow experiments, normalized to theoretical value for each harmonic

theoretical and measured values for the dissipation of the fundamental resonant frequency. While the third through ninth harmonics all correlate well to predicted values, the first harmonic deviates from predicted values by around 25 percent. In all cases, its shift is greater than the predicted value of 278 Hz. Keep in mind that each harmonic frequency has a characteristic decay length for any given media, which is always greater for the first harmonic. Perhaps the larger penetration depth of the first harmonic is a cause for these substantially higher dissipation readings, by allowing for more interference from the flow regime within the sensor holder.

In this dissipation data, there is not a prevalent step-wise trend between the higher frequencies as was seen in the frequency data.

Another means of viewing that same data is shown in Figure 20, a plot of the theoretical shift versus the actual shift for all data (n=35). Again, error bars around each data point represent the interval for 95 percent confidence. The dashed line within that plot has a slope of one to represent a perfect correlation with theory.

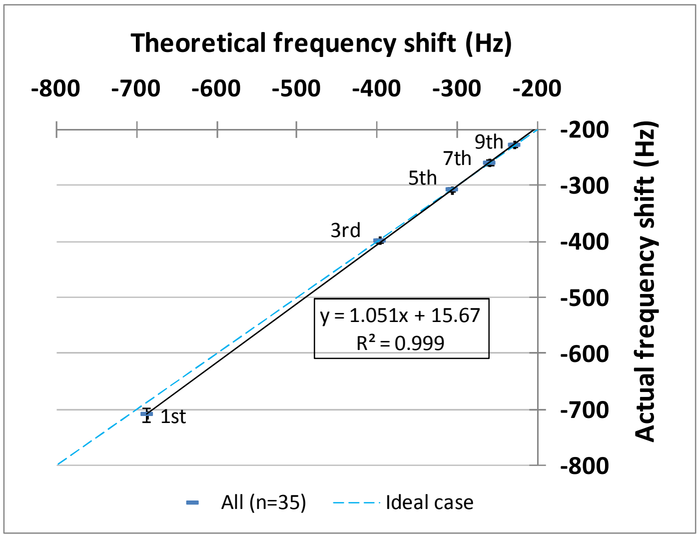

Figure 20: Actual vs Theoretical Frequency shifts for all harmonics during baseline flow experiment

The black trend line in Figure 20 is a line determined by least squares method for the plotted data. The r-squared value of 0.999 shows that this trend line accurately represents the data as a linear trend. The trend line's slope of 1.03 is remarkably close to the ideal value of 1.00.

A similar look at the dissipation data collected during baseline measurements may be found in Figure 21. This figure includes the same information as that described above for the frequency data: data points for the first through ninth harmonics for the entire data set (n=37), error bars at each of those points for the 95 percent confidence interval, and a black trend line through those data. The black trend line including all of those harmonics does not follow closely to the ideal case, since this best fit line has a slope of 1.4. The fit of the data is still relatively good, with an r-squared value of 0.993.

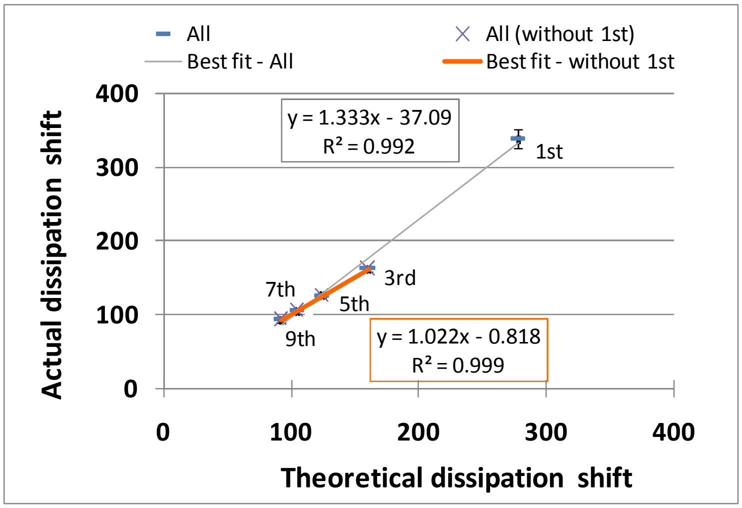

Figure 21: Actual vs Theoretical Dissipation shift for all harmonics during baseline flow experiment

Figure 21 also includes an alternate analysis in which the data from the first harmonic is not included when fitting the trend line. By eliminating that point, which was shown in Figure 19 to be approximately 25 percent away from predicted value, the dissipation data measured correlates much better with theory. The slope of the best fit line through the third, fifth, seventh, and ninth harmonics is 1.02, with an r-squared value of 0.999.

The trends that were seen during these baseline measurements confirm the approach for data analysis that was most prevalent in the literature, that of neglecting the first harmonic in favor of the third and higher harmonics (Poitras et al. 2009; Quevedo and Tufenkji 2009). Not only was the frequency correlation poor for the first harmonic, but also the dissipation results clearly indicate that the first harmonic does not accurately represent the values of the higher harmonics.

Results throughout this section, especially those from the silver flow runs, will place emphasis on the third harmonic in particular. The third harmonic represents the data better than the other harmonics considered (fifth, seventh, and ninth) when looking at the mean of the frequency shift for the baseline flow runs.

Silver Deposition

Each sensor was treated identically for the silver deposition process, allowing for the data of all sensors to be grouped, with 39 total sensors. Figure 22 shows the results of the silver deposition measurements, both frequency and dissipation, across each of the harmonics up through the ninth. The mean of each harmonic is plotted and the error bars cover the 95 percent confidence interval. Also included in that figure is a dashed line at 219 Hz, which is the expected shift for each of those scaled frequencies given the known deposition process, calculated by the Sauerbrey equation.

Interestingly, when measured on the Q-sense E4, the first harmonic returns a frequency shift closest to the calculated, expected shift. This is in contrast to the results obtained by the SRS system for the first harmonic, which exceeded the expected shifts by approximately 50 percent. It is noteworthy that the third through ninth harmonics measured by the Q-sense E4 match more closely with the frequency shifts of the SRS system.

Shown in Table 11 are results from a paired Student's t-test for each harmonic with the others. At $\alpha = 0.05$, matching the 95 percent confidence interval shown in all results, the frequency and dissipation shifts for the seventh and ninth harmonics may be considered the same (at $p=0.30$ and $p=0.11$, respectively). The frequency and dissipation shifts for all other harmonics are unique from the values of each of the others. This is likely due to decay length characteristics of each overtone, combined with the variable thickness and structural heterogeneity of the adsorbed silver.

Table 11: Paired t-test results for dry silver frequency and dissipation shift between each harmonic.

A Harmonic	B Harmonic	Frequency shift p-value	Dissipation shift p-value
1	3	< 0.001	0.478
1	5	< 0.001	0.256
1	7	< 0.001	0.047
1	9	< 0.001	0.014
3	5	< 0.001	0.012
3	7	< 0.001	0.012
3	9	< 0.001	0.012
5	7	< 0.001	0.005
5	9	0.042	< 0.001
7	9	0.297	0.111

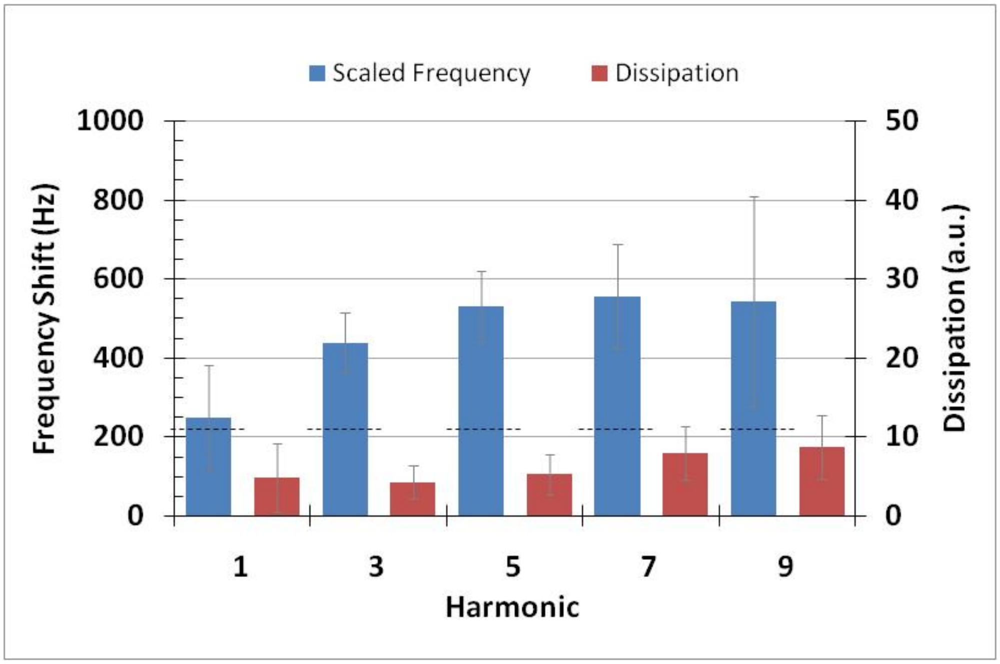

Figure 22: Frequency and dissipation shifts from silver deposition. Error bars represent 95% confidence interval (n=39). Dashed lines show the expected frequency shift given the mass of silver deposited, calculated by Sauerbrey equation

According to the principles presented in the Background section, the silver nanoparticles as deposited behave as a sufficiently rigid mass so that visco-elastic properties may be neglected. As shown in Figure 22, the shift in dissipation values caused by the addition of silver was on the order of 5-10 (x 10^{-6}) dissipation units. Dissipation shifts of that magnitude fall well below the threshold of around 10 percent of the magnitude of the frequency shift, meaning that elastic models (such as the Voigt model) are not well suited to describe this mass. For that reason, any comparisons of frequency shifts to mass have been calculated simply using the Sauerbrey correlation.

Drop casting the colloidal silver solution onto the silica surface is certainly not the best manner of silver deposition to meet the criteria of the Sauerbrey correlation. Drop casting is, however, a deposition process representative of the application method used during ceramic pot filter production. Brushing the colloidal silver solution onto the walls of the ceramic pot filter allows for a similar interaction between silver nanoparticles and the ceramic surface as when a drop is placed onto the QCM sensor surface.

Two primary concerns raised by drop casting these nanoparticles onto the sensor are the location within the overlapping electrode area, and the uniformity of the mass deposited. Every effort was made to center the 5 µL drop of the colloidal silver solution within the electrode area; in all cases, the entirety of the drop was contained within the overlapping area. As shown by Lu et al., a mass placed at the very outskirts of the overlapping electrode area will have a very small effect on the frequency readings, generally less than a few percent (2004). Effects caused by poor placement of the adsorbed silver are not sufficient to explain the discrepancy relative to the calculated, expected values in frequency shifts.

The uniformity of the deposited silver was not controlled beyond the deposition process. Localized deposits of mass may have impacted the frequency response of these readings. If localized deposits were the primary cause of the poorly correlated frequency readings, then one would expect to see extreme outliers within the data set, in that unique localized deposits could cause dramatic effects that would not be repeated. Another reason to assume that localized deposits did not have an important effect on the frequency readings is that a similar discrepancy (between theoretical or expected values, and actual values) was encountered when silver was deposited by sputtering, a method that deposits a much more uniform film than can be achieved by drop casting.

Post Flow Frequency Shift

A simple way to determine the effects of the flowing sample water across the silver nanoparticle-coated surface is to compare the reading of each sensor (with silver deposited) to the frequency reading of that same sensor after the silver flow run has been conducted. This is a static measurement of the overall frequency and dissipation shifts of each sensor caused by the flow experiment.

According to the principles of QCM measurements, a positive shift in frequency from the reading obtained immediately after silver deposition to the reading obtained post-flow indicates a release in mass. The magnitude of that shift is directly proportional to the quantity of mass released, when operating under the Sauerbrey conditions, as in this case. The maximum positive shift in frequency due to silver release is equal (and opposite) to the frequency shift caused by the deposition of silver; this is the limiting case of 100 percent release.

Presented as Figure 23 are the results from the post-flow frequency comparison. The mean for each harmonic, each data set, is plotted with error bars representing the 95 percent confidence interval. Figure 23 plots these data as absolute frequency shifts, which is important to see the directionality of the shift, and the variance of the data.

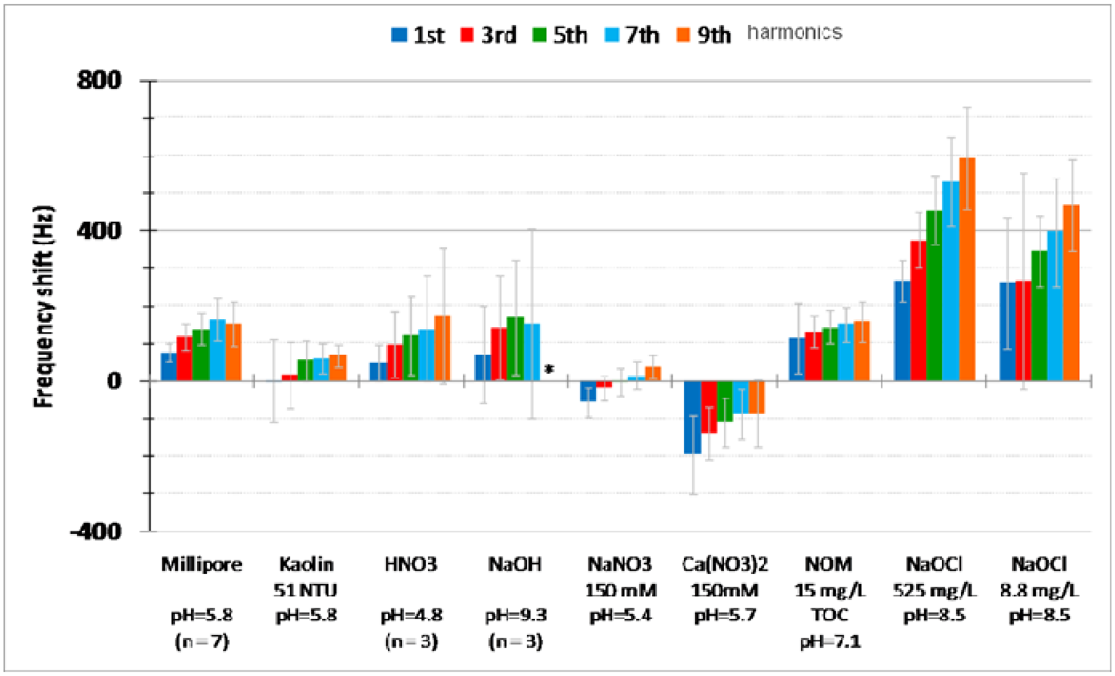

* - no data available for 9th harmonic of NaOH water.

Figure 23: Frequency shift caused by the silver flow experiment, taken as the difference between the dry post flow measurement and the initial dry silver measurement. Each sample water condition is represented by the group of columns showing 1st through 9th harmonics (n=4 for all conditions unless otherwise noted). Error bars represent 95% confidence interval.

While the error bars in Figure 23 give some perspective as to the statistical significance of each harmonic for each data set, more specific statistical detail is provided in Figure 24, which plots the p-values for each harmonic. A solid line is included at a p-value of 0.05, which corresponds with the significance of the 95 percent confidence interval. In agreement with the visual assessment of the confidence intervals provided in Figure 23, it can be seen that the sodium hypochlorite containing waters provide very significant release of silver. The baseline ultrapure water and the pH = 4.7 water also show a significant amount of silver released.

Even though many of the influent water qualities did not provide significant removal of silver, a great deal can still be learned from those experiments. For instance, in the case of the turbid water, the expectation was that the particles would physically remove some of the silver from the surface. This would be of interest to both help explain potential mechanisms of the preliminary QCM results, as well as to understand the variables of future experiments. Again in the case of the varied pH waters, significant removal of silver could have provided another variable to consider in instances of near complete removal of silver. Since the pH shift alone was not sufficient to cause significant silver release, any major releases of silver caused by waters with varied pH should not be contributed to the pH alone, but of course the effects of that varied pH on other potential reactions cannot be neglected.

The nitrate salt containing waters show a significant shift in frequency, but keep in mind that those frequency shifts were negative, corresponding with adding mass to the surface, not removing silver. For the divalent nitrate salt ($Ca(NO_3)_2$) in particular, the negative frequency shift was substantial. Given the influent concentration of 0.1 moles per liter of calcium, a total of around 50 mg of calcium flowed across the surface of each sensor during the 2 hour experiment. The negative frequency shift of around 200 Hz suggests that approximately 1 µg of mass was deposited onto the surface, according to the Sauerbrey equation. That is a very likely explanation for the frequency shifts, especially since that amount of mass is such a small percentage (0.002 percent) of the available calcium. It is assumed that the calcium would be attracted to the quartz surface given the expected negative charge at the surface. An interaction between the silver nanoparticles and the nitrate is unlikely as this decrease in frequency response was not seen for the waters containing nitric acid for pH adjustment.

A similar effect is likely occurring for the monovalent nitrate salt ($NaNO_3$), but with a much lesser amount of mass being deposited. In both cases, it is impossible to resolve the exact effects of silver nanoparticle release versus elemental deposition without further analytical analysis of the sensor surface after the flow experiment. Some insight may be gained by observing the greatly increased dissipation values in those two cases, but elemental analysis is recommended to better understand this phenomenon.

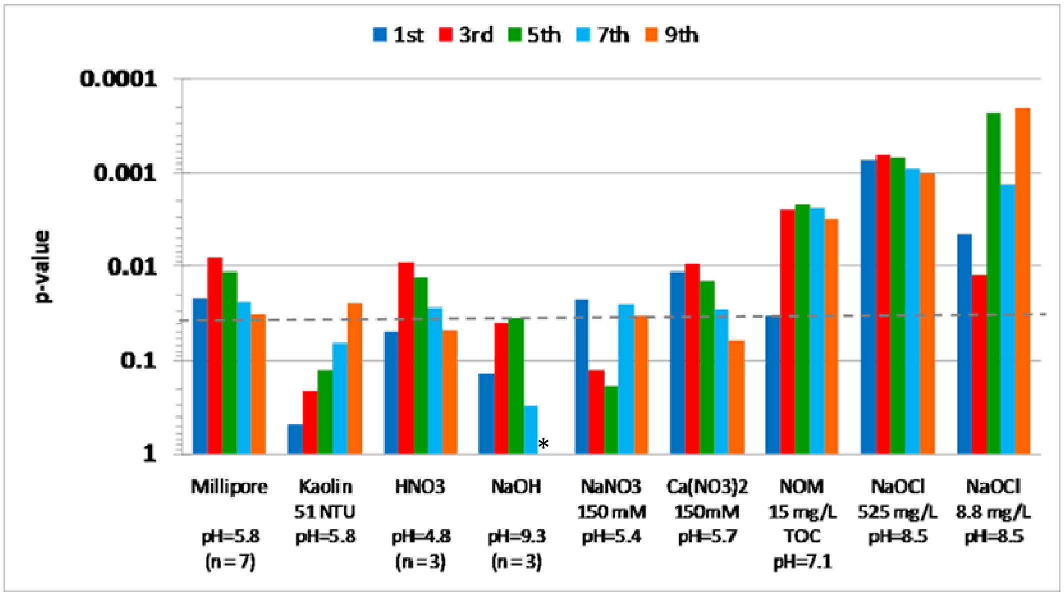

* - no data available for 9th harmonic of NaOH water.

Figure 24: Statistical significance of the frequency shifts caused during silver flow experiments, plotted as the p-value for each harmonic for each sample water. n = 4 unless otherwise stated. Dashed line shown at p = 0.05.

The very same data presented as Figure 23 can be normalized in order to better understand how much of the available, or deposited, silver was removed during the experimental run. The frequency shift for each sensor was divided by the frequency shift caused by the initial silver deposition process. This means that with no measurable shift from the experimental flow run, the normalized value would be zero. Or, if that specific sensor returned a 300 Hz shift for a given harmonic when silver was deposited, and that same harmonic showed a 150 Hz shift increase from pre- to post-flow measurements, then the normalized value of silver released would be 50 percent. These normalized results are shown below as Figure 25.

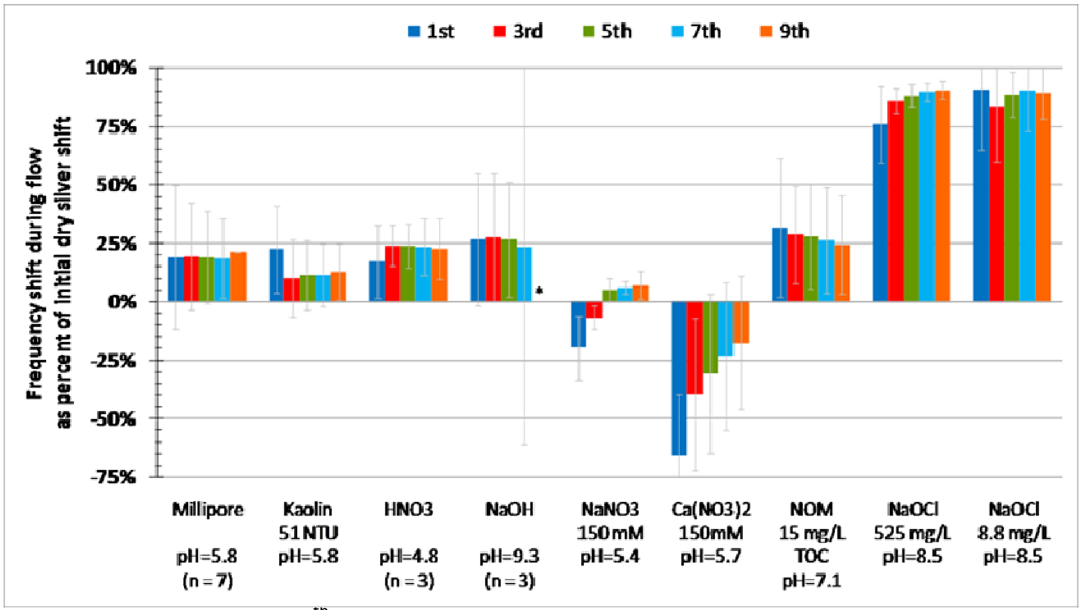

* - no data available for 9th harmonic of NaOH water.

Figure 25: Frequency shift during flow experiment normalized to initial dry silver frequency shift. Negative values indicate a further decrease in resonant frequency (related to mass deposition). Each sample water condition is represented by the group of columns showing 1st through 9th harmonics (n=4 for all conditions unless otherwise noted). Error bars represent 95% confidence interval.

The perspective gained by the normalized data brings a few different interpretations to the forefront. First of all, it is readily apparent that waters containing even very low concentrations of sodium hypochlorite have a dramatic effect on the release of silver nanoparticles from the silica surface. In both runs with sodium hypochlorite, at concentrations of 525 and 9 mg/L, approximately 90-100 percent of the deposited silver was removed. This was verified by visual inspection immediately after the silver flow run, and can be seen in the optical micrographs included as Appendix D.5: Optical Micrographs of Post Flow Condition. Those images are useful to confirm the near-complete removal of silver, as well as to verify that silver remains on the surface of the sensor in most other cases.

While the preliminary QCM data cannot be used for direct comparison, it can still provide insight into the effects of hypochlorite as compared to the chloride found in the TSB and PBS solutions. Sodium hypochlorite was run at concentrations of 0.12 and 7.0 mM for the 8.8 and 525 mg/L waters, respectively. The 10% TSB solution run during the preliminary investigation contained approximately 8.6 mM chloride, comparable to the concentration of hypochlorite found in the solution representative of a bleach cleaning solution (525 mg/L of NaOCl). The immediate removal of silver was apparent in that TSB experiment, but there were too many other factors at play to attribute the silver loss to the chloride in solution. In fact, the 1% PBS solution contained 1.4 mM chloride, the same order of magnitude as the 8.8 mg/L NaOCl water, yet the PBS solution did not affect the silver as greatly as the sodium hypochlorite containing water. This goes to show that the stronger oxidizer, hypochlorite, has a stronger effect on the rate of release of silver than chloride alone. Further investigation could be conducted to find trends between hypochlorite concentrations, oxygen content of the water, and the rate of release of silver nanoparticles from the ceramic surface.

Also of note for the normalized frequency shift data is the large interval required to achieve 95 percent confidence level, especially when compared to the mean for those data sets. This suggests that some of these data are statistically insignificant even though the mean alone would show a 10-30 percent removal of the deposited silver; such is the case for the turbidity and high pH waters.

The baseline water, Millipore ultrapure water, removed approximately 20 percent of the available silver. For the baseline water, as well as the pH and turbidity adjusted water, there is extremely good correlation between the multiple harmonics for each data set. While the sodium hypochlorite containing waters have means that vary slightly across the harmonics of interest, the 95 percent confidence interval places all of those values at an equal level. There are no real trends across the harmonics, except for the sample waters of nitrate salts.

Since the deposited silver is behaving as a rigid thin film (shown by its low dissipation values), the characteristic penetration depth of each harmonic is much less important than when the film being considered has visco-elastic properties, or when the specimen is submerged in a liquid (recall that these post flow measurements are all taken dry). Another potential parameter that can impact trends between the harmonics is the heterogeneity of the surface coverage, causing unique frequency trapping phenomenon at each resonant frequency. This effect is again most noticeable when the measurement is being recorded while submerged, and will likely not effect these post-flow measurements (Rechendorff et al. 2007). Efforts to more accurately model those types of effects could be useful to better interpret these data, but that is beyond the scope of this investigation.

As mentioned above, the waters at 150 mM with mono- and divalent nitrate salts caused unexpected behavior during the flow run. Those sample waters caused a further decrease in the resonant frequencies, suggesting additional mass was deposited onto the surface during the experimental flow run. Dissipation values for these data sets were shifted higher than baseline, suggesting that whatever mass was deposited had some visco-elastic properties (relative to the deposited silver).

The results from these nitrate salt runs also have a noticeable trend through the harmonics, where the first harmonic shows a larger shift in frequency than the successively higher harmonics. This type of effect was noticed within the baseline flow results presented above. In that case, it was assumed to be an effect of the visco-elastic behavior of the fluid in contact with the oscillating crystal. That explanation does not necessarily fit the results for the nitrate salt-containing waters because these measurements were taken dry, but perhaps entrained water caused some of that shift.

Although these measurements are static, they can still be confounded by other interactions during the silver flow run beyond a simple release of nanoparticles from the surface. The addition of mass to the surface of the sensor through gravitational settling or through chemical attraction during the experimental run is a possibility. The additional mass would cause a decrease in resonant frequency, offsetting some of the frequency increase that may have taken place from a release of silver. It is even conceivable that under perfect conditions, equilibrium could exist with a sample water where 50 percent of the nanoparticles would leave the surface of the sensor in exchange for the same mass of a substance contained within the influent water. If that were the case, then these static measurements would show absolutely no change from the pre- to post-flow condition. That type of effect is not expected for these experiments, but provided as an example for a general picture of potential effects of interferents.

A similar effect may be occurring when the waters contained increased levels of turbidity, specifically kaolin particles. As seen in Figure 25, the effect is subtle compared to the offsetting frequency shifts of the waters with elevated ionic strengths, but there is a noticeable drop in the frequency shifts of the third, fifth, seventh, and ninth harmonics recorded for the sample water at 51 NTU.

Given the surface charge characteristics of the kaolin particles and the silica surface both being negative, a lesser interaction is expected relative to that seen for the sodium and calcium ions. These results fit with that expectation, which also could explain the increased forces of interaction of the calcium ions relative to the sodium ions. The divalent ions would have a greater positive charge, increasing their propensity to deposit onto the silica surface.

Further study is required to determine what types of effects occurred during the experimental runs with elevated turbidity and ionic strength.

Silver Flow Results

For analysis of the silver flow runs themselves, the third harmonic was selected as the frequency to monitor. All measurements were started with the sensor dry, but located within the flow cell. The pump was turned on to commence flow within a few minutes of initializing the measurement.

As the sample water filled the volume above the sensor, an obvious drop in frequency occurred, as expected. Theoretically, the drop in frequency should be equal to the drop in frequency seen during the baseline flow measurements. Each and every sensor strayed from that ideal behavior; instead, the drop in frequency during the silver flow run was always less than that of the baseline experiment. An example plot of the data obtained during the silver flow run is included as the thicker lines in Figure 26. On the same plot, the reader will see a set of thinner lines that were recorded during the baseline flow run for the same four sensors. For data from each of the baseline and silver flow runs, see Appendix D: Results.

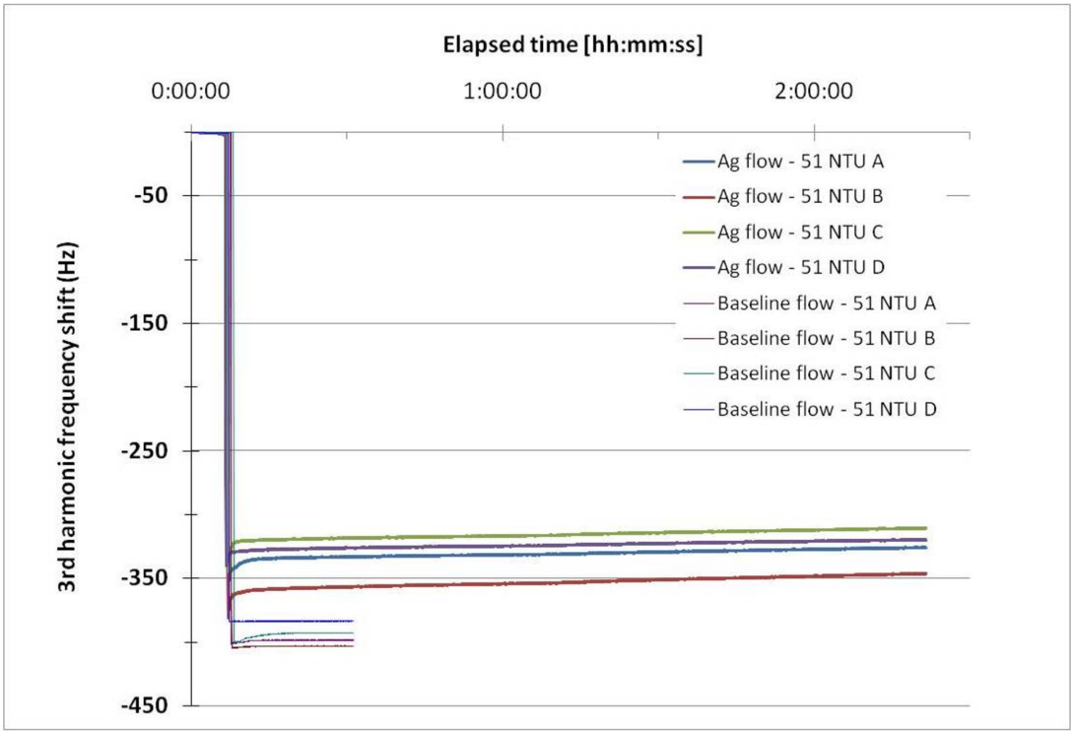

Figure 26: Example plot of data collected during Baseline and Silver flow experiments

The baseline flow measurements were all measured to be 397.5 Hz (+/- 4.1 Hz, α = 0.05, n = 37). As can be seen in the example plot above, as well as the others included in Appendix D: Results, the initial decrease in frequency during the silver flow run was less, at around 325-375 Hz.

There is a characteristic shape to the third harmonic's response during the silver flow run. As soon as the sample water covers the sensor, a major drop in frequency occurs. Almost immediately thereafter, the resonant frequency bounces back up and then begins to level off to a linear reading. That behavior, seen in almost every sensor analyzed, calls for a piecewise analytical approach, allowing for interpretation of the initial response separate from the linear region of the flow.

Further discussion will refer to either the initial region or to the linear, stable region. The division between those two regions was made visually, with validation provided by the linear fitting parameters returned for the linear region; the r-squared value for the linear region of each sensor was generally larger than 0.8, however, there were instances of very low r-squared values below 0.2. Even at those low values, the linearity of the data was confirmed by very large F-values, with the related p-value less than 0.0001 for the linear region of each sensor.

Initial region analysis

The initial frequency response is a complex interaction of the silver-coated sensor with influent water. Not only is the sensor adjusting to the new presence of the fluid over its surface, but also, that water may be having substantial effects on the silver itself. One possible outcome is an immediate flushing of silver, which would cause a relative increase in frequency as mass is being removed. This flushing effect is a likely explanation for (1) the lesser frequency decrease compared to baseline flow and (2) the immediate and sharp frequency increase witnessed in almost all experimental runs.

Some effort was made to model the initial region as a logarithmic trend beginning from the minimum frequency for each sensor. Shown in Figure 27 is an example of the initial region of data from the same four sensors shown above in Figure 26. This plot is a zoomed in view of the first few minutes after the sample water had contacted the sensor, showing the immediate and sharp frequency increase in greater detail.

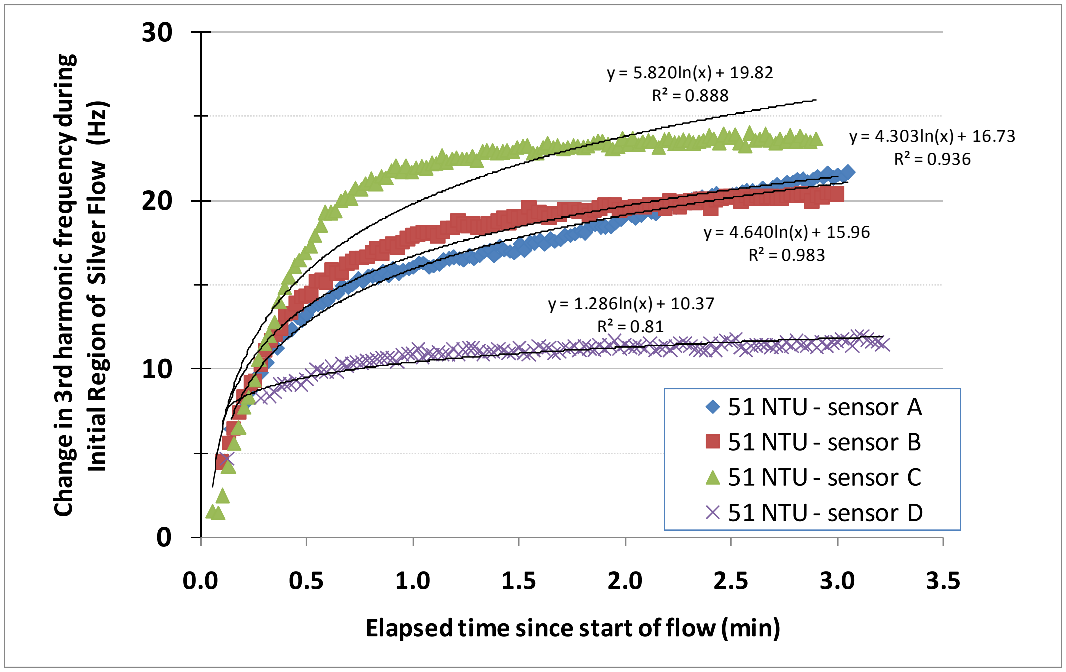

Figure 27: Example plot of Initial Region data of the 3rd harmonic for Silver Flow experiment

Many of the initial region measurements fit a logarithmic trend at a reasonably high r-squared value (0.80 or greater). However, there were a substantial number of sensors that responded in a manner not readily described by a logarithmic function. That, combined with the wide range of curve-fit parameters for each data set, was reason enough to seek other means of interpreting this initial region of data.

Without a reliable and consistent model to accurately describe the frequency response of the initial region, it was decided to analyze the initial regions by simple differential frequency shifts. Two differences were calculated for each sensor: first, the difference between the dry silver reading and the minimum frequency recorded and second, the difference between the minimum frequency and the end-point frequency of the initial region.

Table 12: Baseline flow frequency shift of the 3rd harmonic during the Initial Region.

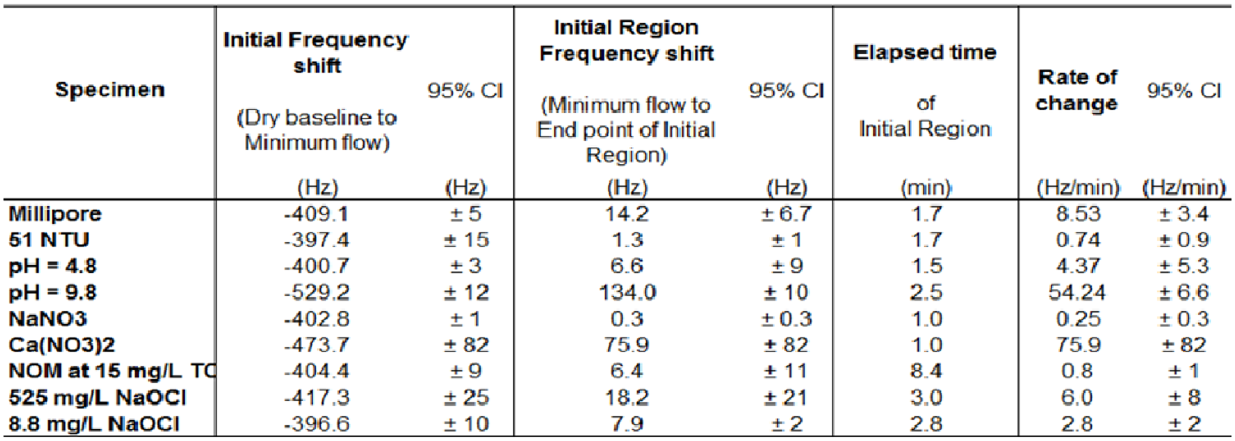

Specimen	Initial Frequency shift (Dry baseline to Minimum flow) (Hz)	95% CI (Hz)	Initial Region Frequency shift (Minimum flow to End point of Initial Region) (Hz)	95% CI (Hz)	Elapsed time of Initial Region (min)	Rate of change (Hz/min)	95% CI (Hz/min)
Millipore	-409.1	± 5	14.2	± 6.7	1.7	8.53	± 3.4
51 NTU	-397.4	± 15	1.3	± 1	1.7	0.74	± 0.9
pH = 4.8	-400.7	± 3	6.6	± 9	1.5	4.37	± 5.3
pH = 9.8	-529.2	± 12	134.0	± 10	2.5	54.24	± 6.6
NaNO3	-402.8	± 1	0.3	± 0.3	1.0	0.25	± 0.3
Ca(NO3)2	-473.7	± 82	75.9	± 82	1.0	75.9	± 82
NOM at 15 mg/L TC	-404.4	± 9	6.4	± 11	8.4	0.8	± 1
525 mg/L NaOCl	-417.3	± 25	18.2	± 21	3.0	6.0	± 8
8.8 mg/L NaOCl	-396.6	± 10	7.9	± 2	2.8	2.8	± 2

The difference between the dry silver reading and the minimum frequency recorded should theoretically be equal to that of the frequency shift seen during the baseline flow run. As mentioned above, the minimum frequency shift for most of these sensors, at around 325 to 375 Hz, was less than the baseline flow frequency shift. Table 12 contains the Baseline frequency shift and the minimum frequency shift for each sensor, grouped by experimental run.

Table 13: Silver flow experiment frequency shift of the 3rd harmonic during the Initial Region.

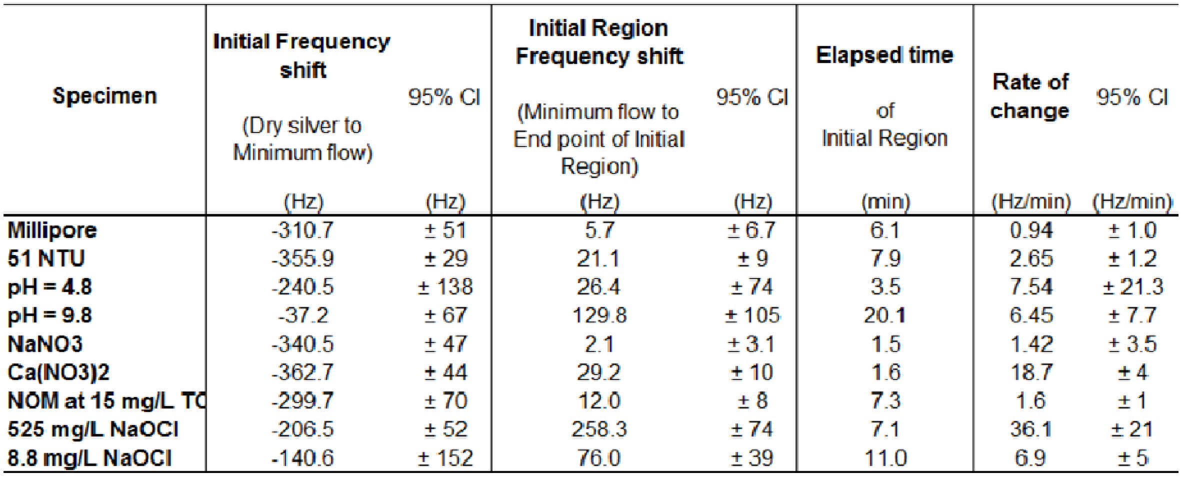

Specimen	Initial Frequency shift (Dry silver to Minimum flow) (Hz)	95% CI (Hz)	Initial Region Frequency shift (Minimum flow to End point of Initial Region) (Hz)	95% CI (Hz)	Elapsed time of Initial Region (min)	Rate of change (Hz/min)	95% CI (Hz/min)
Millipore	-310.7	± 51	5.7	± 6.7	6.1	0.94	± 1.0
51 NTU	-355.9	± 29	21.1	± 9	7.9	2.65	± 1.2
pH = 4.8	-240.5	± 138	26.4	± 74	3.5	7.54	± 21.3
pH = 9.8	-37.2	± 67	129.8	± 105	20.1	6.45	± 7.7
NaNO3	-340.5	± 47	2.1	± 3.1	1.5	1.42	± 3.5
Ca(NO3)2	-362.7	± 44	29.2	± 10	1.6	18.7	± 4
NOM at 15 mg/L TC	-299.7	± 70	12.0	± 8	7.3	1.6	± 1
525 mg/L NaOCl	-206.5	± 52	258.3	± 74	7.1	36.1	± 21
8.8 mg/L NaOCl	-140.6	± 152	76.0	± 39	11.0	6.9	± 5

That discrepancy is not well explained by the surface roughness inherent with the adsorbed silver nanoparticles. As shown by Rechendorff et al., surface roughness on the order of 30 nm (a comparable characteristic dimension of the adsorbed nanoparticles) can impact the resonant frequency of a sensor submerged in a liquid by trapping small pockets of the liquid in the open spaces on the surface (2007). Frequency shifts of around 10-20 percent greater than expected were reported for the first through seventh harmonics. The results presented here show frequency shifts around 10-20 percent less than theoretical and baseline values.

Also included in Table 12 is data related to the second frequency difference analyzed for the initial region, that from the minimum frequency up to the end-point of the logarithmic region. This frequency shift is recorded along with the change in time for each sensor, also shown in Table 12.

Since a flushing of loosely associated silver nanoparticles is a likely explanation for the frequency shifts seen in this initial region, a comparison to the frequency change from pre- to post-flow is

Table 14: Initial Region 3rd harmonic rate of change for Baseline and Silver flow experiments. A paired Student's t-test was used to deermine the p-value for comparing these data sets

	Baseline (Hz/min)	95% CI	**Silver flow** (Hz/min)	95% CI	**p-value**
Millipore	8.53	± 3.4	0.94	± 1.0	0.002
51 NTU	0.74	± 0.9	2.65	± 1.2	0.004
pH = 4.8	4.37	± 5.3	7.54	± 21	0.537
pH = 9.8	54.2	± 6.6	6.45	± 7.7	0.001
NaNO3	0.25	± 0.3	1.42	± 3.5	0.258
Ca(NO3)2	75.9	± 82	18.7	± 3.9	0.119
NOM at 15 mg/L	0.77	± 1	1.65	± 0.8	0.007
525 mg/L NaOCl	6.04	± 8.0	36.1	± 21	0.006
8.8 mg/L NaOCl	2.80	± 1.6	6.94	± 5.4	0.136

important. As presented above, the sample waters that had a significant and measurable effect of releasing silver from the sensor's surface included baseline ultrapure water, water at pH of 4.8, and waters containing sodium hypochlorite. Also recall that the waters containing nitrate salts had a reverse effect of causing a significant frequency drop over the course of the flow experiment. When comparing those results to the data from the initial region (Table 13), a direct correlation is not seen.

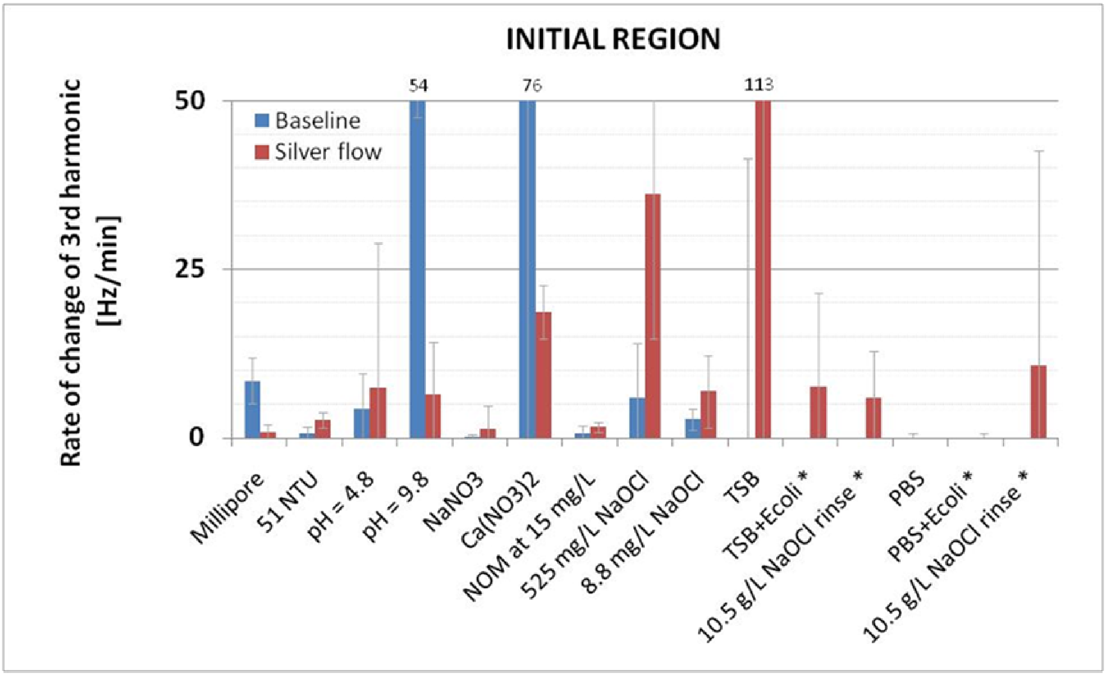

* - Experiment performed in sequence with previous data. Rate of change calculated from the previous plateau rather than from the minimum flow frequency.

Figure 28: Initial Region rate of change of the 3rd harmonic. Error bars represent 95% confidence interval. Mean values are included for data exceeding the axis maximum.

There are, however, some trends in the magnitude and direction of the frequency shift. For instance, the sodium hypochlorite containing waters caused an initial increase in frequency when the flow experiment commenced. This result is consistent with predicted results for an immediate release of 90 to 100 percent of the silver. Since the pre- to post-flow results for those sensors showed a loss of that amount of silver, verified by visual inspection and microscopic imaging, it is expected that during the silver flow run, the third harmonic would increase by nearly 300 Hz (the total possible shift as determined by the silver dry measurement). Perhaps this initial region of data is capturing that immediate effect.

Even with those trends present, the initial frequency shifts do not accurately describe the release of silver under these experimental conditions. The complex interactions at the time of initial flow across the surface of the sensor may overwhelm the ability to detect the continued presence of, or release of, the silver nanoparticles.

Linear region analysis

The linear region of the silver flow experiments was also analyzed to determine its relevance to the release of silver from the sensor surface. This linear region of data begins at the end-point of the initial region, so the analysis of these two regions covers the entire data set recorded for each sensor. Each point of the raw data across the linear region was used to calculate a best-fit trend line according to the least squares method. Of most interest is the slope of that line, as that would relate to a rate of release of silver, which could be used to calculate a mass-based concentration if the Sauerbrey conditions are considered to be valid.

Provided as Table 15 is a summary of the trend line slopes for the silver flow experiments (a more complete table of the trend line parameters is included in Appendix D: Results). The slopes of the linear regions have been tabulated as a time rate of change with units of Hz per minute. Also included is the range for the 95 percent confidence interval for each experimental run.

Table 15: Linear Region 3rd harmonic rate of change for Baseline and Silver flow experiments. The p-value was calculated as a paired t-test between the Basweline and Silver flow data for each influent water quality

	Baseline (Hz/min)	95% CI	**Silver flow** (Hz/min)	95% CI	**p-value**
Millipore	0.083	± 0.04	0.056	± 0.03	0.203
51 NTU	0.086	± 0.17	0.075	± 0.02	0.848
pH = 4.8	0.03	± 0.03	0.065	± 0.03	0.027
pH = 9.8	0.175	± 0.07	0.017	± 0.02	0.007
NaNO3	0.070	± 0.18	0.102	± 0.02	0.512
Ca(NO3)2	0.067	± 0.08	0.101	± 0.04	0.257
NOM at 15 mg/L	0.020	± 0.07	0.110	± 0.09	0.065
525 mg/L NaOCl	0.025	± 0.10	0.127	± 0.03	0.034
8.8 mg/L NaOCl	0.016	± 0.02	0.058	± 0.02	0.041

The variance in this data, both for the baseline slopes, as well as for the slopes of the silver run data, causes a rather large interval at 95 percent confidence level for each experimental set. Since the 95 percent confidence interval for the baseline slopes generally includes zero within its bounds, most of the baseline slopes are not statistically different than zero. Beyond that, most of the 95 percent confidence intervals for the slopes from the silver runs contain the mean of the baseline slope within their bounds, meaning that there is a good chance that the slopes from the silver runs are not significantly different from the baseline. A graphical representation of these confidence intervals is included Figure 29.

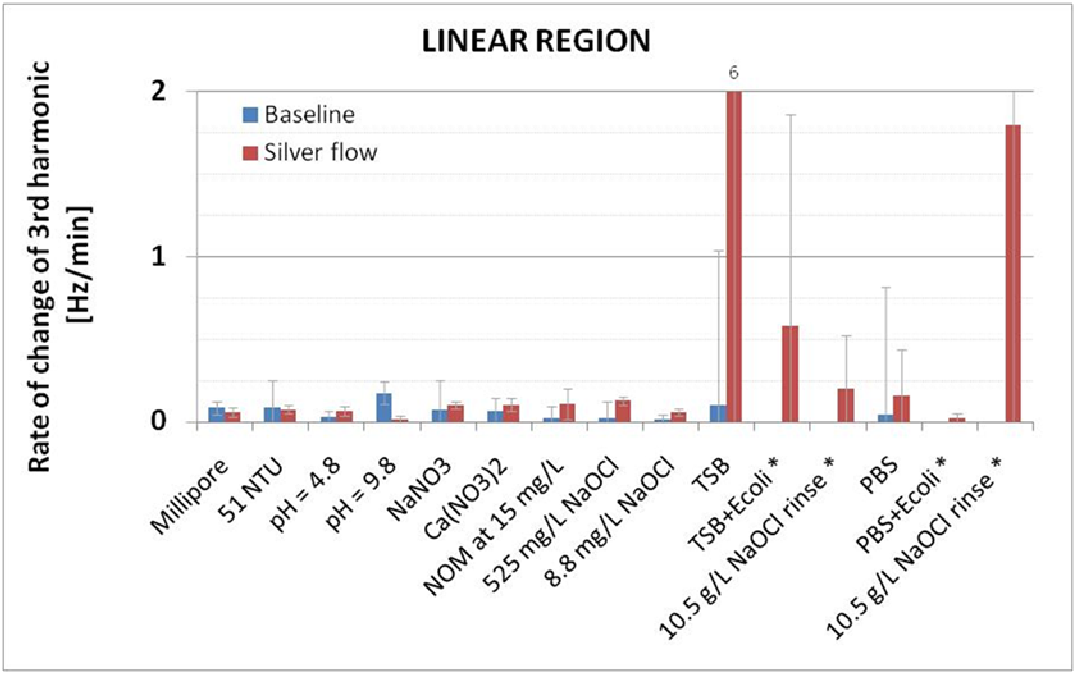

* - Experiment performed in sequence with previous data. Rate of change calculated from the previous plateau rather than from the minimum flow frequency.

Figure 29: Linear Region rate of change of the 3rd harmonic. Error bars represent 95% confidence interval. Mean values are included for data exceeding the axis maximum.

The implications of these overlapping data is that perhaps this measurement technique, employed under these experimental conditions, does not reveal real-time information of the rate of release of nanoparticles from the silica surface of the sensor. Looking at the p-values included in Table 15, the only significant increase of the 3rd harmonic rate of change from baseline to silver measurements was during the NaOCl experiments, and pH adjusted waters.

To ensure that assessment is correct, further statistical analysis was carried out to compare the slopes of the linear regions of data from both the baseline and silver flow experiments. A parallel line test was conducted on data sets in two steps: initially to ensure that the data from the four sensors run simultaneously was, in fact, statistically parallel to each other, and finally to compare the slopes of the silver flow data to the baseline data for each experimental set. The first test serves as a method to verify the appropriateness of grouping the data together for each experimental run. The second test determines whether the slope of the silver flow frequency response is statistically different from the baseline; that is, whether there is a detectable change in mass taking place at the surface of the sensor.

A parallel line test based on a simple linear model was used, where the hypothesis is that all lines being compared are parallel (slopes are equal). The null hypothesis is that at least one of the lines being compared is not parallel to the others. A calculation according to Equation 6 was performed for each experimental data set under both baseline and silver flow conditions. Once the W_P parameter is determined, it is compared to the F-value (a measure of linearity of a data set) for the known number of

Equation 6: Statistical analysis to determine parallel lines (Graybill 1976)

$$W_P = \frac{\sum_{h=1}^{N} \left[m_h - \frac{\sum_{i=1}^{N} m_i \cdot b_{ii}}{\sum_{j=1}^{N} b_{jj}} \right]^2 \cdot b_{hh}}{(N-1) \cdot \sigma^2}$$

where $$b_{hh} = \sum_{t=1}^{n_h} (x_{ht} - \overline{x_h})^2$$

m is the 3rd harmonic rate of change for each sensor
N is the total number of sensors being compared
n (lower case) is the total number of data points for each sensor
σ is the error of the linear regression
x represents each data point
x(bar) is the mean of the data set

degrees of freedom. If W_P is greater than or equal to that F-value, then the null hypothesis is rejected. In that case, the group of lines being compared may be considered parallel (Graybill 1976). The terms within Equation 6 account for the variance of each best fit line, as well as the slopes.

When comparing each grouping of data, this test proved that the lines are all parallel within the experimental data sets, meaning that the average slope for the four simultaneously run sensors is a justifiable quantity to consider. The slope for each of four sensors for the baseline flow under any one experimental condition is statistically the same as the slope for the other of those four sensors. Likewise, the same can be said for the slopes determined from the linear region of the silver flow analysis. A summary of the results of this statistical comparison may be found in Appendix E: Analysis.

Just as the complexity of the initial region of data pushed its interpretation beyond the scope of this investigation, the similarity of the slopes of the linear region prevents those results from providing real-time insight into the rate of release of silver from the silica surface. By comparing the slopes of the linear region for each silver flow experiment to the slopes of the baseline for that same water condition, it can be shown that there is not a statistically significant increase in the slope when predicted from a release of silver nanoparticles. Details of this comparison may also be found in Appendix E: Analysis.

Silver flow analysis summary

The analysis of the silver flow experiments as presented here is not sufficient to describe the effects of influent water quality on the release rate of silver from a silica surface. The results that prove to be most revealing are those that are taken from before and after the experimental flow runs. While that static information still provides valuable insight into the overall effects of the influent water quality, real-time detection of the release of silver nanoparticles was not possible.

Effluent Silver Concentration

Samples were collected during two of the experimental runs for silver content analysis by inductively coupled plasma with mass spectroscopy (ICP-MS). The two experiments that were selected for this analysis were the sample waters containing sodium hypochlorite, which clearly removed the majority of deposited silver.

The effluent stream was collected over one time interval during the experimental run of the influent concentration of 525 mg/L sodium hypochlorite. The effluent from all four of the sensors being run in parallel was collected as one sample, beginning 25 minutes after the flow contacted the sensor, through 50 minutes after initial flow. During that 25 minute interval, there were four effluent streams, each having a volumetric flow rate of 0.1 mL/min, yielding a sample volume of 10 mL.

Analysis was also conducted of the influent stream, to control for any silver contamination that may have been present. The influent stream was below the detection limit (BDL) of 0.011 ppm for the ICP-MS machine used for analysis.

As shown in Table 16, the average silver concentration for that 10 mL sample was 13 ppb. This implies that over that 25 minute interval, approximately 130 ng of silver were released into the water flowing across the sensors. That is a small fraction of the approximately 4 µg applied to the four sensors. One possible explanation is that the sodium hypochlorite had the immediate effect of removing the vast majority of the deposited silver. In that case, the effluent stream 25 minutes after flow began would have nothing more than trace amounts of silver, such as this case.

Table 16: Silver content analysis of NaOCl-containing samples

Sample Water	Description	Silver content (ppb)
525 mg/L NaOCl	Influent	(< 11)
	Effluent, collected from 25 to 50 minutes	13
8.8 mg/L NaOCl	Influent	(< 11)
	Effluent collected from 0 to 10 minutes	97
	Effluent, collected from 25 to 50 minutes	15

For the experimental run conducted at 8.8 mg/L sodium hypochlorite, two samples were collected: one was collected during the initial 10 minutes of flow, and the second was collected over the same time interval as the previous run, from 25 to 50 minutes after flow began. Again in this case, the silver concentration of the influent water was below the detection limit of the ICP-MS.

The second sample matched quite well with the sample collected over the same time interval for the higher sodium hypochlorite influent concentration. In this case, at 8.8 mg/L influent concentration of sodium hypochlorite, the measured concentration was 15 ppb, suggesting that a total of 150 ng of silver was released during that time interval.

If those silver concentrations are exceptionally low because the proposed action of immediate stripping of the silver occurs, then one would expect a sample taken at the commencement of the flow run to contain a higher concentration of silver, corresponding with a total mass approaching the 3.5 µg of silver deposited onto the four sensors, as calculated from deposition of a known volume of the application solution (at 175-190 ppm silver). Such is not the case.

The sample collected from time zero through 10 minutes of the experimental run provided a sample volume of 4 mL. According to ICP-MS analysis, the silver content of that sample was 97 ppb. It follows that in those first 10 minutes of flow, a total mass of silver equal to around 390 ng was picked up by the water flowing across the sensors.

That mass of silver is still surprisingly low given the overall effect of the sodium hypochlorite containing waters. As an exercise, to consider that concentration as being stable for 1 full hour, the total amount of silver in the effluent stream would still only be around 1.6 µg of silver. That would be less than half of the silver deposited! And in actuality, that concentration is only occurring for the first few minutes, with a rapid decrease down to approximately 15 ppb.

Further experiments will be required to fully understand what is happening to the mass of silver that is unaccounted for. At the time of experimentation, the tubing and sensor holder were not expected to dramatically affect the silver concentration by sorption to any surfaces, but perhaps sorption would explain the very low concentration of silver measured in the effluent stream. For reference, the tubing leading out of the titanium flow channels of the sensor holder was 18 inches long PTFE tubing, to which a 12 inch length of Tygon tubing for the peristaltic pump was attached, both had internal diameters on the order of 0.5 mm. The effluent stream was collected into a polyethylene vial, refrigerated immediately, and tested by ICP-MS within 72 hours of collection. The sample was not acidified due to the suspension characteristics of the casein-coated silver nanoparticles, as well as the limited time between collection and testing.

It is interesting that the silver concentrations of these effluent waters correlate well with what has been measured during full-scale ceramic pot filter testing. It is common for the first few flushings to have silver concentrations around, or slightly greater than, 50 ppb (Lantagne 2001; Bielefeldt et al. 2009). The silver releasing from the ceramic surface rapidly declines, reaching a near equilibrium level of approximately 10 ppb within the first 10 flushings (Bielefeldt et al. 2009; Kohler 2009). There are too many other factors at play in these measurements to compare those concentrations directly to the QCM experiments, but it is at the very least encouraging that the trend is similar.

Perhaps with more fundamental investigations into the effects being detected by the QCM, this real-time gravimetric technique could still be applied to a condition representative of nanoparticle silver being released from a ceramic surface. At this time, though, the real-time data is not useful for that assessment. Instead, the most significant results are those obtained from simple before and after measurements.

Conclusions

The results presented in this document provide a glimpse of a colloidal silver product used worldwide in ceramic pot filter production. The colloidal silver solution was characterized through elemental analysis and particle size distribution, showing that the silver product contained few contaminants and consisted of mostly spherical nanoparticles with an average diameter on the order of 10-50 nanometers. The silver concentration of the application solution was measured to be 70 percent of the mass of silver powder added, due to the inclusion of a high ratio of casein to aid in suspension.

A novel gravimetric technique was employed to determine the effects of varied water quality parameters on the rate of release of that silver nanoparticle, once applied to a silica surface. The results of this study show that the pH, ionic strength, and turbidity, when at environmentally relevant concentrations, have little impact on the rate of silver release. While those results were not discernible during the actual experimental flow runs, the measurements taken after the flow run portray minimal effects.

Even though the results do not show any significant trends between the sample waters tested, a valuable piece of information was still gained – that the influent water quality should not greatly impact the rate of release of the colloidal silver coating from the walls of the ceramic pot filter. It is worth noting that the preliminary experiments did show exceptionally high rates of silver release when the influent waters contained high concentrations of organic components (e.g, TSB) and bacteria. This could cause concern if direct contamination of source water by latrine discharge or seepage is a possibility.

On the other hand, water containing even very low concentrations of sodium hypochlorite has the effect of removing almost all of the silver from the silica surface. As presented in the results section, waters at 8.8 mg/L NaOCl removed at least 90 percent of the adsorbed silver. That is an important fact to know for the use of these ceramic pot filters.

The concentration of 8.8 mg/L NaOCl was selected based on guidelines provided by the World Health Organization (WHO) and the US Environmental Protection Agency (EPA) for drinking water purification by addition of household bleach. This concentration of sodium hypochlorite is a potential influent stream into a ceramic pot filter in areas where inconsistent municipal drinking water treatment may be provided, or where community members have been instructed to also treat their water with a few drops of bleach per liter (which is a distinct possibility given the often overlapping efforts of aid organizations and NGO's in developing regions).

Based on these experiments, it is clear that pouring water containing NaOCl into a ceramic pot filter would quickly remove the silver coating. There are at least two negative effects caused by this, including the increased silver concentration being ingested by the end-user and the decreased effectiveness of the water filter due to the removal of the anti-microbial coating.

It is extremely important that users do not clean their ceramic pot filters with water containing bleach. This could be a difficult message to deliver, as it may seemingly be in contrast to the very important procedure of cleaning the receptacle and spigot with a cleaning solution, often containing sodium hypochlorite from bleach. However, as seen by data presented here, that bleach containing water should not come in contact with the silver coated ceramic filter element.

Future Work

While real-time monitoring of the release of silver nanoparticles may be difficult to achieve, there are still a number of steps that could be taken to build on the results presented here, and to improve the overall understanding of the colloidal silver coating at use in tens of thousands of ceramic pot filters worldwide. Some potential directions for future investigations include:

- Determine the source of discrepancy between the expected frequency shift and the actual frequency shift for both adsorbed and sputtered silver.
- Improve application techniques to allow for more reliable prediction of frequency shifts caused by deposited silver.
- Increase the mass of silver deposited onto each sensor, potentially allowing for a larger and more detectable shift in frequency.
- Increase the duration of flow tests and analyze each for effluent silver concentration.
- Determine the fate of silver nanoparticles released from the sensor surface within the experimental set-up.
- Understand the “deposition”-type effects caused by influent waters containing nitrate salts.
- Find trends between hypochlorite concentrations, dissolved oxygen content of the water, and the rate of release of silver nanoparticles from the ceramic surface.
- More accurately represent the alumino-silicate composition of the ceramic pot filters on the surface of the QCM sensors.
- Define the mechanisms of association between the silver nanoparticles and the ceramic substrate (whether silica or alumino-silicate).
- Determine the effects of varied ceramic microstructures (porosity, elemental composition, surface chemistry) on the rate of release of silver nanoparticles under relevant flow conditions.
- Use these data to better predict the operational lifetime of the colloidal silver coating.
- Use these data to optimize the application procedures for the colloidal silver coating in a manner that is appropriate for actual production facilities.

References

Aitken RJ, Creely KS, Tran CL (2004). "Nanoparticles: An Occupational Hygiene Review." Research Report 274. *Institute of Occupational Medicine, Health and Safety Executive*. Crown. Norwich, UK.

Archer SL (2008). "Dilated cardiomyopathy and left bundle branch block associated with ingestion of colloidal gold and silver is reversed by British antiLewisite and vitamin E: The potential toxicity of metals used as health supplements." *Canadian Journal of Cardiology* 24 (5): 397-399.

Auffan M, Rose J, Bottero JY, Lowry GV, Jolivet JP, Wiesner MR (2009) "Towards a definition of inorganic nanoparticles from an environmental, health and safety perspective." *Nature Nanotechnology* 4 (10): 634-41.

el Badawy AM, Luxton TP, Silva RG, Scheckel KG, Suidan MT, Tolaymat TM (2010). "Impact of Environmental Conditions (pH, Ionic Strength, and Electrolyte Type) on the Surface Charge and Aggregation of Silver Nanoparticles Suspensions." *Environmental Science & Technology* 44: 1260-1266.

Benjamin MM (2002). Water Chemistry. International Edition. McGraw Hill, Singapore.

Bielefeldt AR, Kowalski K, Summers RS (2009). "Bacterial treatment effectiveness of point-of-use ceramic water filters." *Water Research* 43: 3559-3565.

Bielefeldt AR, Kowalski K, Schilling C, Schreir S, Kohler A, Summers RS (2010). "Removal of virus to protozoan sized particles in point-of-use ceramic water filters." *Water Research* 44: 1482-1488.

Brandt D, Park B, Hoang M, Jacobe HT (2005). "Argyria secondary to ingestion of homemade silver solution." *Journal of the American Academy of Dermatology* 53 (2 Suppl 1): S105-S107.

Brauner CJ, Wilson J, Kamunde C, Wood CM (2003). "Water Chloride Provides Partial Protection during Chronic Exposure to Waterborne Silver in Rainbow Trout (Oncorhynchus mykiss) Embryos and Larvae." *Physiological and Biochemical Zoology* 76 (6): 803-815.

Buttry DA, Ward MD (1992). "Measurement of Interfacial Processes at Electrode Surfaces with the Electrochemical Quartz Crystal Microbalance." *Chemical Reviews* 92: 1355-1379.

Cho NJ, Frank CW, Kasemo B, Hook F (2010). "Quartz crystal microbalance with dissipation monitoring of supported lipid bilayers on various substrates." *Nature Protocols* 5 (6): 1096-1106.

Cientifica Ltd (2009). "Global Nanotechnology Funding in 2009". (accessed July 2010 at http://cientifica.eu/attachments/050_Nanotechnology Takes a Deep Breath.pdf)

Clasen TF (2009). "Scaling Up Household Water Treatment Among Low-Income Populations." World Health Organization. Geneva, Switzerland.

CMWG - The Ceramics Manufacturing Working Group (2010). "Best Practice Recommendations for Local Manufacturing of Ceramic Filters for Water Treatment", Ed. 1. Atlanta, GA, USA.

Cosgrove T, editor (2010). Colloid Science: Principles, Methods and Applications. 2nd edition. John Wiley & Sons, West Sussex, UK.

Diegoli S, Manciulea AL, Begum S, Jones IP, Lead JR, Preece JA (2008). "Interactions of charge stabilised gold nanoparticles with organic macromolecules." *Science of the Total Environment* 402: 51-61.

Doulton Ceramic Water Filters. "Silver – Nature's Water Purifier". Undated. (accessed July 2010 at http://www.doulton.ca/silver.html)

Drozd C, Schwartzbrod J (1996). "Hydrophobic and Electrostatic Cell Surface Properties of *Cryptosporidium Parvum*." *Applied and Environmental Microbiology* 62 (4): 1227-1232.

ENG - European Nanotechnology Gateway (2005). Funding and support for international nanotechnology collaborations. (accessed July 2010 at www.nanoforum.org)

Geranio L, Heuberger M, Nowack B (2009). "The Behavior of Silver Nanotextiles during Washing." *Environmental Science & Technology* 43: 813-818.

Graybill FA (1976). Theory and Application of the Linear Model. Duxbury Press. N Scituate, MA. 288-289.

Gustafsson O, Gschwend PM (1997). "Aquatic Colloids: Concepts, Definitions, and Current Challenges." *Limnology and Oceanography* 42 (3): 519-528.

Hagan JM, Harley N, Pointing D, Sampson M, Smith K, Soam V (2009). "Resource Development International – Cambodia: Ceramic Water Filter Handbook." Version 1.1. Phnom Penh, Cambodia.

Hoek EMV, Bhattacharjee S, Elimelech M (2003). "Effect of Membrane Surface Roughness on Colloid-Membrane DLVO Interactions." *Langmuir* 19: 4836-4847.

Hook F (1997). "Development of a novel QCM technique for protein adsorption studies." Dissertation. Chalmers University of Technology and Goteborg University.

Hook F, Rodahl M, Brzezinski P, Kasemo B (1998). "Energy dissipation kinetics for protein and antibody-antigen adsorption under shear oscillation on a quartz crystal microbalance." *Langmuir* 14: 729-734.

Hospitality Trends (2010). Nanotechnology Market Forecast to 2013. (accessible at www.htrends.com)

Hussain SM, Hess KL, Gearhart JM, Geiss KT, Schlager JJ (2005). "In vitro toxicity of nanoparticles in BRL 3A rat liver cells." *Toxicology in Vitro* 19: 975-983.

Jaiswal A (2010). "Introduction to Data Analysis." Presentation for QCM-D Basic Training Course, Q-sense. 23-24 February 2010.

Jara AA, Goldberg S, Mora ML (2005). "Studies of the surface charge of amorphous aluminosilicates using surface complexation models." *Journal of Colloid and Interface Science* 292: 160-170.

Jordan W (2010). "Nanotechnology and Pesticides." Presentation to the Pesticide Program Dialogue Committee, Office of Pesticide Programs, USEPA; Session I. 29 April 2010.

Ju-Nam Y, Lead JR (2008). "Manufactured Nanoparticles: An overview of their chemistry, interactions and potential environmental implications." *Science of the Total Environment* 400: 396-414.

Kanazawa KK, Gordon JG II (1985). "Frequency of a Quartz Crystal Microbalance in Contact with Liquid." *Analytical Chemistry* 57: 1771-1772.

Klarman M (2009). "Investigation of Ceramic Pot Filter Design Variables." Thesis. Emory University.

Kohler AM (2009). "Bacterial Disinfection and Contamination of Drinking Water by Ceramic Pot Filter Cores." Thesis. University of Colorado.

Lantagne D (2001). "Investigation of the Potters for Peace Colloidal Silver Impregnated Ceramic Filter – Report 1: Intrinsic Effectiveness." Alethia Environmental. Allston, MA.

Lu CS (1975). "Mass determination with piezoelectric quartz crystal resonators." *Journal of Vacuum Science & Technology* 12 (1): 578-583.

Lu CS, Lewis O (1972). "Investigation of film thickness determination by oscillating quartz resonators with large mass load." *Journal of Applied Physics* 43 (11): 4385-4390.

Lu F, Lee HP, Lim SP (2004). "Quartz crystal microbalance with rigid mass partially attached on electrode surfaces." *Sensors and Actuators A* 112: 203-210.

Luoma SN (2008). "Silver Nanotechnologies and the Environment: Old Problems or New Challenges?" Project on Emerging Nanotechnologies (PEN15). Washington, DC.

Lux Research (2007). The Nanotech Report, 5th Edition. (accessible at www.luxresearchinc.com)

Madou MJ (1997). Fundamentals of microfabrication. CRC Press, Boca Raton, FL. 99-102.

Martin SJ, Granstaff VE, Frye GC (1991). "Characterization of a Quartz Crystal Microbalance with Simultaneous Mass and Liquid Loading." *Analytical Chemistry* 63: 2272-2281.

McAllister S (2005). "Analysis and Comparison of Sustainable Water Filters." EPD 397 Technical Report, Undergraduate Engineering Review, Department of Mechanical Engineering. University of Wisconsin – Madison.

Morones JR, Elechiguerra JL, Camacho A, Holt K, Kouri JB, Ramirez JT, Yacaman MJ (2005). "The bactericidal effect of silver nanoparticles." *Nanotechnology* 16: 2346-2353.

Mould RF (2007). "Pierre Curie, 1859-1906." *Current Oncology* 14 (2): 74-82.

Nardo R (2005). "Factory Startup Manual: For The Production of Ceramic Water Filters." (accessed July 2010 at http://s189535770.onlinehome.us/pottersforpeace/?page_id=125)

Navarro E, Piccapietra F, Wagner B, Marconi F, Kaegi R, Odzak N, Sigg L, Behra R (2008). "Toxicology of Silver Nanoparticles to *Chlamydomonas reinhardtii*." *Environmental Science & Technology* 42: 8959-8964.

Nowack B, Bucheli TD (2007). "Occurrence, behavior and effects of nanoparticles in the environment." *Environmental Pollution* 150: 5-22.

NSF - National Science Foundation (2001). Nanoscale Science, Engineering, and Technology Workshop Report: Societal Implications of Nanoscience and Nanotechnology.

NSTC - National Science and Technology Council (2010). The National Nanotechnology Initiative: Supplement to the President's 2011 Budget.

O'Sullivan CK, Guilbault GG (1999). "Commercial quartz crystal microbalances – theory and applications." *Biosensors & Bioelectronics* 14: 663-670.

Oyanedel-Craver VA, Smith J (2008) "Sustainable Colloidal-Silver-Impregnated Ceramic Filter for Point-of-Use Water Treatment." *Environmental Science & Technology* 42: 927-933.

PCAST - President's Council of Advisors on Science and Technology (2010). Report to the President and Congress on the Third Assessment of the National Nanotechnology Initiative. 12 March 2010.

PEN - Project on Emerging Nanotechnologies, Woodrow Wilson International Center for Scholars and PEW Charitable Trusts (2009). "Analysis of Consumer Product Inventory." (accessed July 2010 at http://www.nanotechproject.org/inventories/consumer/analysis_draft/)

PFP - Potters for Peace. "Promoting Clean Water through Local Partnerships: An Innovative Approach." Undated. (accessed July 2010 at http://s189535770.onlinehome.us/pottersforpeace/wp-content/uploads/filter-work.pdf)

Poitras C, Fatisson J, Tufenkji N (2009). "Real-time microgravimetric quantification of *Cryptosporidium parvum* in the presence of potential interferents." *Water Research* 43: 2631-2638.

Quevedo IR, Tufenkji N (2009). "Influence of Solution Chemistry on the Deposition and Detachment Kinetics of a CdTe Quantum Dot Examined Using a Quartz Crystal Microbalance." *Environmental Science & Technology* 43: 3176-3182.

Rayner J (2009). "Current Practices in Manufacturing of Ceramic Pot Filters for Water Treatment." Thesis. Loughborough University.

Rechendorff K, Hovgaard MB, Foss M, Besenbacher F (2007). "Influence of surface roughness on quartz crystal microbalance measurements in liquids." *Journal of Applied Physics* 101 (114502). DOI: 10.1063/1.2735399.

Roco MC (2002). "Government Nanotechnology Funding: An International Outlook." *JOM Journal of the Minerals, Metals and Materials Society* 54 (9): 22-23.

Rodahl M (1995a). "On the Frequency and Q Factor Response of the Quartz Crystal Microbalance to Liquid Overlayers." Dissertation. Chalmers University of Technology and Goteborg University.

Rodahl M, Hook F, Krozer A, Brzezinski P, Kasemo B (1995b). "Quartz crystal microbalance setup for frequency and Q-factor measurements in gaseous and liquid environments." *Review of Scientific Instruments* 66 (7): 3924-3930.

Rojas E, Gallego M, Reviakine I (2008). "Effect of Sample Heterogeneity on the Interpretation of Quartz Crystal Microbalance Data: Impurity Effects." *Analytical Chemistry* 80: 8982-8990.

Russell P, Batchelor D, Thornton JT (2004). "SEM and AFM: Complementary Techniques for High Resolution Surface Investigations." Veeco Instruments and North Carolina State University. Santa Barbara, CA and Raleigh, NC.

Ryan JN, Gschwend PM (1994). "Effects of Ionic Strength and Flow Rate on Colloid Release: Relating Kinetics to Intersurface Potential Energy." *Journal of Colloid and Interface* Science 164: 21-34.

Sauerbrey G (1959). "Verwendung von Schwingquarzen zur Wagung dunner Schicten und zur Mikrowagung." *Zeitschrift fur Physik* 155: 206-222.

Silvestry-Rodriguez N, Sicairos-Ruelas EE, Gerba CP, Bright KR (2007). "Silver as a Disinfectant." *Reviews of Environmental Contamination & Toxicology* 191: 23-45.

Sobsey MD, Stauber CE, Casanova LM, Brown JM, Elliott MA (2008). "Point of Use Household Drinking Water Filtration: A Practical, Effective Solution for Providing Sustained Access to Safe Drinking Water in the Developing World." *Environmental Science & Technology* 42: 4261-4267.

SRS - Stanford Research Systems (2005). "Operation and Service Manual: QCM200 Quartz Crystal Microbalance Digital Controller." Revision 2.1. Sunnyvale, CA.

Stone V, project coordinator (2009). "Engineered Nanoparticles: Review of Health and Environmental Safety." Edinburgh Napier University. Edinburgh, UK.

Sung JH, Ji JH, Yoon JU, Kim DS, Song MY, Jeong J, Han BS, Han JH, Chung YH, Kim J, Kim TS, Chang HK, Lee EJ, Lee JH, Yu IJ (2008). "Lung function changes in Sprague-Dawley rats after prolonged inhalation exposure to silver nanoparticles." *Inhalation Toxicology* 20 (6): 567-574.

UNDP - United Nations Development Programme (c2004). "Filtrón: Ceramic Filter for Drinking Water." Innovation for Development and South-South Cooperation. Nicaragua. (accessed July 2010 at http://pottersforpeace.org/ wp-content/uploads/ideass-brochure-english.pdf)

USEPA Office of Water (2006). "Emergency Disinfection of Drinking Water." EPA 816-F-06-027. (accessed July 2010 at www.epa.gov/safewater)

USEPA Science Policy Council, Nanotechnology Workgroup (2007). US Environmental Protection Agency Nanotechnology White Paper.

van Halem D (2006). "Ceramic Silver Impregnated Pot Filters for Household Drinking Water Treatment in Developing Countries." Thesis. Delft University of Technology. Delft, Netherlands.

Voinova MV, Rodahl M, Jonson M, Kasemo B (1999). "Viscoelastic Acoustic Response of Layered Polymer Films at Fluid-Solid Interfaces: Continuum Mechanics Approach." *Physica Scripta* 59: 391-396.

Vrijenhoek EM, Hong S, Elimelech M (2001). "Influence of membrane surface properties on initial rate of colloidal fouling of reverse osmosis and nanofiltration membranes." *Journal of Membrane Science* 188: 115-128.

Ward MD, Buttry DA (1990). "In Situ Interfacial Mass Detection with Piezoelectric Transducers." *Science* 249: 1000-1007.

WHO - World Health Organization (2004). "Guidelines for Drinking Water Quality." 3rd Edition, Volume 1. Geneva, Switzerland.

Wright H, Bielefeldt AR (2005). "Evaluating the Water Treatment Effectiveness of the Filtrón." Presented at the University of Colorado, Boulder. (unpublished)

Index of Appendices

Appendix A: SEM Images

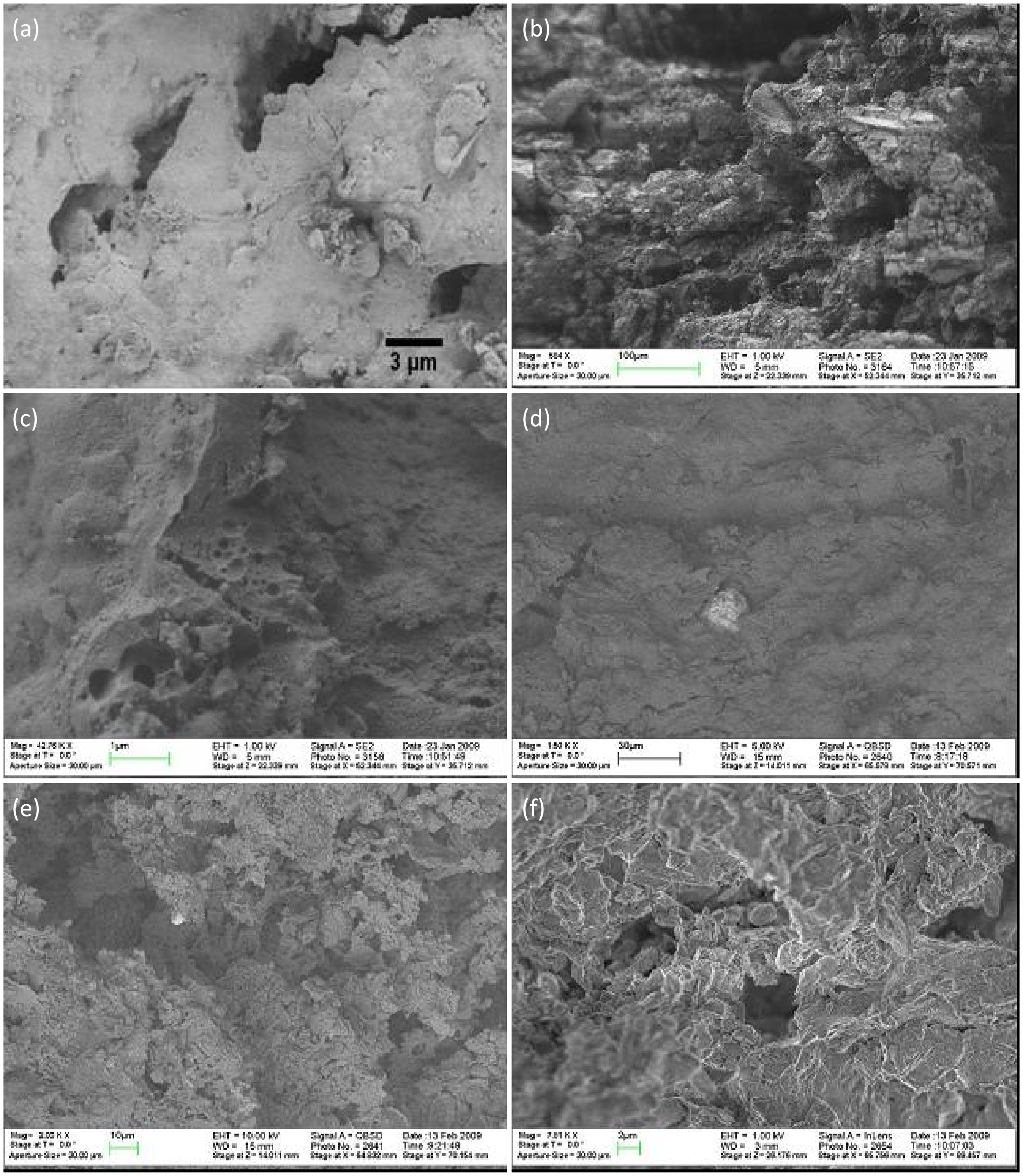

Figure A-1: SEM images of inner wall of used Nicaraguan filter by Secondary Electron Detector (a); mid-wall of used Nicaraguan filter by Secondary Electron Detector (b, c); outer wall of used Nicaraguan filter by Backscatter Electron Detector (d, e); mid-wall of new Peruvian filter by In-Lens Detector (f). Scale bars shown represent: (a) 3 µm, (b) 100 µm, (c) 1 µm, (d) 30 µm, (e) 10 µm and (f) 2 µm.

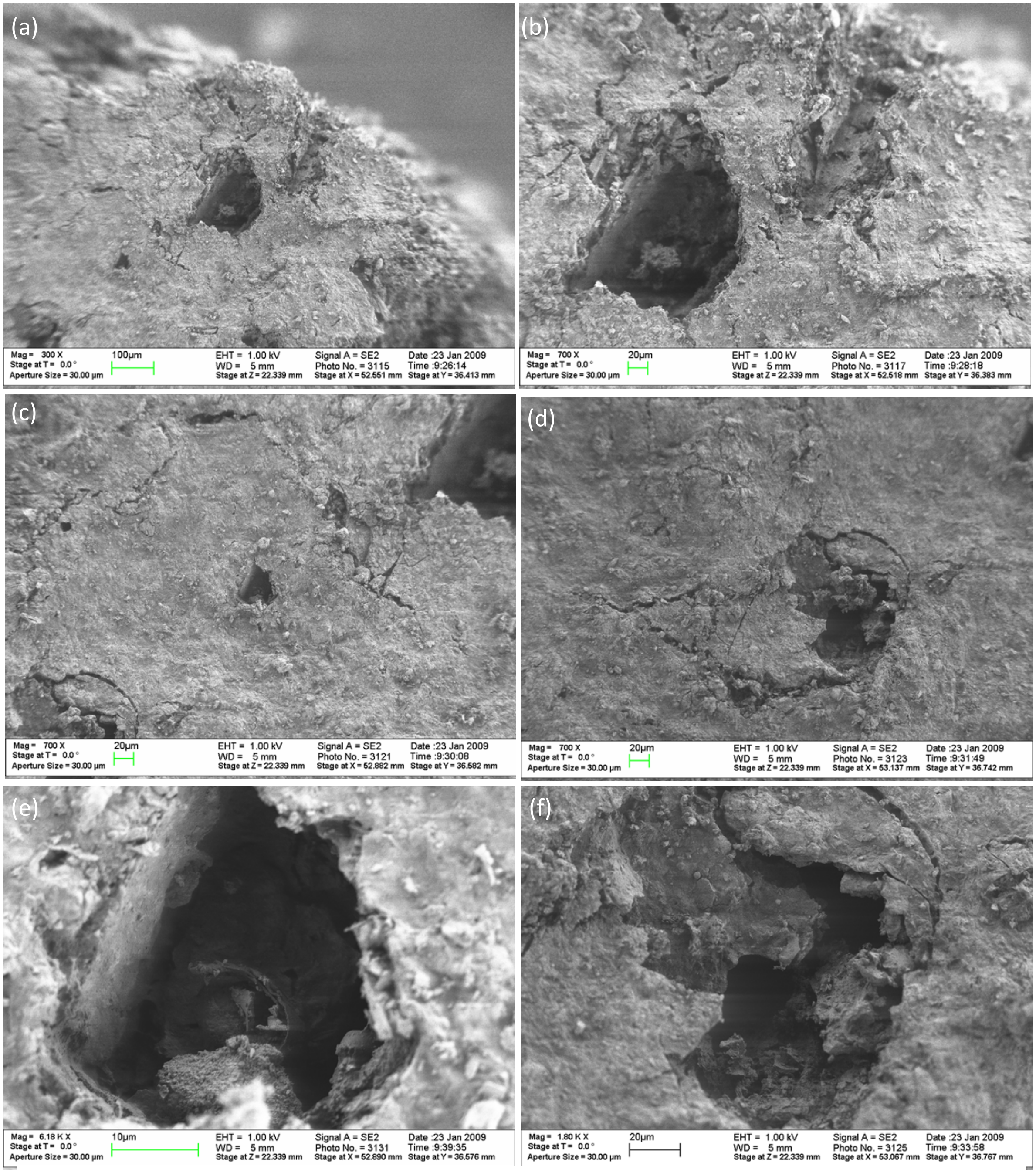

Figure A-2: SEM images of inner wall of used Nicaraguan filter by Secondary Electron Detector (a, b, c, d, e, f). Image (b) is a zoom of (a), (e) is a zoom of (c), and (f) is a zoom of (d). Scale bars shown represent: (a) 100 µm, (b) 20 µm, (c) 20 µm, (d) 20 µm, (e) 10 µm and (f) 20 µm.

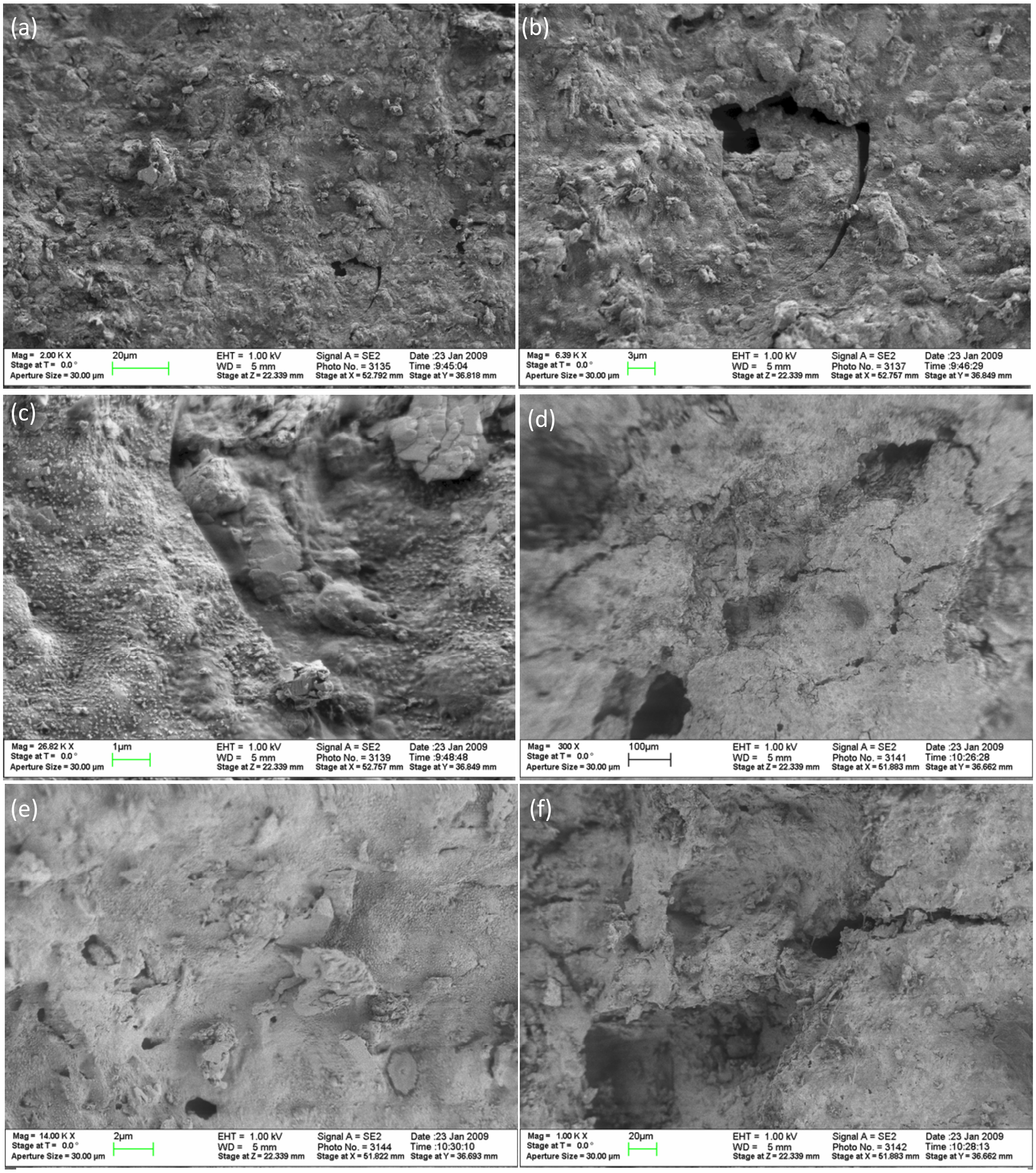

Figure A-3: SEM images of inner wall of used Nicaraguan filter by Secondary Electron Detector (a, b, c, d, e, f). Scale bars shown represent: (a) 20 µm, (b) 3 µm, (c) 1 µm, (d) 100 µm, (e) 2 µm and (f) 20 µm.

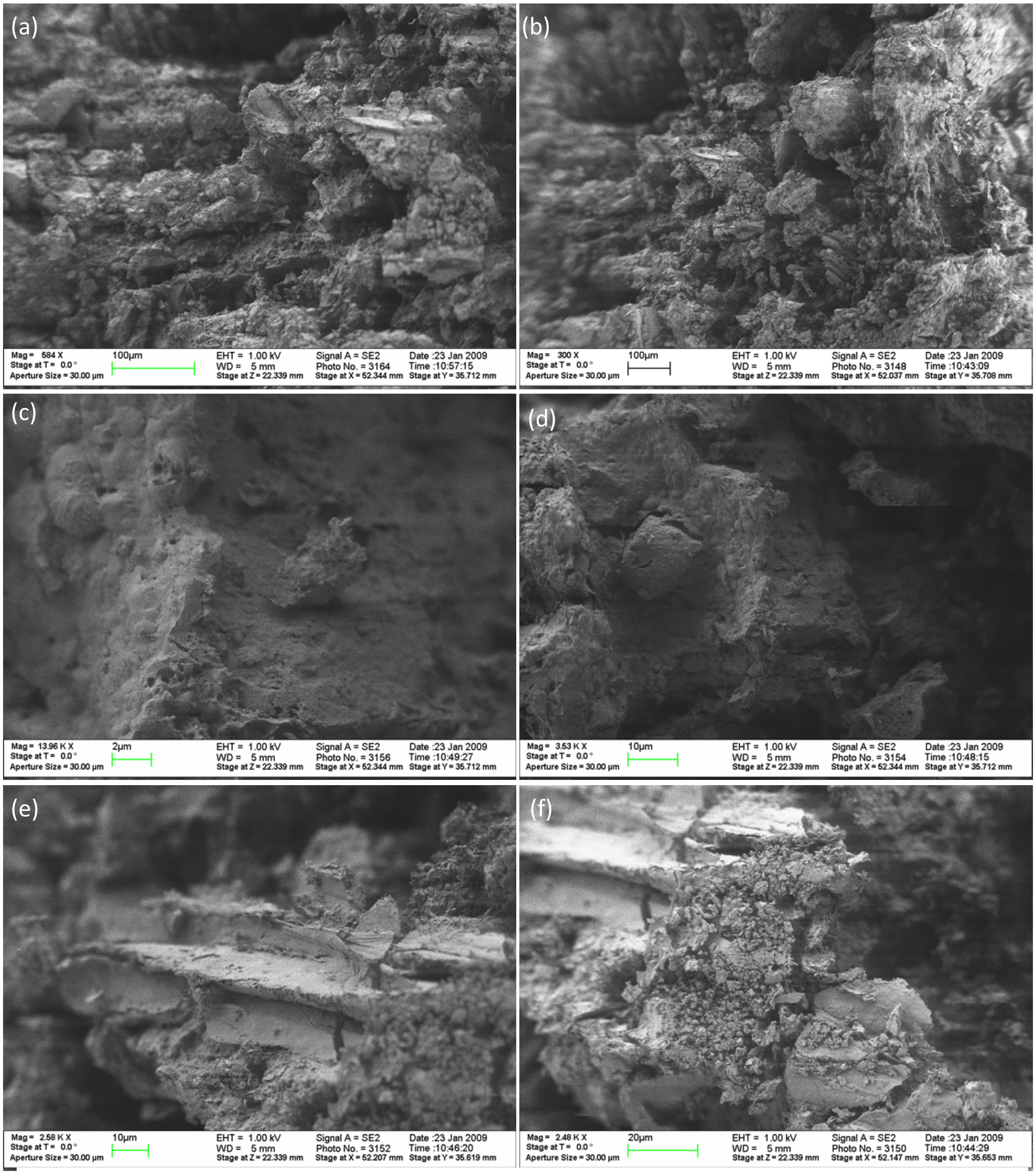

Figure A-4: SEM images of mid-wall of used Nicaraguan filter by Secondary Electron Detector (a, b, c, d, e, f). Scale bars shown represent: (a) 100 µm, (b) 100 µm, (c) 2 µm, (d) 10 µm, (e) 10 µm and (f) 20 µm.

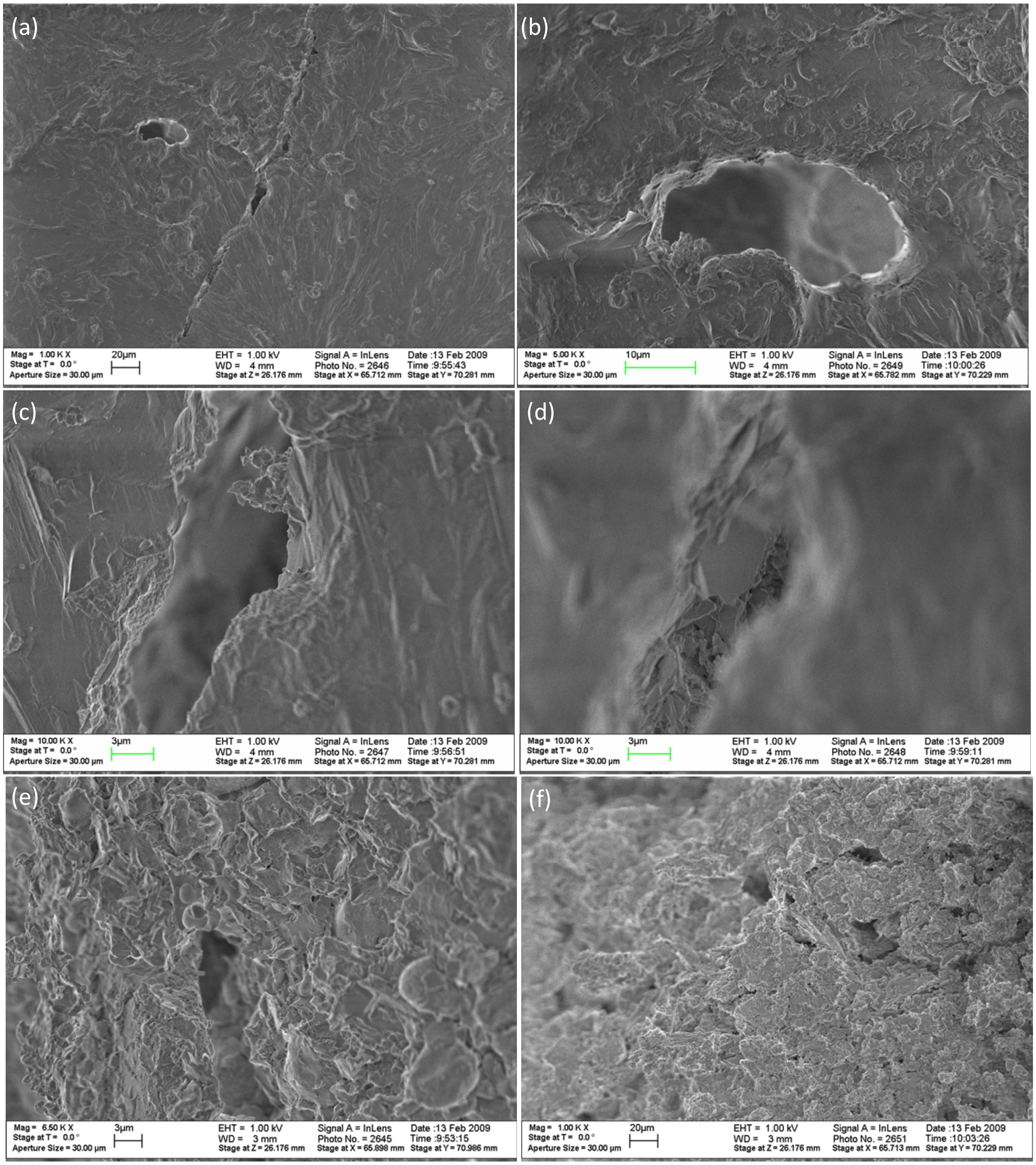

Figure A-5: SEM images of outer-wall (a, b, c, d); of a specimen taken 2.5 mm within the inner wall (close to the mid-wall) (e); and of the mid wall (f) of a new Peruvian filter by an In Lens Detector. The features seen in (b, c, d) are all evident in image (a). Image (c) is identical to (d) but at a different focal distance. Scale bars shown represent: (a) 20 µm, (b) 10 µm, (c) 3 µm, (d) 3 µm, (e) 3 µm and (f) 20 µm.

Appendix B: Theoretical QCM Response to Water

Appendix B.1: Water Density and Viscosity Values

Temp	**Density**	**Dynamic Viscosity (μ --or-- η)**	
(℃)	(kg/m3)	(Pa-sec)	(g/(cm-sec))
20.0	998.23	1.00E-03	0.010
20.1	998.21	9.99E-04	0.010
20.2	998.19	9.97E-04	0.010
20.3	998.17	9.94E-04	0.010
20.4	998.15	9.92E-04	0.010
20.5	998.13	9.90E-04	0.010
20.6	998.11	9.87E-04	0.010
20.7	998.09	9.85E-04	0.010
20.8	998.07	9.83E-04	0.010
20.9	998.04	9.80E-04	0.010
21.0	998.02	9.78E-04	0.010
21.1	998.00	9.75E-04	0.010
21.2	997.98	9.73E-04	0.010
21.3	997.96	9.71E-04	0.010
21.4	997.93	9.69E-04	0.010
21.5	997.91	9.66E-04	0.010
21.6	997.89	9.64E-04	0.010
21.7	997.87	9.62E-04	0.010
21.8	997.85	9.59E-04	0.010
21.9	997.82	9.57E-04	0.010
22.0	997.80	9.55E-04	0.010
22.1	997.78	9.53E-04	0.010
22.2	997.75	9.50E-04	0.010
22.3	997.73	9.48E-04	0.009
22.4	997.71	9.46E-04	0.009
22.5	997.69	9.44E-04	0.009
22.6	997.66	9.41E-04	0.009
22.7	997.64	9.39E-04	0.009
22.8	997.62	9.37E-04	0.009
22.9	997.59	9.35E-04	0.009
23.0	997.57	9.33E-04	0.009
23.1	997.54	9.30E-04	0.009
23.2	997.52	9.28E-04	0.009
23.3	997.50	9.26E-04	0.009
23.4	997.47	9.24E-04	0.009
23.5	997.45	9.22E-04	0.009
23.6	997.42	9.20E-04	0.009
23.7	997.40	9.17E-04	0.009
23.8	997.38	9.15E-04	0.009
23.9	997.35	9.13E-04	0.009
24.0	997.33	9.11E-04	0.009
24.1	997.30	9.09E-04	0.009
24.2	997.28	9.07E-04	0.009
24.3	997.25	9.05E-04	0.009
24.4	997.23	9.03E-04	0.009
24.5	997.20	9.01E-04	0.009
24.6	997.18	8.99E-04	0.009
24.7	997.15	8.97E-04	0.009
24.8	997.13	8.95E-04	0.009
24.9	997.10	8.92E-04	0.009
25.0	997.08	8.90E-04	0.009

Appendix B.2: Frequency and Resistance Response by QCM to Water

All values shown for 1st harmonic ($f_0 = 5$ MHz). Other harmonic responses may be calculated similarly.

T (°C)	Kanazawa Δ f (Hz)	Martin Δ R (Ω)
20.0	-715	377
20.5	-711	375
21.0	-706	373
21.5	-702	371
22.0	-698	368
22.5	-694	366
23.0	-690	364
23.5	-685	362
24.0	-681	360
24.5	-678	358
25.0	-674	356

$$\Delta R = \left(\frac{n\omega_s L_u}{\pi}\right)\cdot\left(\frac{2\omega_s \rho_L \eta_L}{\rho_q \mu_q}\right)^{1/2}$$

$$\Delta f = -f_U^{3/2}\left(\frac{\rho_L \eta_L}{\pi \rho_q \mu_q}\right)^{1/2}$$

f_0 = 5000000 Hz

T_0 = 20 deg C

Δ T = 0.5 deg C/min

ωs = 3.14E+07 rad/sec

Lu = 42 mH

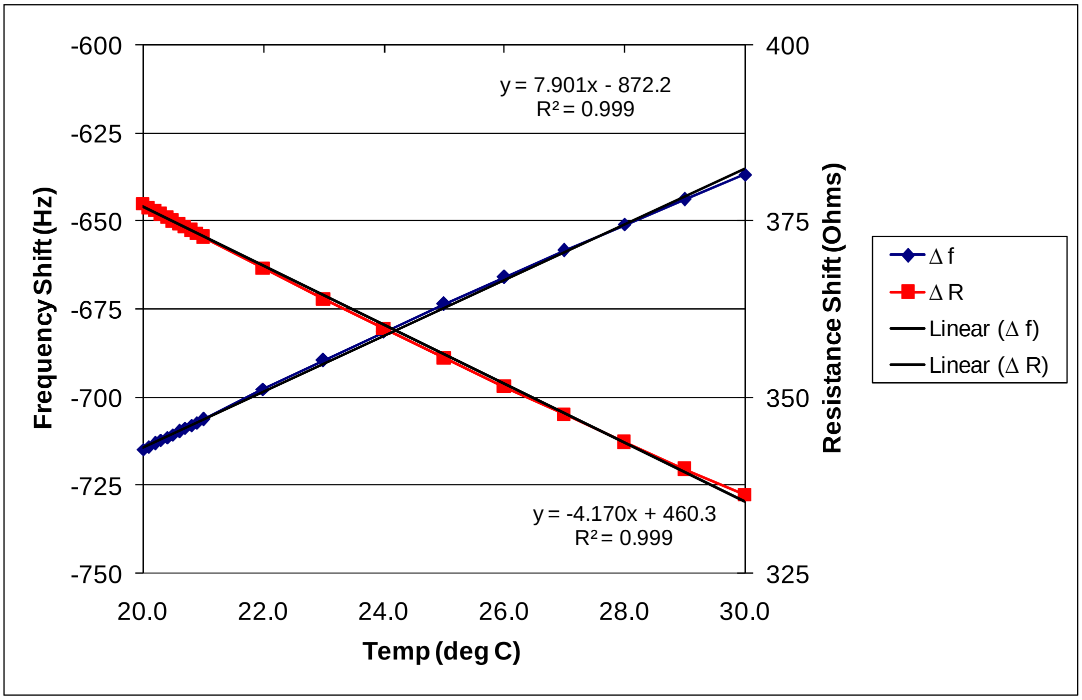

Appendix C: Materials and Methods

Appendix C.1: Silver Collargol Data, Laboratorios Argenol

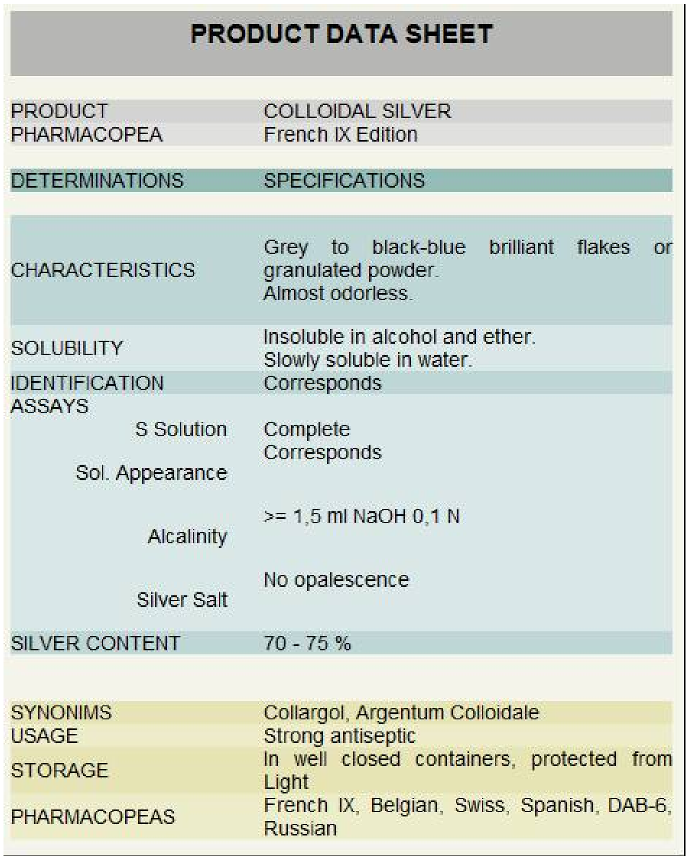

PRODUCT DATA SHEET

PRODUCT	COLLOIDAL SILVER
PHARMACOPEA	French IX Edition
DETERMINATIONS	SPECIFICATIONS
CHARACTERISTICS	Grey to black-blue brilliant flakes or granulated powder. Almost odorless.
SOLUBILITY	Insoluble in alcohol and ether. Slowly soluble in water.
IDENTIFICATION	Corresponds
ASSAYS	
S Solution	Complete
Sol. Appearance	Corresponds
Alcalinity	>= 1,5 ml NaOH 0,1 N
Silver Salt	No opalescence
SILVER CONTENT	70 - 75 %
SYNONIMS	Collargol, Argentum Colloidale
USAGE	Strong antiseptic
STORAGE	In well closed containers, protected from Light
PHARMACOPEAS	French IX, Belgian, Swiss, Spanish, DAB-6, Russian

(from http://www.laboratorios-argenol.com/fi-colargoli.htm, accessed July 2010)

REPORT OF TEM OF COLARGOL

NOTE: Original document entitled "Informe TEM del Colargol" sent October 15, 2008 from Laboratorios Argenol, S.I. Translated by Michael Stewart on October 20, 2008.

In this method, as opposed to SEM which is an analytical method performed on solid specimens, the sample is dissolved in distilled water and deposited on both copper and carbon substrates; then the solvent evaporates.

Due to the analytical method, we cannot distinguish the carbon contained within the substrate and that of the protein.

In these initial images the sample is shown in general views.

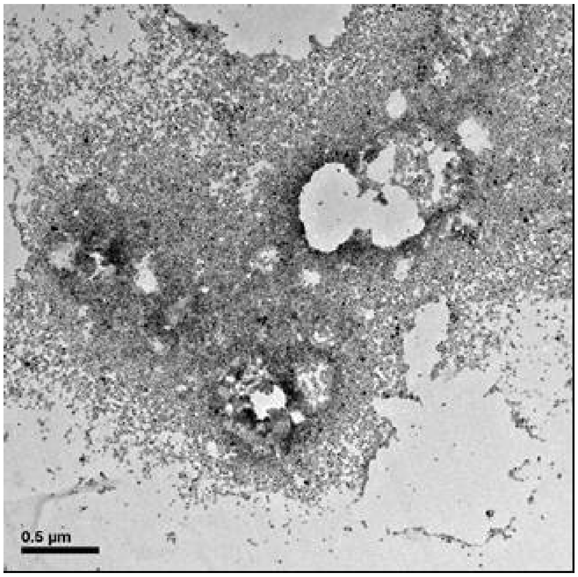

Upon analyzing the general composition both carbon and copper were found, due to the substrate used in this analysis; oxygen, sulfur, nitrogen, and silver, as expected for a sample of protein with silver and calcium and silicon.

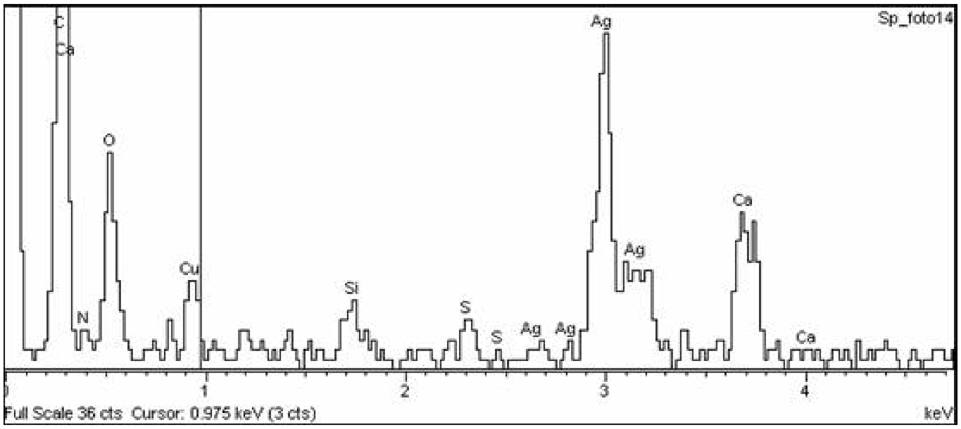
Sp_foto14
C
Ca
O
N
Cu
Si
S
S
Ag
Ag
Ag
Ag
Ca
Ca
0
1
2
3
4
Full Scale 36 cts Cursor: 0.975 keV (3 cts)
keV

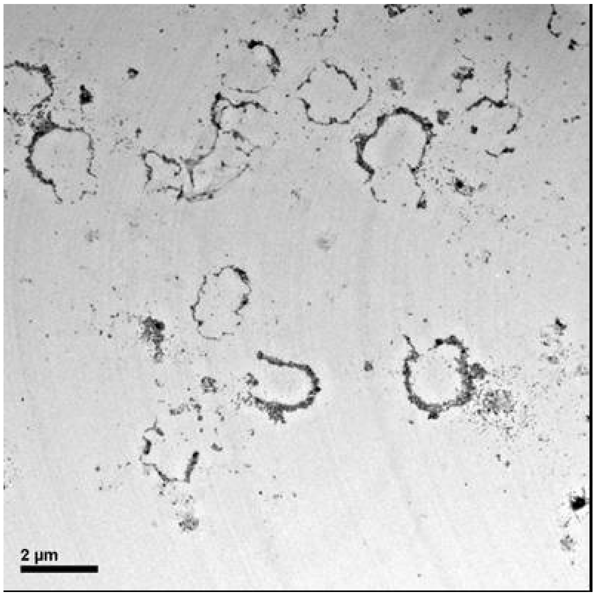
2 µm

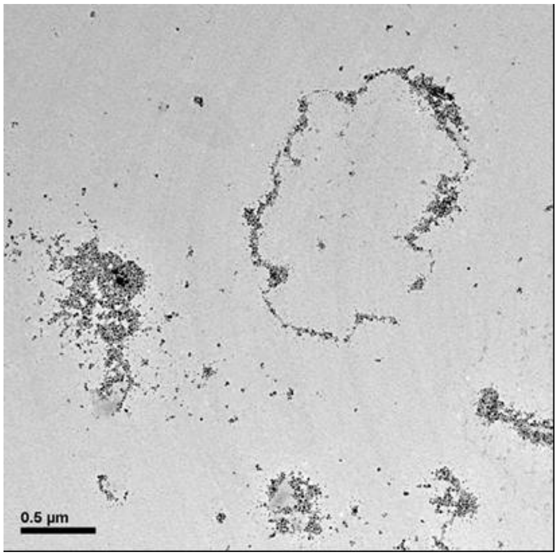
0.5 µm

In the following images we examine a region of the sample, with what appears to be nanoparticles of silver in solution and ridged areas that could be from the protein.

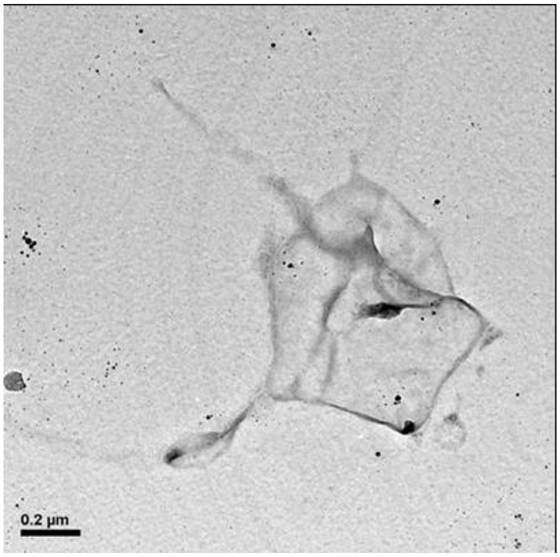

Upon analyzing the composition the presence of carbon, oxygen and a slight amount of nitrogen was identified, that we believe can be attributed to the presence of protein.

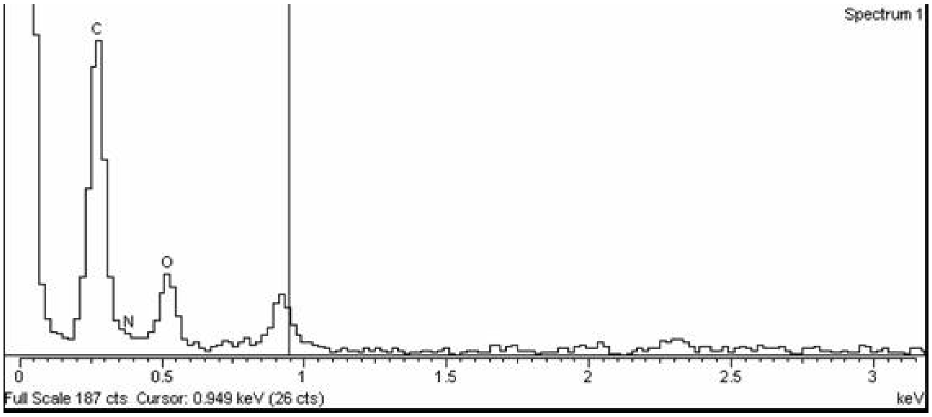

Higher magnification images were taken of certain regions of these “pleats” in order to observe them in greater detail.

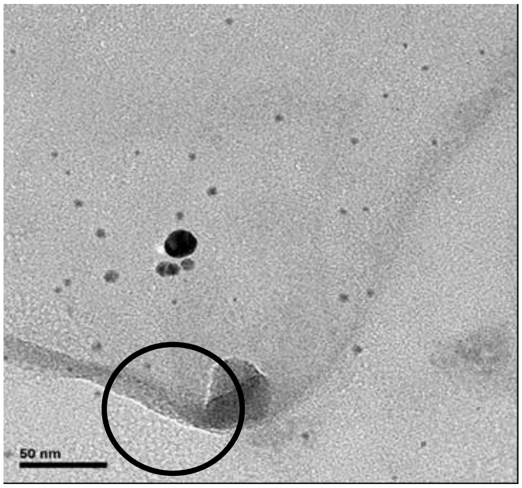

Analyzing the composition of the circled region returned oxygen, calcium, as well as silver.

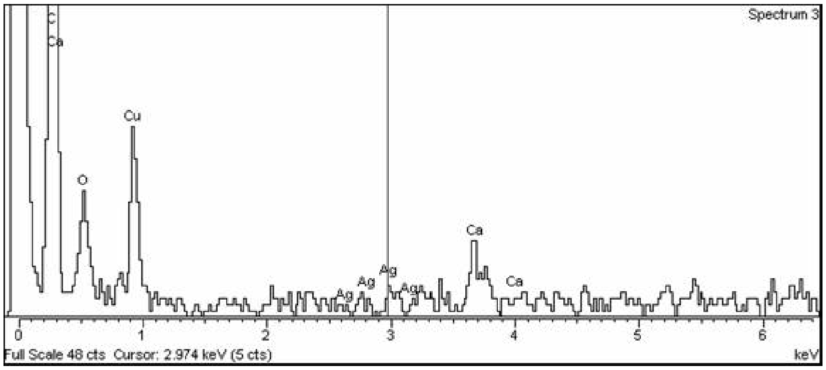

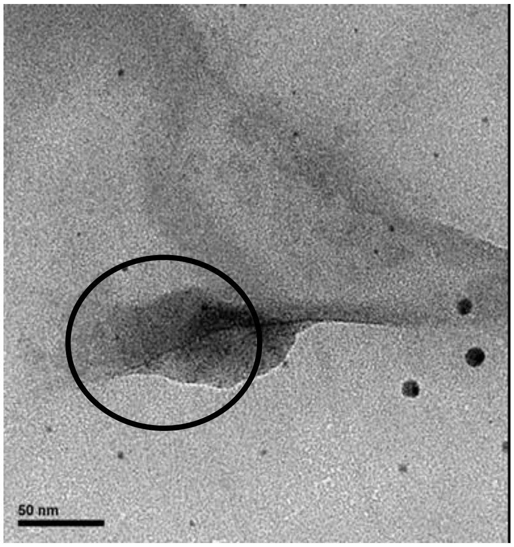

Compositional analysis of this darker region was performed with the expectation of raised percentages of nitrogen and oxygen (protein) but the results were the same as the zone outside of that region.

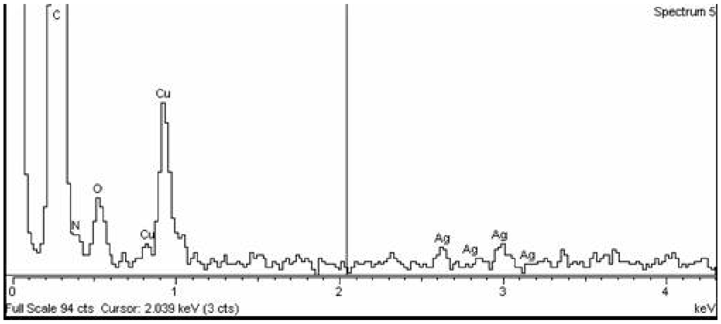

Other zones with a presence of nanoparticles of silver and pleats were sought, with the expectation of being able to locate protein.

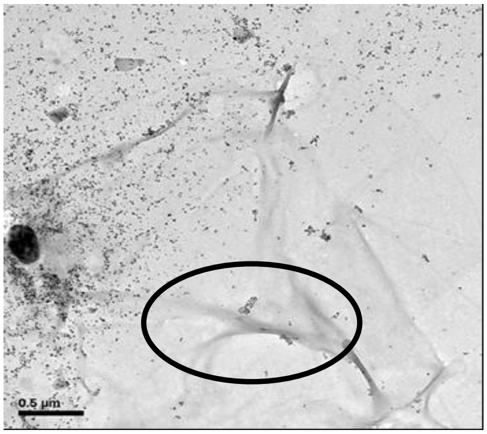

The composition of the circled zone was likely to show: nitrogen and oxygen (assuredly due to protein) and silver due to the presence of the nanoparticles.

Higher magnification images were taken of the black particle that is observed at the left side of the previous image.

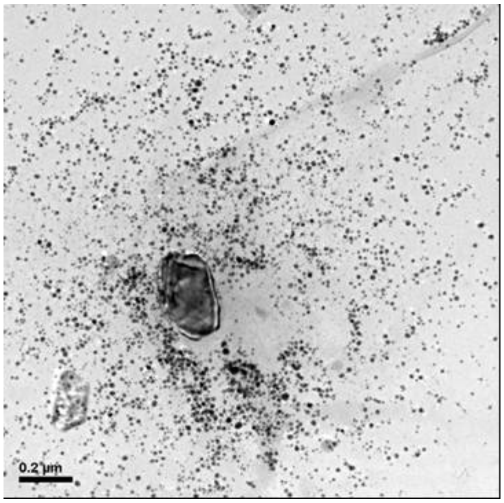

Upon analyzing the composition we found the presence of silver and above all else oxygen and calcium.

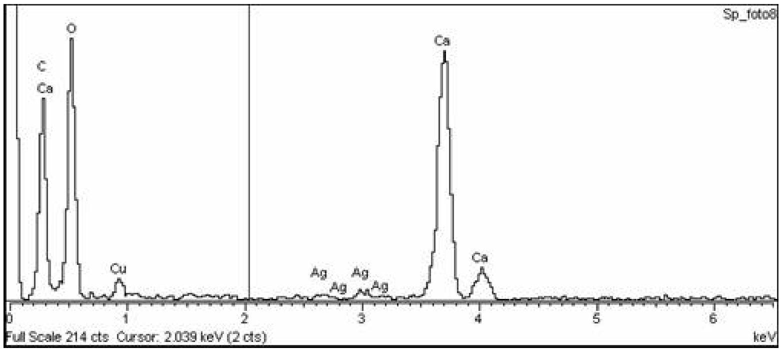

We also zoomed in on the regions where there seemed to be nanoparticles of silver in solution.

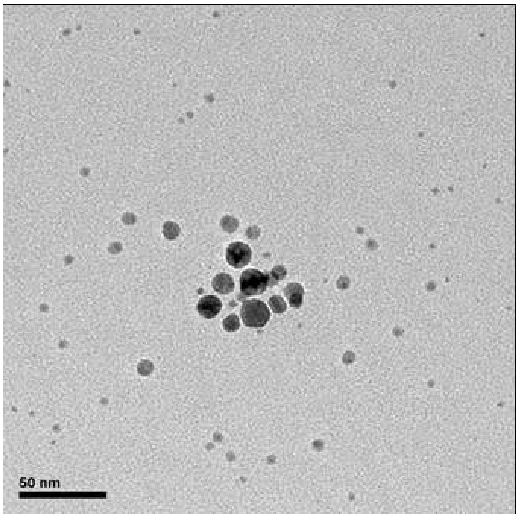

We zoomed in further on the nanoparticles and analyzed their composition.

After compositional analysis of one of these black particles we found the expected results: the exclusive presence of silver.

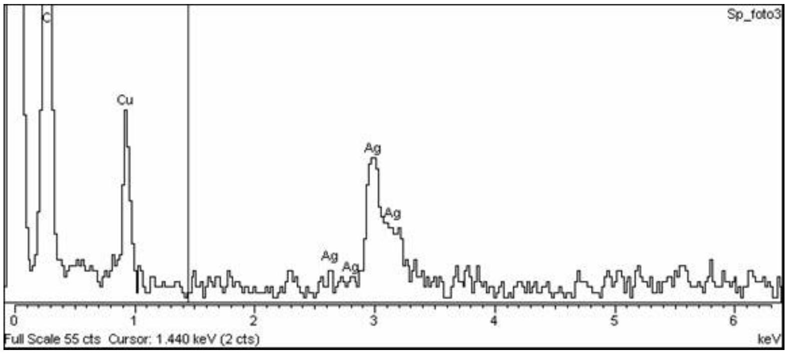

Upon zooming in on other particles we observe the same.

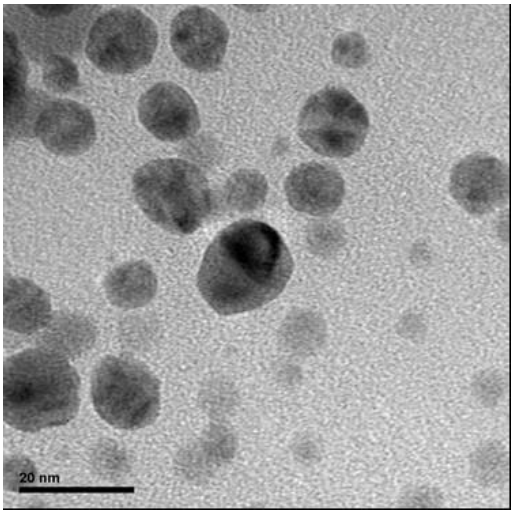

We found a region with a ridged molecule similar to that found through SEM.

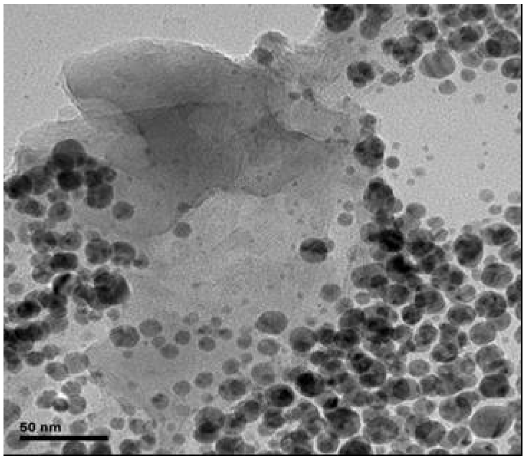

We zoomed in to image the region with more detail.

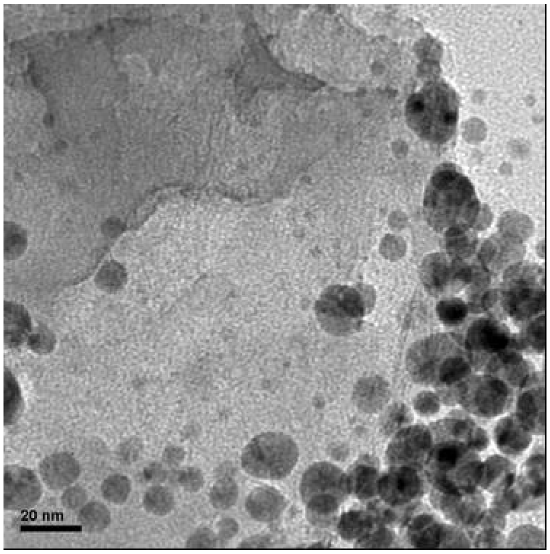

We zoomed in further yet.

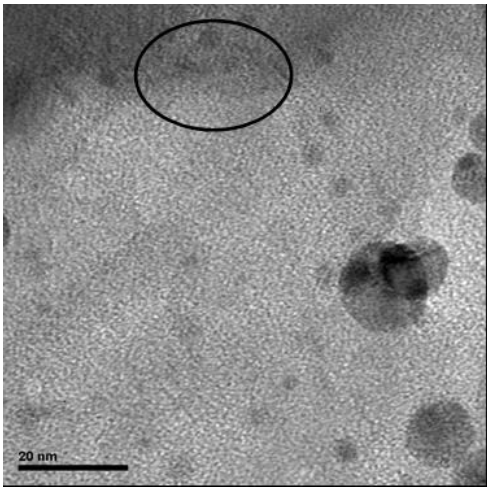

These last few enlargements do not provide any new data points due to the poor resolution, but one can clearly see the silver nanoparticles (black points) and a ridged area for which compositional anaylsis yields carbon (from the substrate and/or protein), oxygen and silver due to the presence of nanoparticles en the analyzed region.

Therefore, after this TEM analysis, we can verify the presence of silver nanoparticles and protein. Even though it does not appear that the nanoparticles are linked to the protein one must remember that the sample was diluted in water during its preparation, and because of this, could have undergone some change from its initial state.

Appendix C.2: Colloidal Silver Solution Mixing Procedures

Mixing of the stock 3.2 percent solution was performed according to the following procedure:

1. Pour 250 mL of Millipore ultrapure (type 1) water into an opaque HDPE bottle.
2. Add 8 g of Collargol silver powder to the Millipore water.
3. Shake vigorously for a minimum of 2 minutes.
4. Store this stock 3.2 percent solution at ambient temperature away from direct light. All experiments were performed within 12 months of mixing this stock solution.

Mixing of the 0.018 percent application solution was performed according to the following procedure:

1. Measure 250 mL of Millipore ultrapure (type 1) water into an opaque HDPE bottle.
2. Transfer 2 mL of the stock 3.2 percent solution into the Millipore water.
3. Shake vigorously for a minimum of 2 minutes.
4. Store this application solution at ambient temperature away from direct light. All experiments were performed within 2 months of mixing the application solution.

Appendix C.3: High Speed Centrifugation

> *"It has been empirically determined that a force-time integral in excess of 325 million G-seconds will suffice to separate out particles into the low nanometer range. When using a centrifuge that produces 1 million G-forces, it would have to dwell at that level for at least 325 seconds to insure particle separation. While a 1 million G-force centrifuges are available, they are extremely expensive and not cost effective for this purpose. Using a 365,000 G-force centrifuge the dwell time would increase to 890 seconds."*

(from http://www.silver-colloids.com/Papers/CSProperties.PDF)

Table of time-force integral calculations for the SW-41 rotor used in this investigation

SW 41 - Centrifuge data		
r	11.02	cm
ω	41000	rpm
By linear velocity		
circ	0.69	m
v(t)	473	m/s
g	9.8	m/s2
a(c)	2031452	m/s2
G	207291	G-forces
Dwell req'd		
t	1568	sec
=	26	min
=	0.4	hrs

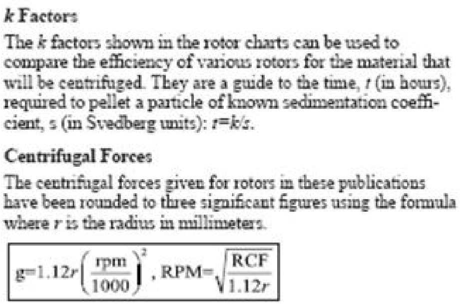

k Factors

The k factors shown in the rotor charts can be used to compare the efficiency of various rotors for the material that will be centrifuged. They are a guide to the time, t (in hours), required to pellet a particle of known sedimentation coefficient, s (in Svedberg units): $t=k/s$.

Centrifugal Forces

The centrifugal forces given for rotors in these publications have been rounded to three significant figures using the formula where r is the radius in millimeters.

$$\boxed{g=1.12r\left(\frac{\text{rpm}}{1000}\right)^2,\ \text{RPM}=\sqrt{\frac{\text{RCF}}{1.12r}}}$$

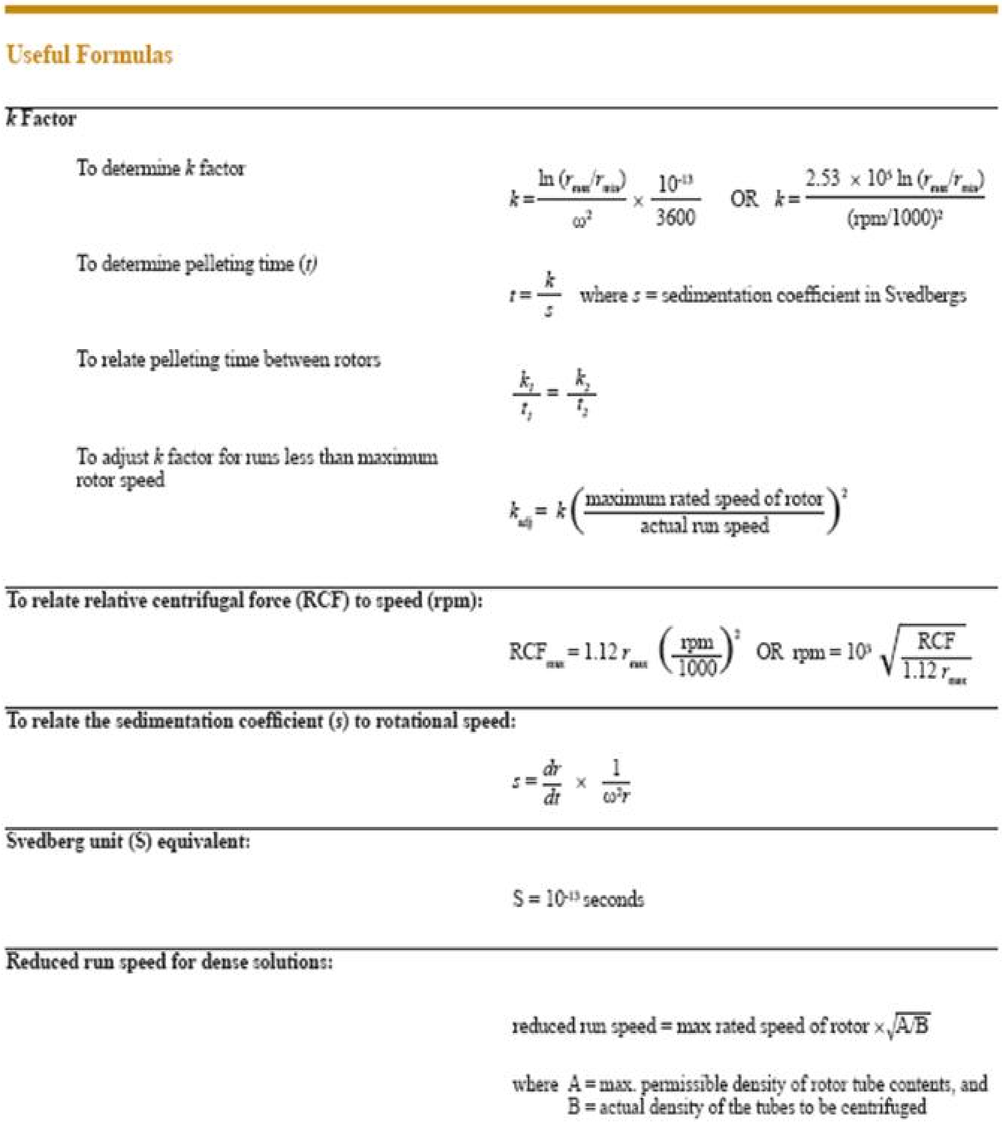

Useful Formulas

k Factor

To determine k factor

$$k = \frac{\ln(r_{max}/r_{min})}{\omega^2} \times \frac{10^{-13}}{3600} \quad \text{OR} \quad k = \frac{2.53 \times 10^5 \ln(r_{max}/r_{min})}{(\text{rpm}/1000)^2}$$

To determine pelleting time (t)

$$t = \frac{k}{s}$$ where s = sedimentation coefficient in Svedbergs

To relate pelleting time between rotors

$$\frac{k_1}{t_1} = \frac{k_2}{t_2}$$

To adjust k factor for runs less than maximum rotor speed

$$k_{adj} = k\left(\frac{\text{maximum rated speed of rotor}}{\text{actual run speed}}\right)^2$$

To relate relative centrifugal force (RCF) to speed (rpm):

$$\text{RCF}_{max} = 1.12\, r_{max} \left(\frac{\text{rpm}}{1000}\right)^2 \quad \text{OR} \quad \text{rpm} = 10^3 \sqrt{\frac{\text{RCF}}{1.12\, r_{max}}}$$

To relate the sedimentation coefficient (s) to rotational speed:

$$s = \frac{dr}{dt} \times \frac{1}{\omega^2 r}$$

Svedberg unit (S) equivalent:

$\text{S} = 10^{-13}$ seconds

Reduced run speed for dense solutions:

reduced run speed = max rated speed of rotor × $\sqrt{\text{A/B}}$

where A = max. permissible density of rotor tube contents, and
B = actual density of the tubes to be centrifuged

Appendix C.4: QSX-303 Sensor Specifications

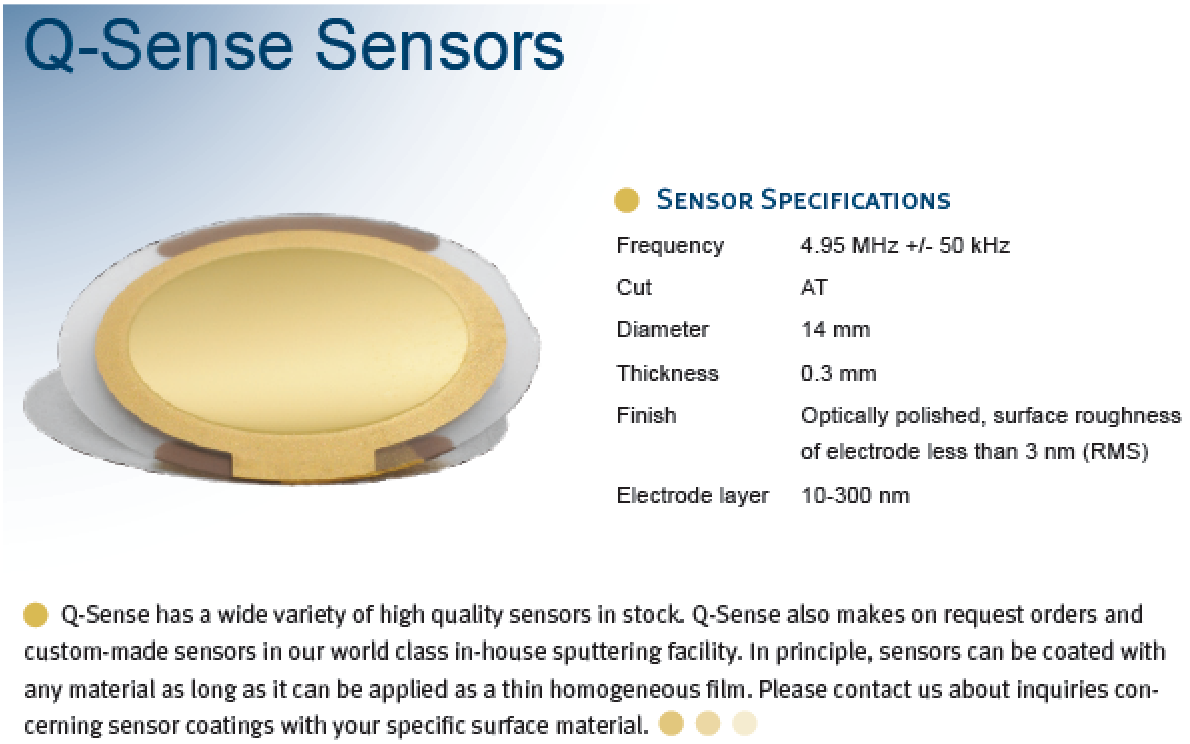

Q-Sense Sensors

Sensor Specifications

Frequency	4.95 MHz +/- 50 kHz
Cut	AT
Diameter	14 mm
Thickness	0.3 mm
Finish	Optically polished, surface roughness of electrode less than 3 nm (RMS)
Electrode layer	10-300 nm

Q-Sense has a wide variety of high quality sensors in stock. Q-Sense also makes on request orders and custom-made sensors in our world class in-house sputtering facility. In principle, sensors can be coated with any material as long as it can be applied as a thin homogeneous film. Please contact us about inquiries concerning sensor coatings with your specific surface material.

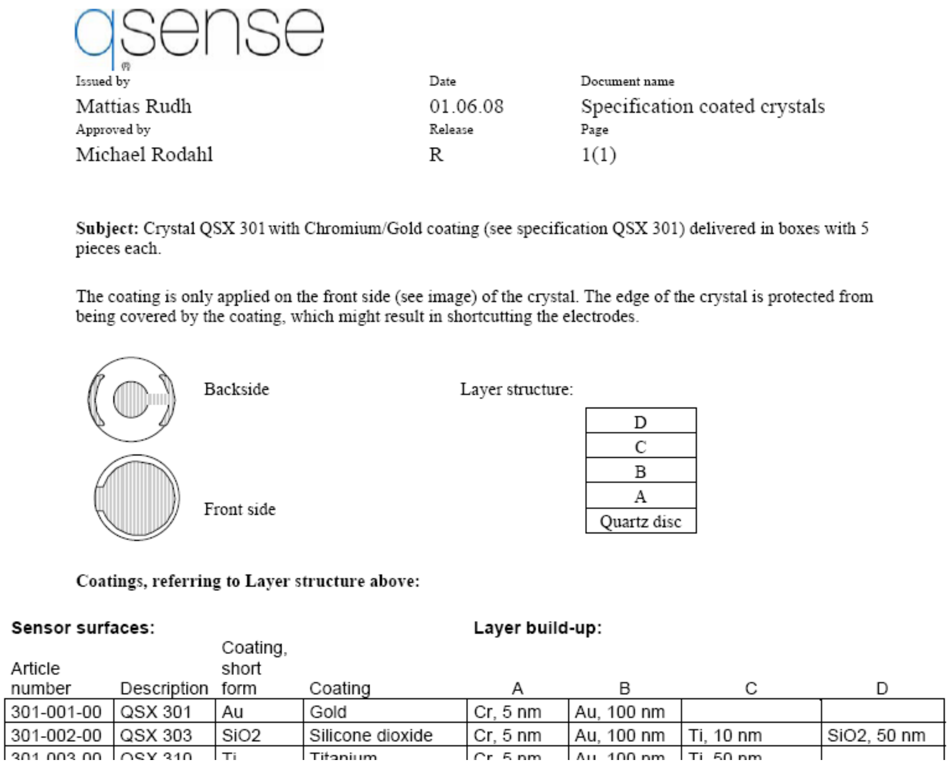

qsense

Issued by	Date	Document name
Mattias Rudh	01.06.08	Specification coated crystals
Approved by	Release	Page
Michael Rodahl	R	1(1)

Subject: Crystal QSX 301 with Chromium/Gold coating (see specification QSX 301) delivered in boxes with 5 pieces each.

The coating is only applied on the front side (see image) of the crystal. The edge of the crystal is protected from being covered by the coating, which might result in shortcutting the electrodes.

Backside

Front side

Layer structure:

D
C
B
A
Quartz disc

Coatings, referring to Layer structure above:

Sensor surfaces: **Layer build-up:**

Article number	Description	Coating, short form	Coating	A	B	C	D
301-001-00	QSX 301	Au	Gold	Cr, 5 nm	Au, 100 nm		
301-002-00	QSX 303	SiO2	Silicone dioxide	Cr, 5 nm	Au, 100 nm	Ti, 10 nm	SiO2, 50 nm
301-003-00	QSX 310	Ti	Titanium	Cr, 5 nm	Au, 100 nm	Ti, 50 nm	

(intentionally truncated)

Appendix C.5: <u>QCM Sensor Cleaning Procedures</u>

1. <u>UV/ozone cleaning</u> – a BioForce Nanosciences ProCleaner ™ UV/ozone device was used to destroy and remove organic contaminants from the surface of the sensors. This device incorporates a 254 nm mercury vapor lamp to inactivate microbial contaminants and to break surface bonds of other organic contaminants. Beyond that, lamp emission at 185 nm reportedly reacts with oxygen to produce ozone, which aids in the disruption of organic contaminants bonded to the sensor surface. Each sensor was subjected to 12-15 minutes in the UV/ozone cleaner.

2. <u>Sodium Dodecyl Sulfate (SDS) soak</u> – each sensor was placed into a 2 percent solution of SDS for a minimum of 30 minutes. SDS is an anionic surfactant used in detergents and cleaning products, as well as for protein preparation in advance of electrophoresis.

3. <u>Ultrapure water rinse</u> – each sensor was rinsed 3 times front and back with Millipore ultrapure water. The sensor was always handled with tweezers, and every effort was made to flow water down the face of the sensor towards the tweezer, so as not to contaminate the surface of the sensor.

4. <u>Drying</u> – each sensor was then dried using industrial grade dry nitrogen at an exit pressure of 20-30 psi until no visible rinse water remained on the sensor.

5. <u>UV/ozone cleaning</u> – each sensor was once again subjected to 12-15 minutes in the UV/ozone cleaner before being considered ready for use.

Appendix D: Results

Appendix D.1: Frequency and Dissipation Shifts for Silver Deposition (taken dry)

Ag Dry	**Millipore, pH = 5.8**								**Kaolin, 51 NTU, pH=5.6**			
	Scaled Frequency								**Scaled Frequency**			
1st	-297	-359	-3682	ND	-285	-383	-330	-297	-376	-397	-364	-349
3rd	-437	-523	-3855	ND	-240	-525	-591	-451	-420	-600	-521	-452
5th	-534	-636	-4023	ND	-234	-628	-737	-535	-431	-682	-570	-530
7th	-611	-748	-4330	ND	-254	-725	-912	-627	-382	-713	-588	-590
9th	-647	-865	-4670	ND	-283	-829	-1108	-703	-336	-720	-585	-643
11th	171	-1038	-3287	ND	-371	-967	-1380	-808	-258	-1759	-581	-712
13th	-734	-1142	-3353	ND	-468	-164	-266	-894	-216	-714	-1752	-777
	Dissipation								**Dissipation**			
1st	0.5	-0.4	2.7	ND	1.1	0.2	-0.4	0.6	-0.4	-0.2	0.1	1.0
3rd	0.2	0.2	2.2	ND	2.1	0.5	2.3	1.1	0.2	1.5	-0.3	3.3
5th	0.8	-3.3	6.0	ND	3.4	2.5	-1.6	7.2	0.4	1.8	0.8	4.0
7th	1.8	2.1	14.4	ND	1.2	2.7	11.4	1.5	1.0	1.8	0.9	3.1
9th	9.2	0.8	30.5	ND	-7.2	2.8	7.8	4.1	-1.0	2.2	1.6	4.3
11th	1.3	-1.4	14.4	ND	4.0	2.4	15.8	2.6	1.6	5.5	2.1	5.0
13th	4.2	7.1	23.5	ND	4.3	1.2	2.0	0.7	1.6	4.0	2.9	5.3

Ag Dry	**HNO_3, pH=4.8**				**NaOH, pH=9.3**				**NaNO3, 150 mM, pH=5.4**			
	Scaled Frequency				**Scaled Frequency**				**Scaled Frequency**			
1st	-338	-432	-332	-290	-445	-484	-426	-394	-266	ND	-275	-285
3rd	-522	-667	-553	-467	-581	-771	-686	-718	-301	ND	-368	-406
5th	-648	-817	-625	-537	-689	-951	-950	-915	-328	ND	-410	-473
7th	-864	-947	-707	-585	-855	572	-1304	-1129	-403	ND	-454	-534
9th	-1170	-1092	-787	-612	121	-1247	-645	-1328	-523	ND	-507	-594
11th	-54	-1262	-870	-644	-731	-320	374	-1599	244	ND	-569	-678
13th	-140	-1385	-915	-671	-206	324	359	389	-312	ND	-649	-757
	Dissipation				**Dissipation**				**Dissipation**			
1st	0.8	5.5	7.8	1.9	20.2	5.7	0.6	0.2	5.1	ND	1.0	0.8
3rd	2.9	18.7	16.8	1.0	21.5	7.7	0.6	0.2	3.3	ND	-0.3	0.3
5th	3.7	24.9	5.4	1.4	23.1	15.7	0.5	0.4	5.7	ND	0.1	0.4
7th	9.2	31.1	35.8	1.6	29.1	11.7	5.9	2.4	3.5	ND	0.3	0.8
9th	20.6	36.4	4.6	4.7	20.0	26.5	6.7	6.3	17.7	ND	1.3	1.3
11th	12.0	31.4	9.1	2.2	25.3	18.9	5.1	10.4	-4.0	ND	5.9	2.1
13th	16.3	33.1	7.1	2.2	20.9	17.9	9.1	2.4	3.5	ND	4.1	2.9

Ag Dry	**Ca(NO$_3$)$_2$, 150mM, pH=5.7**				**NOM 15 mg/L TOC, pH=7.1**			
	Scaled Frequency				**Scaled Frequency**			
1st	-258	-377	-208	-341	-279	-444	-421	-471
3rd	-336	-514	-227	-577	-293	-706	-575	-519
5th	-389	-612	-232	-753	-313	-902	-671	-589
7th	-457	-721	-253	-952	-348	-1096	-750	-659
9th	-546	-851	-277	-1131	-410	-1258	-813	-724
11th	-652	-1062	-320	-1350	-530	-1484	-893	-796
13th	-762	-1243	-373	1107	-643	492	-957	-857
	Dissipation				**Dissipation**			
1st	1.0	0.3	-0.9	1.6	7.1	1.8	-0.4	0.6
3rd	-0.3	1.4	1.1	0.6	11.4	3.9	0.7	1.7
5th	2.5	0.9	0.4	1.5	10.7	7.7	2.5	0.3
7th	7.3	1.5	1.2	3.7	9.4	6.3	2.8	0.7
9th	13.2	2.5	1.4	5.7	11.6	12.2	4.9	2.1
11th	17.4	2.5	0.9	11.0	13.0	15.3	6.0	1.8
13th	20.0	3.3	1.5	-1.7	13.1	3.9	6.6	2.5

Ag Dry	**NaOCl, 525 mg/L, pH=8.5**				**NaOCl, 8.8 mg/L, pH=8.5**			
	Scaled Frequency				**Scaled Frequency**			
1st	-350	-321	-321	-407	1904	-265	-287	-356
3rd	-488	-368	-368	-522	-122	-336	-347	-447
5th	-584	-435	-435	-616	-350	-402	-350	-474
7th	-659	-493	-493	-727	-430	320	-388	-509
9th	-726	-543	-543	-814	-468	-637	-445	-554
11th	-798	-607	-607	-914	-488	-161	-591	-630
13th	-859	-658	-658	101	-506	-312	-85	-650
	Dissipation				**Dissipation**			
1st	3.7	5.9	5.9	11.5	76.1	1.5	16.6	6.6
3rd	7.4	2.6	2.6	17.8	7.3	4.1	19.3	7.6
5th	11.3	4.1	4.1	22.3	7.4	6.8	21.6	15.7
7th	13.6	5.4	5.4	27.6	13.2	5.0	27.5	19.9
9th	14.9	6.8	6.8	36.3	19.8	11.5	36.0	26.5
11th	18.1	10.9	10.9	41.3	25.9	5.5	40.4	36.4
13th	16.8	12.7	12.7	11.6	31.7	7.1	17.0	40.4

Appendix D.2: Frequency and Dissipation Shifts for Baseline Flow

Baseline flow	Millipore, pH = 5.8								Kaolin, 51 NTU, pH=5.6			
	Scaled Frequency								Scaled Frequency			
1st	-710	-685	-726	-695	-719	-681	-715	-681	-773	-673	-729	-677
3rd	-393	-396	-390	-395	-386	-413	-394	-388	-405	-382	-399	-383
5th	-304	-308	-299	-303	-299	-322	-306	-301	-309	-288	-305	-293
7th	-257	-256	-252	-255	-247	-275	-256	-251	-260	-235	-253	-244
9th	-223	-226	-221	-225	-203	-244	-225	-220	-225	-203	-222	-214
11th	-201	-203	-198	-201	-196	-220	-201	-197	-205	ND	-198	-191
13th	-184	-185	-181	-185	-178	-204	-184	-183	-190	-159	ND	-177
	Dissipation								Dissipation			
1st	332.4	351.0	320.7	340.9	337.3	353.4	333.2	345.0	339.6	359.0	323.8	350.2
3rd	162.4	163.3	162.9	162.6	162.2	162.9	162.5	162.2	162.9	165.0	162.4	162.0
5th	126.7	123.9	126.5	126.8	128.6	126.9	120.2	126.6	128.1	128.5	127.5	126.2
7th	105.7	105.5	105.1	105.1	105.9	105.4	105.1	105.4	106.7	105.8	106.0	105.2
9th	94.9	94.4	93.9	94.0	88.3	94.2	93.9	94.2	96.8	93.7	94.7	93.5
11th	85.0	84.9	84.5	84.7	84.7	84.7	84.7	84.1	86.9	86.0	85.4	83.2
13th	79.0	78.7	78.6	78.7	78.0	78.8	78.6	77.1	81.7	77.6	81.4	77.1

Baseline flow	HNO_3, pH=4.8				NaOH, pH=9.3				NaNO3, 150 mM, pH=5.4			
	Scaled Frequency				Scaled Frequency				Scaled Frequency			
1st	-716	-680	-721	-674	-686	-681	-693	-720	-730	ND	-770	-568
3rd	-397	-395	-386	-394	-389	-394	-391	-394	-402	ND	-416	-377
5th	-306	-304	-295	-302	-300	-302	-299	-302	-311	ND	-325	-286
7th	-259	-256	-254	-254	-252	-254	-252	-258	-262	ND	-277	-239
9th	-229	-225	-220	-223	-222	-224	-221	-227	-227	ND	-245	-209
11th	-207	-201	-185	-199	-199	-201	-197	-204	-209	ND	-222	-185
13th	-189	-184	-181	-183	-183	-185	-181	-188	-192	ND	-204	-169
	Dissipation				Dissipation				Dissipation			
1st	338.4	352.4	334.2	347.5	347.8	346.2	354.6	339.7	334.9	ND	327.2	330.7
3rd	162.6	162.4	170.2	162.2	162.4	163.2	162.0	162.1	164.0	ND	164.5	164.3
5th	126.2	126.6	126.3	126.7	126.5	126.8	126.6	126.6	127.9	ND	127.4	127.5
7th	105.2	105.5	107.5	105.4	105.2	105.3	105.2	105.2	106.4	ND	106.1	106.2
9th	93.8	94.5	92.0	94.3	94.0	93.9	94.1	94.1	95.5	ND	94.9	94.6
11th	84.1	84.9	85.9	84.6	84.7	84.6	84.5	84.9	83.2	ND	85.3	85.1
13th	78.2	78.9	79.2	78.8	79.2	78.8	78.7	79.6	78.7	ND	79.2	79.2

Baseline flow	**$Ca(NO_3)_2$, 150mM, pH=5.7**				**NOM 15 mg/L TOC, pH=7.1**			
	Scaled Frequency				**Scaled Frequency**			
1st	-717	-699	-719	-723	-756	-737	-727	-755
3rd	-403	-417	-384	-395	-397	-400	-395	-397
5th	-312	-325	-294	-304	-308	-309	-304	-309
7th	-262	-276	-245	-255	-260	-261	-257	-258
9th	-230	-244	-215	-224	-229	-230	-225	-223
11th	-205	-219	-190	-198	-205	-206	-201	-197
13th	-187	-201	-173	-181	-188	-188	-183	-182
	Dissipation				**Dissipation**			
1st	338.1	360.8	329.3	339.7	332.1	349.5	299.9	333.6
3rd	165.1	165.4	165.8	166.2	162.7	162.1	163.1	161.8
5th	128.6	128.8	128.9	129.5	126.5	126.4	126.7	126.5
7th	107.5	107.4	107.1	107.9	105.5	105.4	105.4	106.2
9th	95.8	95.7	95.5	96.3	94.2	94.2	94.4	94.1
11th	85.5	85.8	86.0	86.2	84.5	84.9	85.0	81.9
13th	78.2	78.7	79.8	79.6	77.8	78.6	78.8	75.7

Baseline flow	**NaOCl, 525 mg/L, pH=8.5**				**NaOCl, 8.8 mg/L, pH=8.5**			
	Scaled Frequency				**Scaled Frequency**			
1st	-707	-696	-719	-730	-694	-654	-735	-753
3rd	-388	-403	-386	-403	-395	-379	-405	-419
5th	-297	-311	-298	-314	-306	-293	-316	-326
7th	-248	-263	-252	-264	-257	-247	-269	-276
9th	-218	-232	-220	-231	-227	-216	-237	-244
11th	-192	-207	-197	-206	-203	-193	-215	-222
13th	-174	-191	-183	-191	-189	-175	-201	-209
	Dissipation				**Dissipation**			
1st	333.2	309.5	332.3	340.1	334.0	325.6	327.4	337.9
3rd	163.3	163.6	163.0	161.7	161.3	155.4	162.6	157.0
5th	127.0	126.9	126.8	127.2	125.2	123.3	126.5	126.0
7th	106.0	105.8	105.2	105.8	104.5	102.5	105.3	104.5
9th	94.3	94.3	93.6	93.8	92.7	90.9	93.3	93.3
11th	84.3	84.6	83.4	82.1	82.4	79.8	82.5	82.2
13th	77.6	78.1	77.7	75.7	76.5	73.6	76.1	75.8

Appendix D.3: Frequency and Dissipation Shifts for Silver Flow

Flow data recorded from Millipore Baseline and Silver Flow runs (Group 1 of 2)

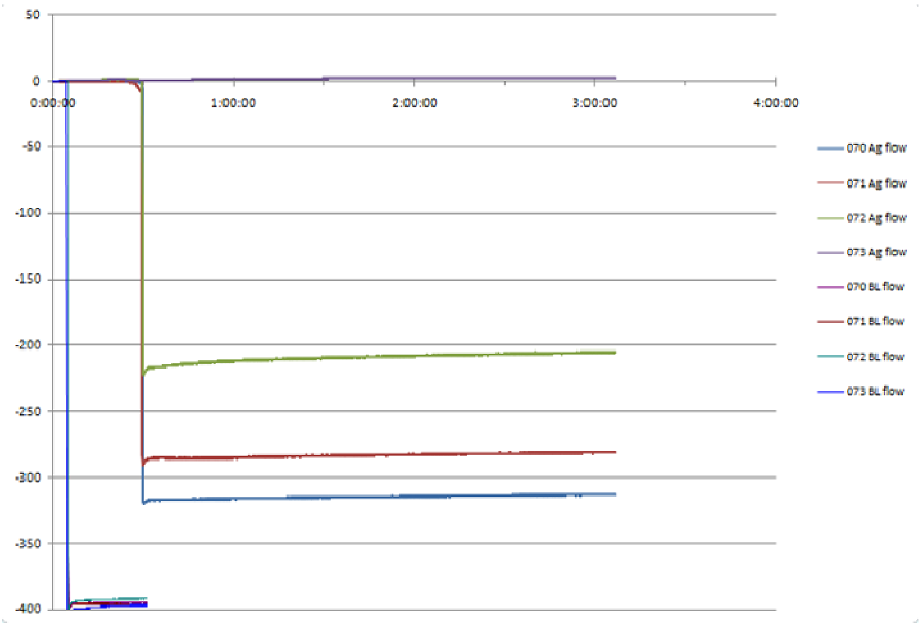

Flow data recorded from Millipore Baseline and Silver Flow runs (Group 2 of 2)

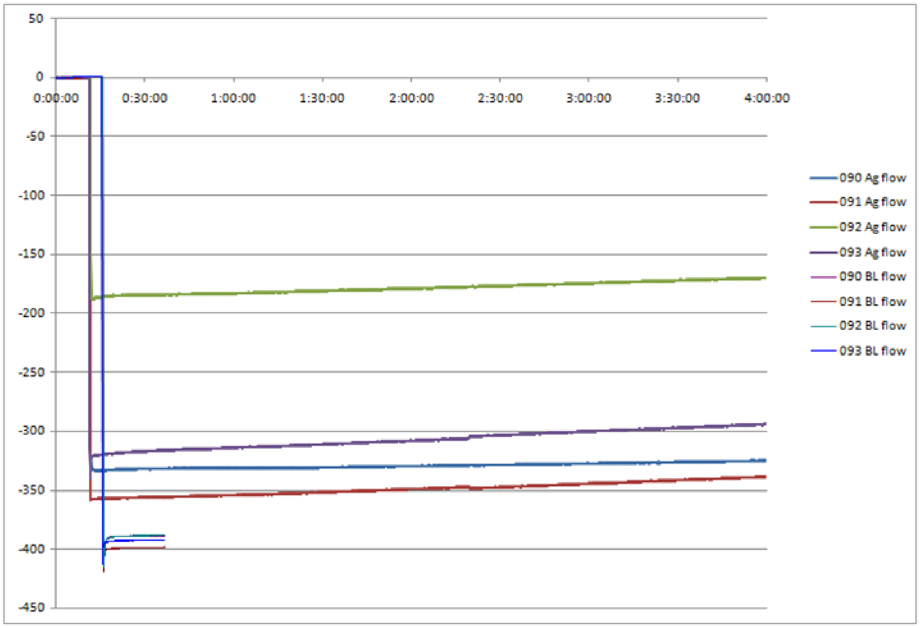

Flow data recorded from turbid (51 NTU) Baseline and Silver Flow runs

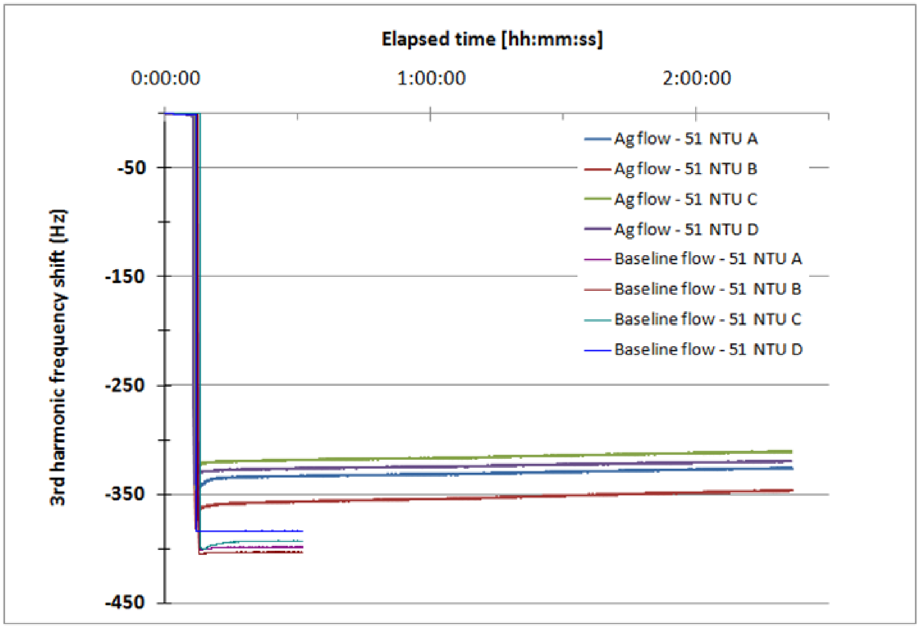

Flow data recorded from low pH (pH=4.7) Baseline and Silver Flow runs

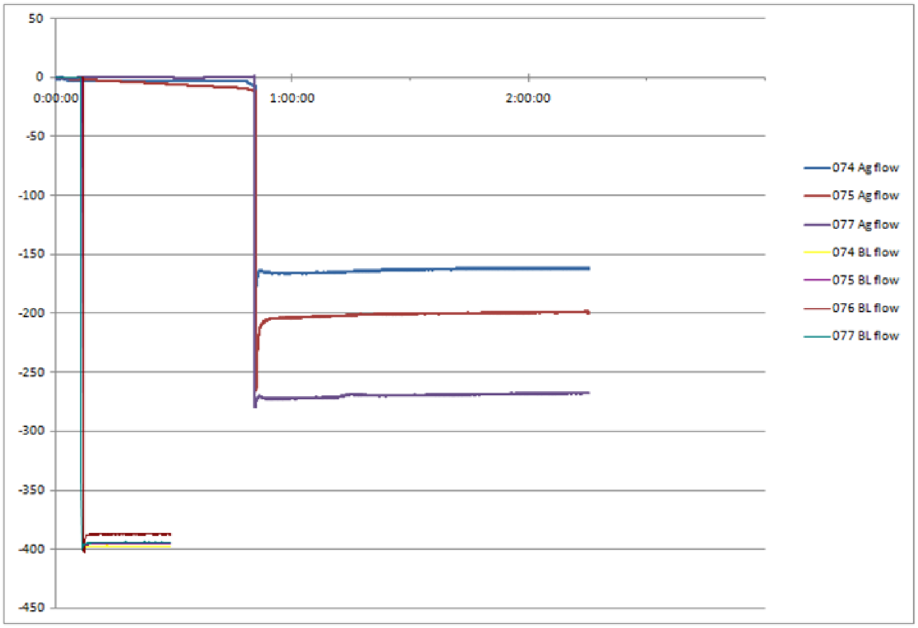

Flow data recorded from high pH (pH=9.3) Baseline and Silver Flow runs

Flow data recorded from monovalent ion ($NaNO_3$) Baseline and Silver Flow runs

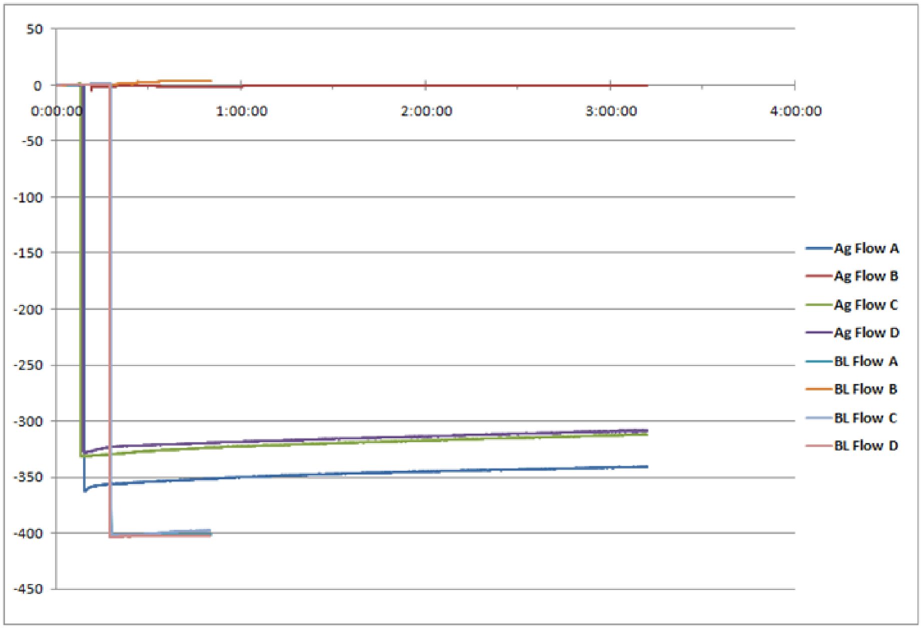

Flow data recorded from divalent ion ($Ca(NO_3)_2$) Baseline and Silver Flow runs

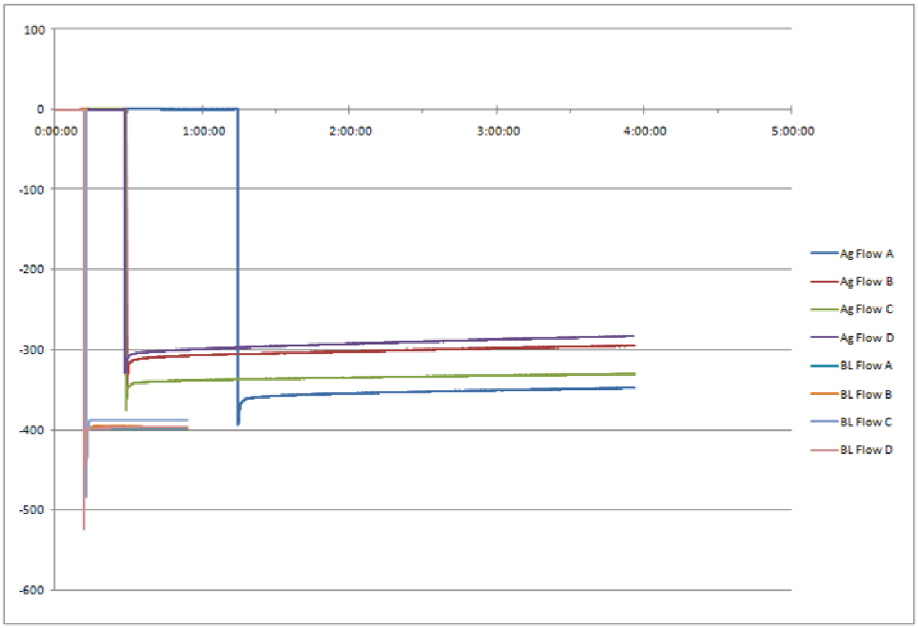

Flow data recorded from NOM waters (15 mg/L) Baseline and Silver Flow runs

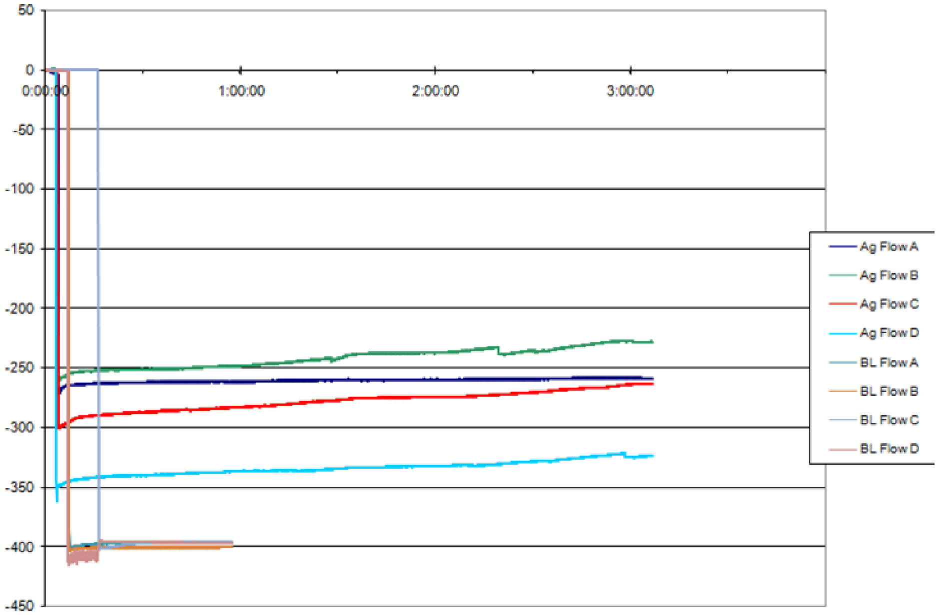

Flow data recorded from NaOCl waters (525 mg/L) Baseline and Silver Flow runs

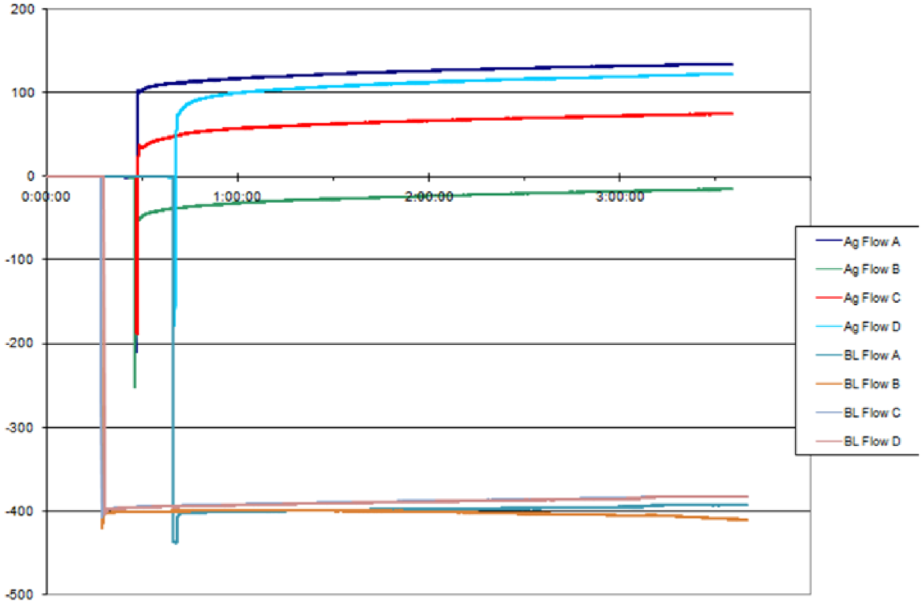

Flow data recorded from NaOCl waters (8.8 mg/L) Baseline and Silver Flow runs

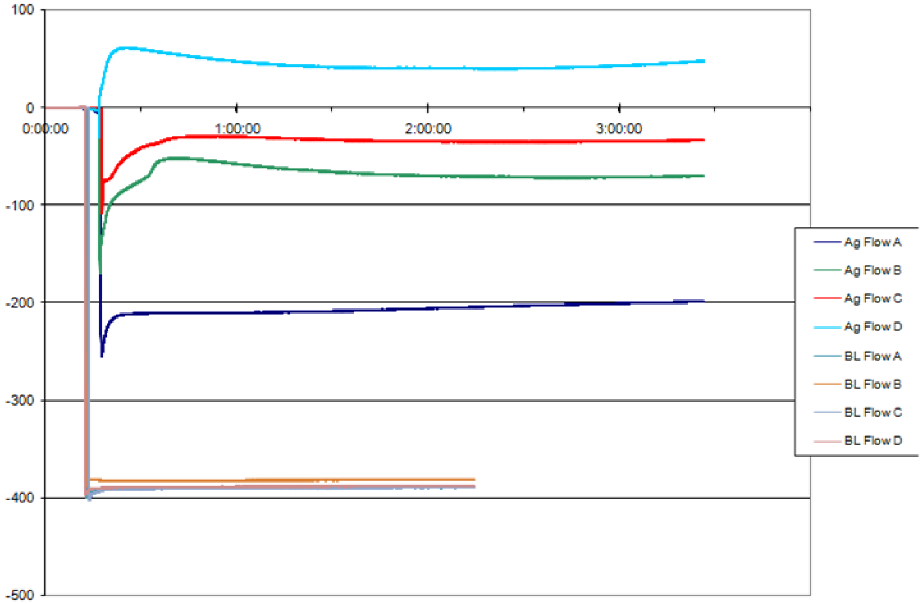

Appendix D.4: Frequency and Dissipation Shifts for Post Flow

Post flow	Millipore, pH = 5.8								Kaolin, 51 NTU, pH=5.6			
(rel. to Baseline dry)	**Scaled Frequency**								**Scaled Frequency**			
1st	-181	-305	-3566	ND	-257	-312	-240	-237	-332	-531	-284	-336
3rd	-300	-404	-3673	ND	-188	-426	-429	-380	-367	-644	4843	-412
5th	-383	-488	-3794	ND	-170	-518	-552	-448	-369	-692	-467	-468
7th	-453	-577	-4021	ND	-177	-605	-697	-528	-321	-699	-495	-515
9th	-495	-680	-4322	ND	-186	-701	-865	-591	-272	-685	-500	-553
11th	-541	-846	-3107	ND	-238	-825	-1108	-687	-202	-1710	-504	-604
13th	-588	119	-3225	ND	-294	-929	ND	-764	-166	-658	-1677	-652
	Dissipation								**Dissipation**			
1st	1.3	-0.2	3.5	ND	7.3	1.1	1.2	6.2	-0.4	10.8	0.9	5.6
3rd	0.4	0.2	2.0	ND	6.5	0.9	5.2	1.9	1.5	11.3	-9.4	8.0
5th	0.3	-2.2	4.0	ND	5.2	2.0	0.5	3.8	3.6	15.1	1.0	6.2
7th	2.8	0.6	10.9	ND	1.9	2.8	7.7	4.1	5.7	17.5	0.8	8.9
9th	7.9	0.8	27.3	ND	-8.3	2.7	7.7	3.5	5.4	17.3	1.4	11.0
11th	7.1	-0.1	7.8	ND	2.3	2.1	11.8	1.7	6.1	20.2	2.1	12.3
13th	3.9	-1.2	24.1	ND	2.6	3.3	ND	0.6	4.6	18.5	2.7	16.2

Post flow	HNO_3, pH=4.8				NaOH, pH=9.3				NaNO3, 150 mM, pH=5.4			
(rel. to Baseline dry)	**Scaled Frequency**				**Scaled Frequency**				**Scaled Frequency**			
1st	-253	-347	-327	-271	-260	-342	-440	-428	-327	ND	-285	-375
3rd	-365	-523	-560	-370	-338	-534	-676	-646	-320	ND	-355	-422
5th	-451	-642	-625	-428	-418	-666	-927	-820	-332	ND	-379	-465
7th	-589	-767	-714	-471	-538	-796	-1279	-1013	-381	ND	-411	-510
9th	-799	-893	-777	-499	-702	-899	344	-1195	-474	ND	-445	-554
11th	74	-1015	-859	-519	-958	-1036	15	828	-599	ND	-492	-625
13th	-13	-1135	-910	-543	-4	-1140	378	464	117	ND	-551	-694
	Dissipation				**Dissipation**				**Dissipation**			
1st	-1.1	3.4	7.1	2.9	8.0	3.7	2.2	8.6	22.4	ND	20.5	20.5
3rd	3.1	11.9	17.2	0.9	2.3	2.7	0.4	0.9	21.2	ND	19.1	19.3
5th	2.0	17.4	8.3	1.3	2.0	5.4	0.9	0.4	26.1	ND	17.7	17.2
7th	3.4	23.7	33.7	1.4	2.8	8.1	4.3	1.9	22.5	ND	20.3	17.2
9th	8.8	28.1	5.8	7.2	6.4	10.4	0.6	5.2	29.0	ND	19.4	17.1
11th	-0.3	30.2	9.8	2.3	7.9	11.9	2.1	0.8	25.5	ND	25.9	17.3
13th	2.6	30.3	5.9	1.6	2.1	15.9	7.6	1.6	10.8	ND	21.4	17.6

Post flow	**$Ca(NO_3)_2$, 150mM, pH=5.7**				**NOM 15 mg/L TOC, pH=7.1**			
(rel. to Baseline dry)	**Scaled Frequency**				**Scaled Frequency**			
1st	-381	-702	-380	-497	-113	-356	-231	-458
3rd	-425	-713	-405	-664	-133	-572	-427	-438
5th	-467	-754	-401	-803	-138	-750	-516	-498
7th	-524	-818	-413	-976	-157	-934	-591	-563
9th	-599	-910	-425	-1131	-201	-1091	-652	-626
11th	-697	-1085	-456	-1328	-296	937	-733	-693
13th	-2	-1243	-490	1060	-401	612	-805	-753
	Dissipation				**Dissipation**			
1st	29.5	78.6	46.3	38.5	1.6	-1.0	0.5	2.0
3rd	25.0	75.7	42.6	37.8	4.4	7.4	0.3	0.8
5th	28.1	71.8	41.3	36.1	5.0	6.0	0.8	0.9
7th	33.0	69.1	40.6	38.9	2.7	7.4	0.5	1.2
9th	40.8	65.4	40.8	45.6	4.5	13.0	1.6	2.4
11th	42.9	58.1	39.1	54.6	3.6	0.7	1.4	2.7
13th	18.2	56.6	37.3	16.0	3.5	2.2	1.2	1.8

Post flow	**NaOCl, 525 mg/L, pH=8.5**				**NaOCl, 8.8 mg/L, pH=8.5**			
(rel. to Baseline dry)	**Scaled Frequency**				**Scaled Frequency**			
1st	-97	-104	-55	-79	-42	-53	-4	-65
3rd	-73	-39	-55	-81	-37	-52	-19	-74
5th	-65	-40	-56	-88	-37	-60	-20	-67
7th	-65	-40	-54	-89	-39	-77	-23	-73
9th	-63	-42	-56	-94	-40	-100	-22	-75
11th	-65	-44	-52	-94	-41	-128	-29	-75
13th	-62	-47	-55	-91	-41	-145	-27	-78
	Dissipation				**Dissipation**			
1st	-0.1	11.9	5.5	0.4	0.5	2.4	1.1	0.6
3rd	2.9	0.7	3.4	1.1	-0.8	1.3	0.8	-4.5
5th	3.4	0.6	1.9	1.1	-1.1	3.0	0.6	1.5
7th	2.1	0.8	1.1	2.8	-0.5	5.1	0.9	1.0
9th	2.1	0.6	2.7	2.8	-0.5	9.7	1.5	2.1
11th	2.7	-0.5	0.6	2.7	0.2	19.1	3.4	2.4
13th	2.5	2.5	0.1	3.2	0.2	31.3	5.3	3.4

Appendix D.5: Optical Micrographs of Post Flow Condition

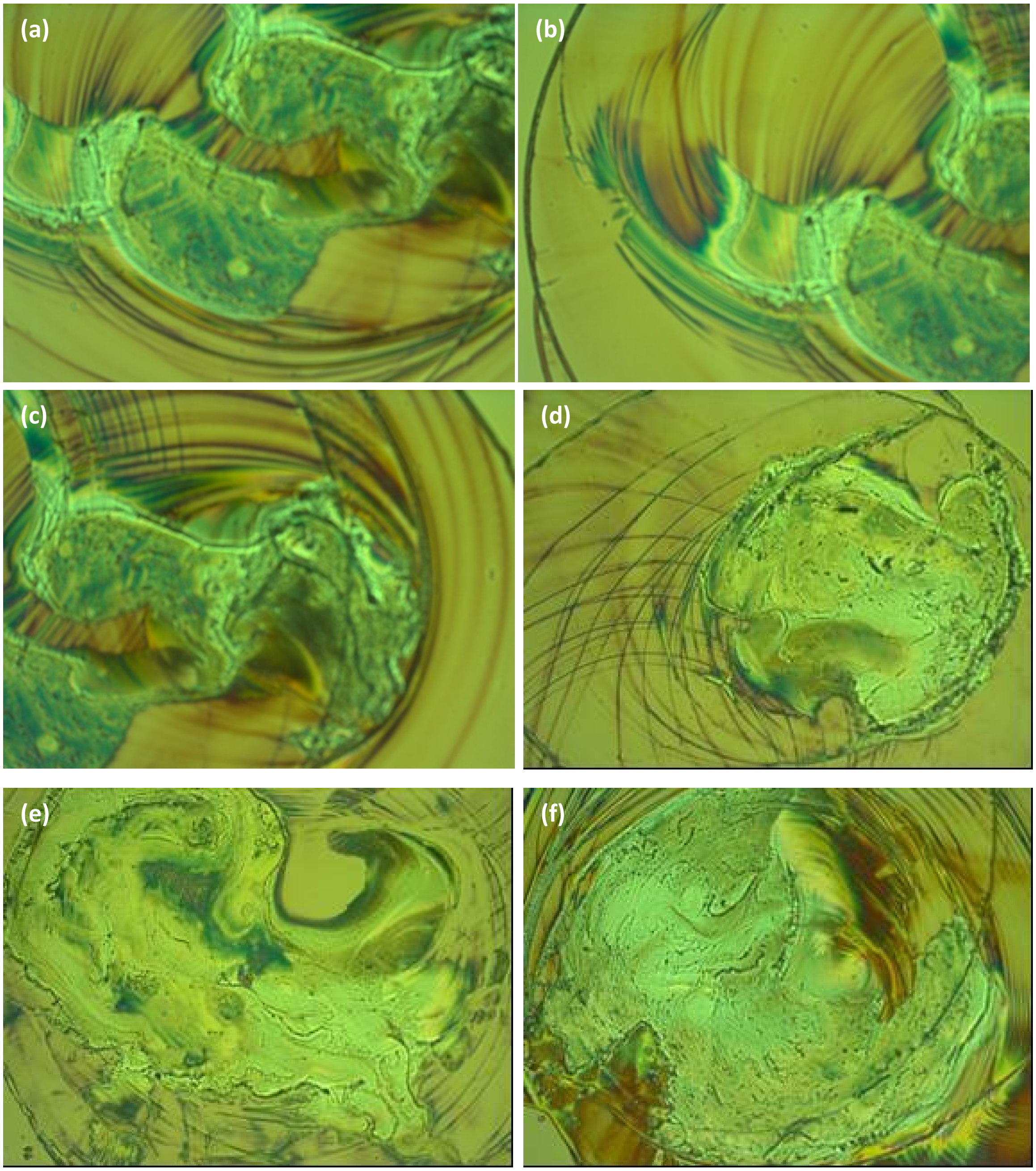

Figure D.5: Silver as deposited onto silica coated sensor (a-c). All other images taken after Post Flow measurements. Sensors were exposed to flows of baseline ultrapure water (d-j), pH adjusted water at 4.7 (k-n) and at 9.3 (o-r), water with turbidity of 51 NTU (s-v), water containing $NaNO_3$ (w-z) and $Ca(NO_3)_2$ (aa-dd) at an ionic strengths of 150 mM, water containing NaOCl at 525 mg/L (ee-hh) and at 8.8 mg/L (ii-ll).

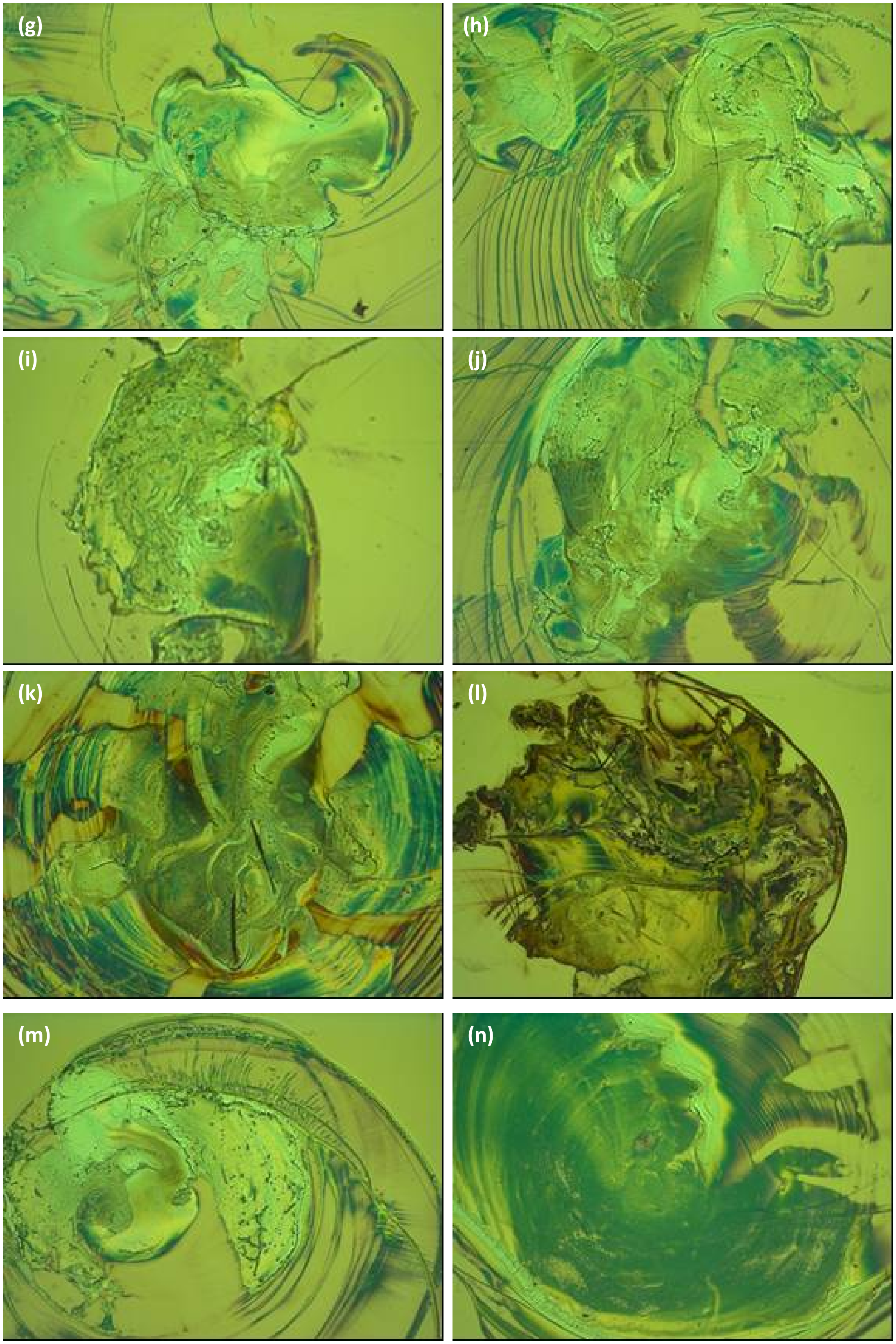
(g)
(h)
(i)
(j)
(k)
(l)
(m)
(n)

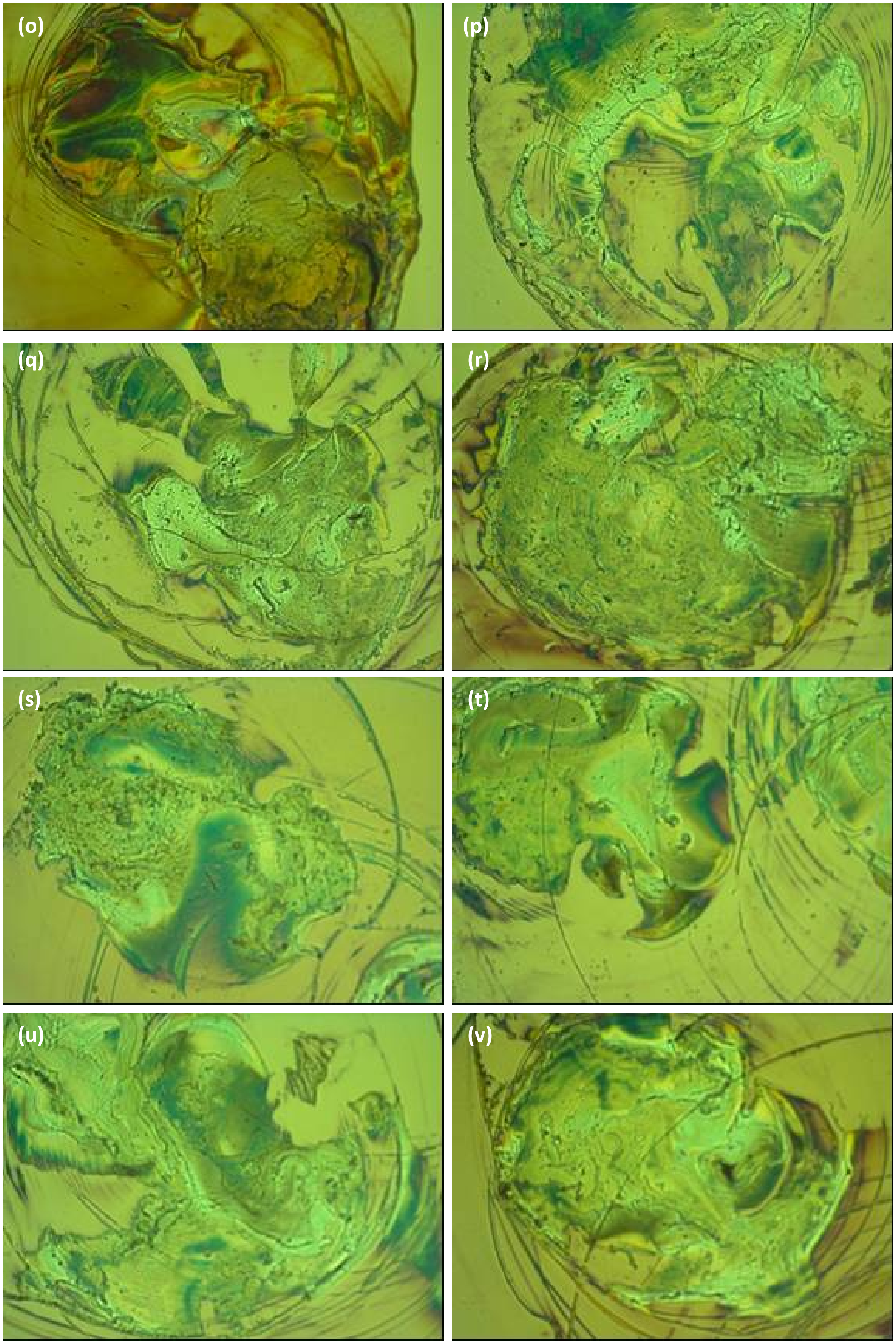
(o)
(p)
(q)
(r)
(s)
(t)
(u)
(v)

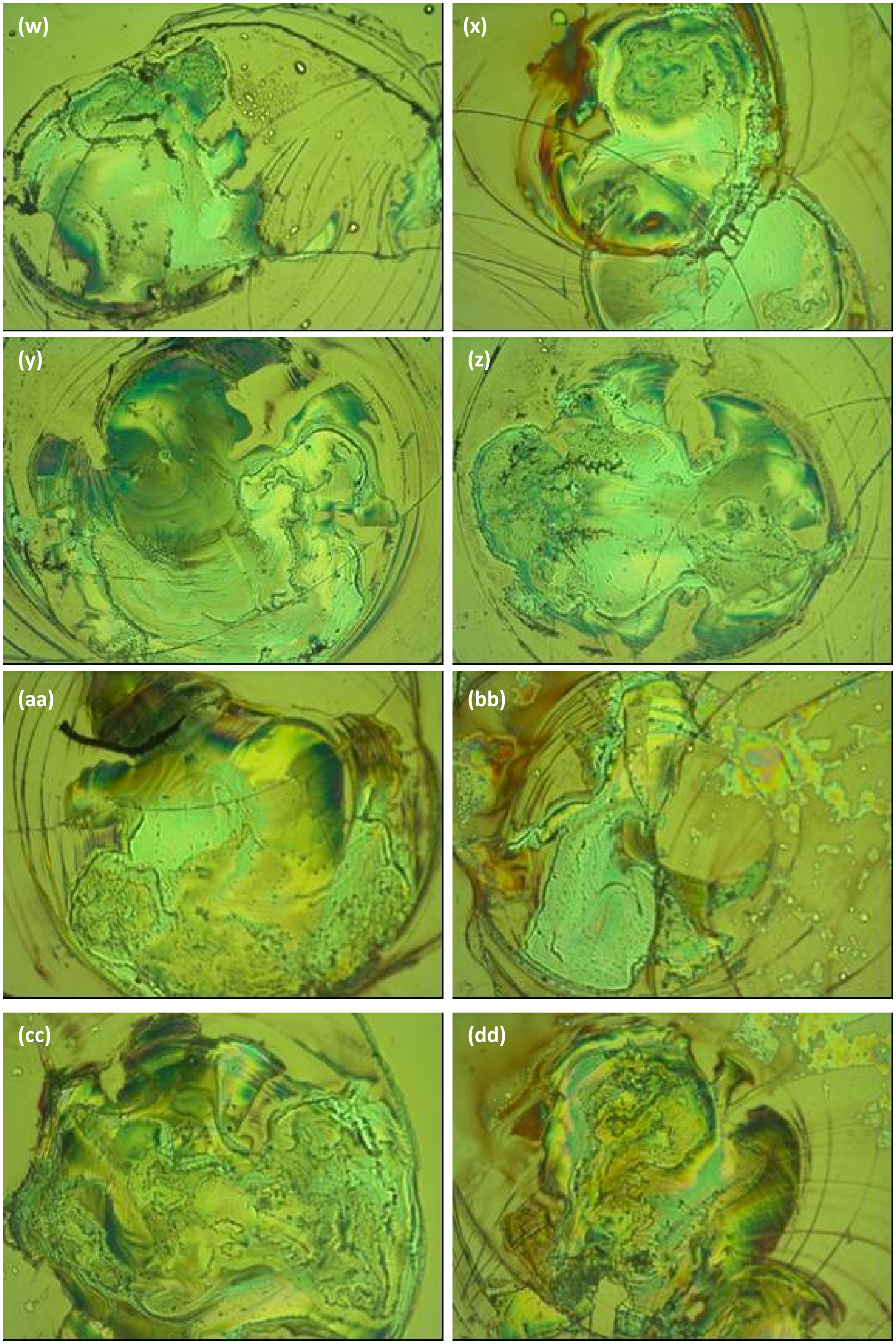
(w)
(x)
(y)
(z)
(aa)
(bb)
(cc)
(dd)

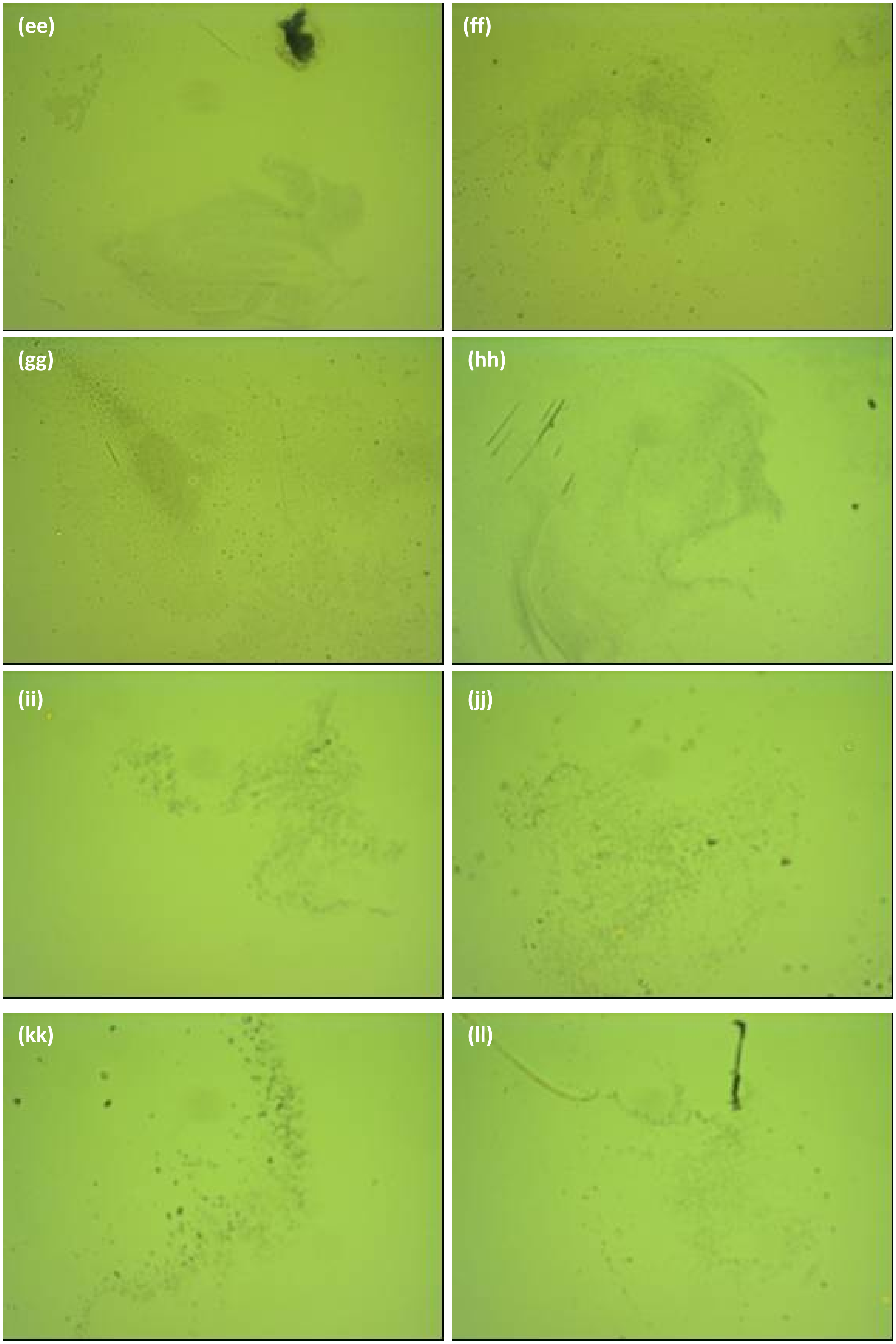
(ee)
(ff)
(gg)
(hh)
(ii)
(jj)
(kk)
(ll)

Appendix E: Analysis

Appendix E.1: Statistical Comparison Summary

	Statistical value	Baseline flow	Ag flow	Grouped, Baseline to Ag comparison
Millipore, group 1	**W(p) =**	0.015	0.055	0.03
	F-critical, 0,05	2.61	2.61	2.01
	p-value	0.003	0.017	0.000
Millipore, group 2	**W(p) =**	0.002	0.439	0.20
	F-critical, 0,05	2.61	2.61	2.01
	p-value	0.000	0.275	0.014
51 NTU	**W(p) =**	0.000	0.041	0.03
	F-critical, 0,05	2.61	2.61	2.01
	p-value	0.000	0.011	0.000
pH = 4.7	**W(p) =**	0.002	0.000	0.00
	F-critical, 0,05	2.61	2.61	2.10
	p-value	0.000	0.000	0.000
pH = 9.8	**W(p) =**	0.000	0.017	0.02
	F-critical, 0,05	2.61	2.61	2.01
	p-value	0.000	0.003	0.000
NaNO3	**W(p) =**	0.034	0.074	0.04
	F-critical, 0,05	2.61	2.61	2.01
	p-value	0.008	0.026	0.000
Ca(NO3)2	**W(p) =**	0.005	0.051	0.03
	F-critical, 0,05	2.61	2.61	2.01
	p-value	0.000	0.015	0.000
NOM at 15 mg/L TOC	**W(p) =**	0.034	0.084	0.25
	F-critical, 0,05	2.61	2.61	2.01
	p-value	0.008	0.031	0.028
8.8 mg/L NaOCl	**W(p) =**	0.213	0.005	0.12
	F-critical, 0,05	2.61	2.61	2.01
	p-value	0.113	0.000	0.003
525 mg/L NaOCl	**W(p) =**	0.002	0.003	0.00
	F-critical, 0,05	2.61	2.61	2.01
	p-value	0.000	0.000	0.000

Equation 7: Statistical analysis to determine parallel lines (Graybill 1976)

$$W_P = \frac{\sum_{h=1}^{N}\left[m_h - \frac{\sum_{i=1}^{N} m_i \cdot b_{ii}}{\sum_{j=1}^{N} b_{jj}} \right]^2 \cdot b_{hh}}{(N-1)\cdot\sigma^2}$$

where $b_{hh} = \sum_{t=1}^{n_h} (x_{ht} - \overline{x_h})^2$

m is the 3rd harmonic rate of change for each sensor

N is the total number of sensors being compared

n (lower case) is the total number of data points for each sensor

σ is the error of the linear regression

x represents each data point

x(bar) is the mean of the data set

Linear regression of "Linear Region" of flow runs

	Mean Baseline	Mean Silver	df	t-stat	t-ratio	p-value
Millipore, group 1	0.05	0.03	6	0.62	0.26	0.555
Millipore, group 2	0.06	0.07	6	0.68	0.28	0.520
Millipore, grouped	0.06	0.05	14	0.21	0.10	0.834
51 NTU	0.01	0.07	6	5.08	2.08	0.002
pH = 4.7	0.01	0.06	5	3.74	1.45	0.013
pH = 9.8	0.17	0.01	6	12.72	5.20	0.000
NaNO3	0.07	0.07	6	0.10	0.04	0.926
Ca(NO3)2	0.00	0.07	6	4.01	1.64	0.007
NOM at 15 mg/L TOC	0.01	0.11	6	2.70	1.11	0.035
8.8 mg/L NaOCl	0.02	0.05	6	2.07	0.85	0.083
525 mg/L NaOCl	0.02	0.10	6	2.08	0.85	0.083